Studies in Gas Phase Nonlinear Laser Spectroscopy and Laser Assisted Processes at the Gas-Surface Interface

Madeline Burke Fusco Memovich
Silverdale, Washington

B.S., Fort Lewis College, Durango, Colorado, 2016

A Dissertation presented to the Graduate Faculty
of the University of Viginia in Candidacy for the Degree of
Doctor of Philosophy

Department of Chemistry

University of Virginia
December, 2023

Madeline Memovich; mbm7wf@virginia.edu

Abstract

More than 60 years following the demonstration of the first laser it remains one of the most valuable tools for modern scientific investigation. In recent years, the development of new techniques and instrumentation have led to improvements in measuring absolute frequencies and phases of optical waves, increasingly short laser pulses or narrow continuous-wave line widths. These techniques and more have led to advances in the understanding of the energetics, kinetics, and dynamics of chemical processes and all while enhancing both sensitivity and selectivity. Here, a portion of my graduate work is described by three separate projects where laser spectroscopy techniques were employed. First, the development of a high-resolution absorption spectrometer for detection of gas phase mercury at 405 nm. The lowest energy ground-state transition for mercury is at 254 nm. Lower energy excitation is achieved via pre-excitation of the ground state, followed by promoted relaxation into a meta-stable state. Second, the development of a saturated absorption spectrometer for detection of nitrous oxide. By saturating the P(18) ro-vibrational absorption line, a hole-burning feature can be created in the spectral line-shape. Measuring the broadening of this feature allows for Doppler-free pressure broadening coefficients to be measured. Third, the resonant infrared photodesorption of methane from a platinum single-crystal surface via resonant C-H stretch excitation. By tuning an optical parametric oscillator to the antisymmetric stretch mode of methane the rate of desorption was measured via change in Fourier transform infrared spectral intensity. A corresponding effective IR photodesorption cross-section, relevant to protostar ice mantle astrochemistry, was determined.

Madeline Memovich; mbm7wf@virginia.edu

Acknowledgements

Let's keep this short and sweet. Thank you to the numerous people who helped me get to this point. Thank you to all my friends, family, and faculty members/educators for your encouragement, support, and inspiration. Thank you for continuing to believe in me even when I lost faith in myself. Thank you to everyone would helped me, in big or small ways, I couldn't have done it without you. We all stand on the shoulders of giants.

Contents

Abstract ii
Acknowledgements iii
List of Figures vi
List of Tables xi
Chapter 1 1
1.1. Absorption and Emission of Light 1
1.2. Basic Absorption Spectroscopy 3
1.3. Spectroscopy Basics at Surfaces 5
Chapter 2 9
2.1. Introduction 9
2.1.1. Motivation 9
2.1.2. Previous Work 11
2.1.3. Long Term Goal 13
2.1.4. Complications: Reactivity with Oxygen 13
2.2. Experimental 15
2.2.1. Properties of Atomic Mercury 15
2.2.2. System Energetics 16
2.2.3. Kinetic Model 18
2.2.4. Determination of Mercury Vapor Concentration 23
2.2.5. Theoretical Spectra at 405 nm 26
2.2.6. Experimental Design 29
2.2.7. Mercury Lamp Emission 33
2.3. Results and Discussion 35
2.3.1. Metastable Mercury Spectra 35
2.3.2. Ground State Absorption 44
2.4. Conclusion 47
Chapter 3 48
3.1. Introduction 48
3.1.1. Motivation 49

3.1.2. Linear and Nonlinear Absorption 51
3.1.3. Pressure Broadening 55
3.2. Experimental 57
3.2.1. Properties of Nitrous Oxide 57
3.2.2. Theoretical Linear Spectra 59
3.2.3. Experiment Design 62
3.2.4. Beam Profiling 64
3.2.5. Spectral Analysis 69
3.3. Results and Discussion 73
3.3.1. Doppler-Free Pressure Broadening Coefficients of P(18) Transition of N_2O 73
3.3.2. Impact of Frequency Modulation Depth and Saturation on Line-Shape 81
3.3.3. Doppler-Free Two-Photon Spectroscopy of Q(18) Transition of N_2O 83
3.4. Conclusion 85
Chapter 4 86
4.1. Introduction 86
4.1.1. Motivation 86
4.2. Experimental 88
4.2.1. Properties of Methane 88
4.2.2. System Energetics 89
4.2.3. Determination of Methane Adsorption and Desorption 92
4.2.4. Experimental Design 95
4.3. Results and Discussion 98
4.3.1. Monolayer Desorption 98
4.3.2. Multilayer Desorption 100
4.3.3. IR Photodesorption Cross-Sections 103
4.4. Conclusions 105
References 106

List of Figures

Figure 1.1. Simplified diagram of direct absorption spectroscopy. **(a)** Experimental diagram. **(b)** Absorption of photon in two-level energy system. **(c)** Resulting absorption profile..... 4

Figure 1.2. Geometry of light reflection and transmission from Medium 1 to Medium 2. 7

Figure 2.1. From A. Srivastava and J. T. Hodges (2018). Top panel: (a) measures (symbols) and fitted ground state ($6\ ^1S_0 \rightarrow 6\ ^3P_1$) absorption coefficient for mercury vapor at room temperature with no added gas (background gas pressure p < 10-6 Pa) based on weighted fit to ln(z), where z is the measured transmission and an absorption cell path length of 10 mm. The data and fit have been offset by 5 units for clarity. (b) Simulated spectra for pure mercury vapor at T = 296 K with indicated transitions, including hyperfine structure of the odd isotopes. Bottom panel: fit residuals. Gaps in residual plot represent points where absorption saturation is observed.[8] 12

Figure 2.2. Energy level diagram of elemental mercury showing relevant transitions and their corresponding wavelengths..... 17

Figure 2.3. Population of the metastable state as a function of system pressure for 273 and 300 K. it can be seen that the population rapidly rises at low pressures at around a few Torr and gradually decreases after it reaches the peak. 23

Figure 2.4. Relationship between temperature and mercury vapor pressure. (a) Values for vapor pressure taken directly from CRC handbook ranging from the freezing point up to room temperature. (b) Values from the CRC Handbook converted to result in a linear relationsip and its corresponding regression fitting line. 25

Figure 2.5. Theoretical spectra of $^3P_0 \rightarrow 7\ ^3S_1$ transition for natural mixture of mercury under conditions comparable to experimental environment. Solid lines represent an expected absorbance if all mercury vapor atoms are excited ($N_{Hg100\%}$). Dashed lines represent the expected absorbance if half of the mercury vapor atoms are excited ($N_{Hg50\%}$). Red lines are at a calculated cell total pressure of 30 Torr, blue lines are a total pressure of 60 Torr. Left panel: entire spectral range showing all isotope shifts and splitting. Right panel: Spectral range comparable to experimental range..... 29

Figure 2.6. Schematic diagram of internal mercury calibration system. Where MFC1 denotes the mercury vapor mass flow control valve and MFC2 is the dilution flow control. 32

Figure 2.7. Experimental apparatus. Diagram includes additions made to address experimental complications described in Section 2.1.4. PD: photodetector; A/D: analog to digital converter; λ/2: half-wave plate; PMT: photo multiplier tube..... 33

Figure 2.8. Broadband Emission of Philips TUV PL-L 95 W mercury lamp used for ground state excitation provided from the product data sheet. 34

Figure 2.9. Top panel: (a) measured (line) and fitted (dotted) excited state ($6\ ^3P_0 \rightarrow 7\ ^3S_1$) absorption spectra for mercury vapor at 273 K and a total pressure of 30 Torr calculated as described above. The fitting model used is a combination of four Voigt profiles to account for the splitting of the odd numbered isotopes. The data and the fit have been offset by 0.1 for clarity. **(b)** The individual Voigt components of the overall fit and their associated isotope. Bottom Panel: fit residuals. 36

Figure 2.10. New depiction of the same spectra and interpolation fit in Figure 2.9. The fitted component attributed to the absorption of the even numbered isotopes is shaded. The total area under this curve is used to calculate the population of mercury in the metastable population..... 38

Figure 2.11. Calculation of percent of mercury population in the metastable state at various cell pressures over increasing nitrogen flow rates. All values were collected with the reservoir at a temperature of 273 K and calculated as described above. 39

Figure 2.12. Comparison of two spectra both taken at a cell pressure of 30 Torr and reservoir temperature of 273 K taken two weeks apart. 40

Figure 2.13. Photo taken by Professor Kevin K. Lehmann depicting coking residue build-up inside the absorption cell located at the inlet likely as a result of excited mercury reacting with trace oxygen. 42

Figure 2.14. Multiple spectra overlaid to illustrate the variation of the amplitude of an un accounted absorption peak around 0.15 cm^{-1} away from the 202-isotope absorption peak. The relative intensities of each spectrum have been corrected for to ensure they are all of the same scale for ease of comparison. 43

Figure 2.15. Analysis of the measured ground state absorbance in the secondary absorption cell with increasing cell pressure. Mercury flow rate was controlled via the PSA Mercury Calibration System and all values taken with a dilution flow of 1000 ml min^{-1} and mercury temperature of 40° C. Solid lines represent a second order linear regression fit. 45

Figure 3.1. Calculated One-photon (in red) and Two-photon (in blue) absorption spectrum for C_3H_8 gas at 300 K. Each transition is plotted as a stick with a height equal to its fraction of the total intensity. The OPA spectrum is multiplied by -10^3 for clarity. 50

Figure 3.2. Comparison of direct absorption spectroscopy and saturated absorption spectroscopy. **(a)** Basic experimental design. Direct absorption spectroscopy utilizes one singular directional laser to measure absorbance. In contrast, saturated absorption spectroscopy utilizes counter propagating beams. In both, the gas analyte exhibits a Maxwell Boltzmann velocity distribution which contributes to Doppler broadening of absorbance line**.** Note, the pump beam is displayed at an angle to the probe beam for clarity**. (b)** Two level energy diagram. In saturated absorption

spectroscopy the counterpropagating pump beam induces a reduction of population in upper energy level. **(c)** Resulting absorption feature. saturated absorption spectroscopy produces spectral hole-burning effect (Lamb-dip), Doppler-free Lorentzian centered at ν_0. 53

Figure 3.3. How one color two-photon spectroscopy from counterpropagating waves is Doppler-free. **(a)** The Laboratory frame. The absorbing medium is traveling at a velocity of V which can be described as a vector pointing in the direction of movement. This vector can be broken up into its components to give the velocity in the direction of the propagating waves (V_z). The waves are both traveling towards the absorber with angular frequency ω but in opposite directions. **(b)** In the atomic frame the frequencies are up/down shifted depending on direction of molecule velocity. These two frequency shifts cancel resulting in Doppler-free line-shape.[28] 54

Figure 3.4. Chemical Structure of N_2O with bond information provided by NIST. 57

Figure 3.5. Energy level diagram of relevant N2O transitions referencing P(18) (ν12), R(17) (ν23), two-photon Q(18) (νTP), and detuning (Δν12) frequencies. Energy levels are for illustrative purposes and not drawn to scale for clarity. 59

Figure 3.6. Theoretical unsaturated spectra of 5 mTorr of N_2O with various amounts of additional gas (air) included indicating the effect of pressure broadening. While in the linear regime, increase in air pressure does not result in a change in absorbance and all lines poses an equivalent absorbance value of 1.62. 62

Figure 3.7. Simplified experimental apparatus depicting quantum cascade laser (QCL) beam path in red. The first order deflected beam from the acousto-optic modulator (AOM) is used in the absorption cell to allow for power modulation. Lenses ($L_{1\text{-}4}$) are used to control the beam size in the cell and laser locking cavity. A beam-splitter following the absorption cell reflects to a curved focusing mirror (radius of curvature $R = 50\ mm$) which sends the transmitted beam back through the cell towards the QCL until it is blocked by the isolator. The radius of curvature was chosen maintain the beam size in the reverse propagation to the forward propagation to maximize beam overlap. 64

Figure 3.8. IR cross-sections of beam fitted to Gaussian Profile. **(a)** The raw thermal image of the beam taken with Spiracon Pyrocam. **(b)** The thermal image is then converted to a matrix where each pixel is assigned a value denoting how bright it is. Can be shown as both a contour plot or a mesh plot to show the 3-D Gaussian shape. **(c)** The matrix is then fitted using least-squares methods to a Gaussian function to determine the spot size at this particular position. From a collection of these fits the overall beam propagation can be determined. 66

Figure 3.9. Beam propagation of QC laser output without any focusing. This was used to help determine proper lens/telescope options to focus beam to desired size in absorption cell. The beam waist ω_0 was determined as 0.942 mm and z_0 = 616.119 mm. 67

Figure 3.10. Beam propagation fit in absorption cell after adjusting telescope to focus into the center of the cell. New waist was determined as 0.444 mm and z_0 = 135.969 mm. 68

Figure 3.11. Representation of the fit to the saturated absorption line shape and breaking it down into Gaussian and Lorentzian components. 70

Figure 3.12. Generated line shape depicting the frequency modulated absorption of a Gaussian derivative with an added Lorentzian derivative at the central frequency ν_0. If the back reflection is blocked the Lorentzian component will not be visible. 71

Figure 3.13. Spectrum of 5 mTorr of N_2O. (a) Absorbance spectrum and least-squares interpolation fit. (b) The Gaussian and Lorentzian components which combine to the interpolation fit. (c) Residuals between absorbance spectrum and fit. 74

Figure 3.14. Saturated absorption spectra taken at increasing pressures of N_2O starting from 5 mTorr to 15 mTorr. As the pressure was increased the Lamb-dip became smaller and more difficult to measure. 75

Figure 3.15. Comparison of the Lamb-dip size as N_2O pressure increased in reference to spectra shown in Figure 3.14. **(a)** The depth (height) of the Lamb-dip as pressure increased. **(b)** The FWHM of the Lamb-dip as pressure increased. 76

Figure 3.16. Saturated absorption spectra of 5 mTorr of N_2O with increasing amount of added argon gas. Increase in overall absorbance of Doppler broadened peak indicates a reduction in saturation as pressure is increased. 77

Figure 3.17. Side-by-side comparison of the **(a)** 5 mTorr N_2O absorbance spectrum to **(b)** 5 mTorr N_2O with 35 mTorr argon spectrum showing the overall absorbance increasing by more than a factor of 2 as well as the depth of the Lamb-dip, indicating the loss of saturation. 79

Figure 3.18. A comparison of Lamb-dip amplitude as the Doppler-broadened absorbance increases. Values used are based on fitted values from spectra in Figure 3.16 which were taken under the same conditions. As the Doppler-Broadened absorbance increases while N_2O population remains the same, the saturation parameter must be decreasing. 80

Figure 3.19. The change in amplitude of the demodulated peak while the modulation depth was increased. The amplitude shown is a relative value. Spectra shown, the modulation frequency was 50 kHz sine wave and the lock-in amplifier used to demodulate the spectra had atime constant of 10 msec and 1 mTorr of N_2O. 82

Figure 3.20. Broadband spectrum of N_2O at 1.19 Torr with no added gas scanning over a region encompassing the R(17), P(18) and the Q(18) is expected to be seen. The experimental spectrum is compared to a theoretical spectrum generated from HITRAN database which does not contain two-photon data. Evidence of vibrational heating can be seen around 2207.39 cm^{-1}. The Y-axis is restricted to 1 for clarity of the smaller transitions. 84

Figure 4.1. Chemical Structure of CH_4. 88

Figure 4.2. Diagram representation depicting various vibrational energy dissipation pathways for physiosorbed on Pt(111). 91

Figure 4.3. RAIRS spectrum depicting detection and characterization of physiosorbed methane $CH_{4(p)}$ on Pt(111). The symmetric and antisymmetric modes and their respective absorption FWHM's are highlighted. The spectrum was collected at a surface temperature $Ts = 35\ K$ and saturation of the monolayer, equivalent to 0.33 platinum monolayers. 93

Figure 4.4. RAIRS absorption spectra and associated methane coverage. As coverage increases beyond saturation of the monolayer, the multilayer peak forms. 95

Figure 4.5. Experimental apparatus. Diagram includes ultra-high vacuum (UHV) chamber with… 97

Figure 4.6. RAIRS spectra of methane coverage pre and post irradiation with OPO of the symmetric and antisymmetric vibrational modes. Little to no desorption of the monolayers was observed. 99

Figure 4.7. RAIRS spectra representative of methane coverage following OPO irradiation both on and off resonance with the ν_3 antisymmetric stretch. Methane desorption was measured at several different irradiation powers **(a)** 500 mW, **(b)** 1.00 W, **(c)** 1.25 W, **(d)** 1.5 W. For all spectra shown the surface was cooled to 40 K. 102

Figure 4.8. Loss of methane coverage as a function of vibrational excitation photon flux in reference to RAIRS spectra shown in **(a)** Figure 4.7 at 1.00 W excitation power and **(b)** Figure 4.7 at 1.25 W excitation power. 104

List of Tables

Table 2.1. Naturally occurring isotopes of mercury their associated mass and abundances..... 15

Table 2.2. Essential values required for modeling the kinetics of the two electronic excitations used in this research. 19

Table 2.3. Frequency shifts and associated normalized peak intensity for all isotopes of naturally occurring mercury and hyper-fine splitting of odd numbered isotopes.[22, 23] 27

Table 3.1. Natural isotopes of nitrous oxide, their associated mass, and natural fractional abundances. 58

Table 3.2. Transition constants relevant for generating a theoretical spectrum for the P and R branch transitions from HITRAN database. The two-photon, Q(18) transition information is not available in the database. 60

Table 4.1. Description of Methane Vibrational Modes: gas-phase and surface bound frequencies included.[43-46] 89

Table 4.2. Calculated upper-bound effective IR photodesorption cross-sections determined from desorption rates depicted in Figure 4.8. 104

Chapter 1

Introduction

1.1. Absorption and Emission of Light

Throughout the work presented in this thesis the field of spectroscopy is employed fundamentally as a diagnostic tool. Spectroscopy is the study of the interaction between matter and light, and therefore a basic explanation of fundamental interactions between mater and light should be provided for context. Light is electromagnetic radiation which is composed of an electric field wave and magnetic wave perpendicular to one another and propagates with the vector *k*. The magnetic field travels along the same axis with same the frequency as the electric field and as a result, light waves are commonly described in terms of only their electric component.

The wave can be described in terms of its wavelength (commonly units of nm, μm, Å) or oscillation frequency (s^{-1}, MHz, GHz, cm^{-1}) where they are related by $\nu = c/\lambda$, where ν is the frequency, λ is the wavelength, and c is the speed of the wave. The speed of the wave depends on the medium in which it travels as well as its frequency where $c = c_0$ in a vacuum but otherwise can be described as $c = c_0/n(\nu)$ where n is the frequency dependent index of refraction of the medium where frequency is absolute, regardless of medium, but wavelength varies. The energy of a light wave is given by $E = h\nu = h\frac{c}{\lambda}$ where h is Planck's constant which arises due to the quantized nature of light energy.

The range of energies available in electromagnetic radiation have been described as a spectrum split into several regions. Each region of the electromagnetic spectrum can be associated

with different chemical processes depending on the available energy. At the low end of the spectrum, radio and microwave radiation only poses enough energy to induce nuclear or electronic spin flips or rotational transitions. The infrared region (IR) is associated with vibrational transitions, and the visible and ultraviolet regions are capable of exciting valence electrons in atoms and molecules. At the high-energy end of the spectrum are X-rays and gamma (γ) rays which are capable of exciting core electrons and nuclear processes.

Now that basic light plane waves have been described, the absorption and emission of light by matter can be discussed. Considering a two-level energy system with ground state $|i\rangle$ with energy E_i and excited state $|k\rangle$ and energy E_k and each state is populated with a population number density of $N_{i,k}$. A change in the population between the two states can be caused by any of three processes: absorption, spontaneous emission, or stimulated emission. If a wave with energy $E = h\nu = E_k - E_i$ is incident upon the system, the energy may be absorbed causing a body in the ground state $|i\rangle$ to transition to the excited state $|k\rangle$. This process can be described in terms of coefficient $B_{i\rightarrow k}$ referred to as the Einstein absorption coefficient which describes the rate constant of absorption for the transition.

Similarly, a body already in the excited state can relax back down to the ground state either spontaneously or induced by radiation (stimulated). If the body relaxes as a result of stimulation from a photon of energy *E*, then following relaxation, the two exiting photons will be identical in all properties (energy, phase, direction, etc.). The rate of this process is described by $B_{k\rightarrow I}$ the stimulated emission coefficient. Finally, the body in the excited state can spontaneously relax to the ground state releasing a photon at a rate described by

$$\frac{dN_k}{dt} = -A_{k\rightarrow i}N_k$$

Where $A_{k\rightarrow i}$ is the transition lifetime. The rate of transition from the ground state to excited state via absorption is given by

$$\frac{dN_k}{dt} = B_{i\rightarrow k}\rho_\nu N_i$$

and rate contribution from stimulated emission is given by

$$\frac{dN_k}{dt} = -B_{k\rightarrow i}\rho_\nu N_i.$$

Given a thermal system should be in equilibrium with the surrounding radiation field, Einstein showed that

$$B_{i\rightarrow k} = B_{k\rightarrow i}$$

and

$$A_{k\rightarrow i} = \frac{8\pi h\nu^3}{c^3}B.$$

Interestingly the rate constants for seemingly very different processes, spontaneous emission and absorption, are found to be equal.[1]

1.2. Basic Absorption Spectroscopy

Consider a system consisting of an absorbing gas contained in a vapor cell of volume V and length l. This gas has the same two-level energy system described in the previous section. If a flux of photons with energy $E = h\nu$ is incident upon the system such that the incident intensity can be described as $I_0 = Fh\nu$ where F is the flux. The change in flux as a result of passing through the absorbing medium of discrete thickness dx can be described as

$$dF = -\sigma F(N_i - N_k)dx$$

Where integrating over the entire length of the absorption cell results in

$$\ln\left(\frac{F}{dF}\right) = \ln\left(\frac{I}{I_0}\right) = -\sigma\Delta N l$$

or

$$I = I_0 e^{-\sigma\Delta N l}$$

Known as Beer's law where I is the intensity exiting the vapor cell and σ is the cross-section which describes the effective area the absorber represents in relation to the flux.[1] Most simply to measure the degree of absorbance experimentally the drop in intensity of light source before and after absorption can be measured. Absorption is then calculated by

$$A = -\ln\frac{I}{I_0}.$$

See Figure 1.1 for a diagram of direct absorption spectroscopy.

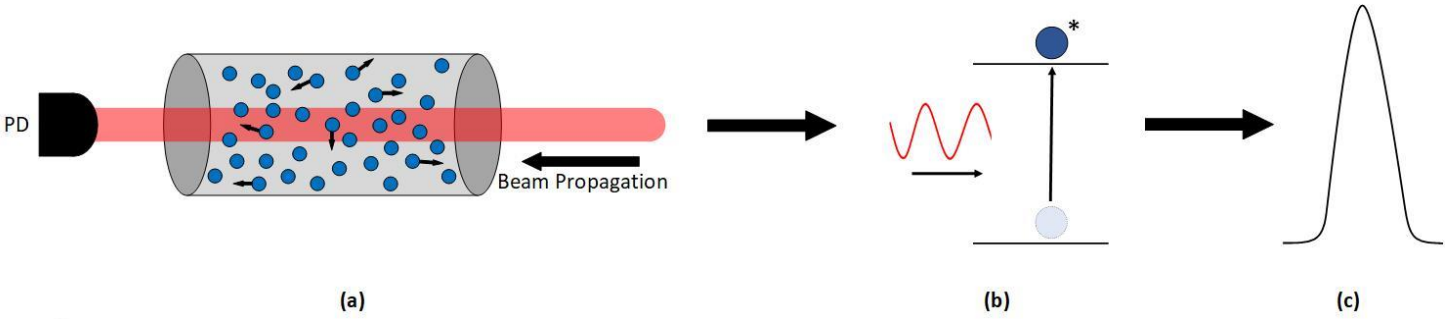

Figure 1.1. Simplified diagram of direct absorption spectroscopy. **(a)** Experimental diagram. **(b)** Absorption of photon in two-level energy system. **(c)** Resulting absorption profile.

As seen in Figure 1.1 (b), despite the system having discrete energy levels the resulting absorption profile (Figure 1.1 (c)) is not seen as a delta function, but rather exhibits broadening and can be expressed in various profiles. These profiles are described as lineshape functions ($g(v)$)

and can be separated into two categories, homogeneous and inhomogeneous broadening. The total lineshape of the system can be described as the collection of lineshapes for each absorbing atom or molecule. Whether the overall broadening is described as homogeneous or inhomogeneous is dependent on whether each individual absorbing species generates an identical lineshape or not. In the former case, it would be considered homogeneous broadening. On the contrary, if the individual species exhibit different lineshapes then it's considered inhomogeneous broadening. The various lines are a result of a variety of molecular environments which contribute to relatively minor shifts in absorption frequency for each absorber in the sample. The convolution of all these individual absorption lines then results in the overall lineshape. Some of the environmental variations which can induce broadening are as follows, high pressure/collisional, relative velocity of the absorber to the light wave (Doppler), transition lifetime of the excited state, transit-time, and more.[1]

1.3. Spectroscopy Basics at Surfaces

To apply spectroscopic techniques to probe kinetics and dynamics at crystal surfaces it must be understood how light interacts with the surface. As an electromagnetic wave impinges upon a surface the light can interact via reflection, transmission, absorption, scattering or a combination. According to Snell's Law, the angle of incidence for a light wave reflecting off a surface is equivalent to the angle of reflection[2] or

$$\theta_i = \theta_r.$$

The intensity of the reflected and transmitted waves is dependent on the polarization of the light with respect to the surface normal. See Figure 1.2 for a depiction of light reflection and

transmission through a surface. The intensity of the reflected and transmitted waves is given by Fresnel formulae where the reflection coefficients of s-polarized light can be described as

$$r_s = \frac{n_i \cos(\theta_i) - n_t \cos(\theta_t)}{n_i \cos(\theta_i) + n_t \cos(\theta_t)}$$

And transmission coefficient of s-polarized light as

$$t_s = \frac{2n_i \cos(\theta_i)}{n_i \cos(\theta_i) + n_t \cos(\theta_t)}.$$

For p-polarized light the transmission and reflection coefficients are given by

$$r_p = \frac{n_i \cos(\theta_t) - n_t \cos(\theta_i)}{n_i \cos(\theta_t) + n_t \cos(\theta_i)}$$

$$t_p = \frac{2n_i \cos(\theta_i)}{n_i \cos(\theta_t) + n_t \cos(\theta_i)}$$

where

$$n_i \sin(\theta_i) = n_t \sin(\theta_t)$$

And the reflectance $R = r^2$ and transmittance $T = \left(\frac{n_t \cos(\theta_t)}{n_i \cos(\theta_i)}\right) t^2$.

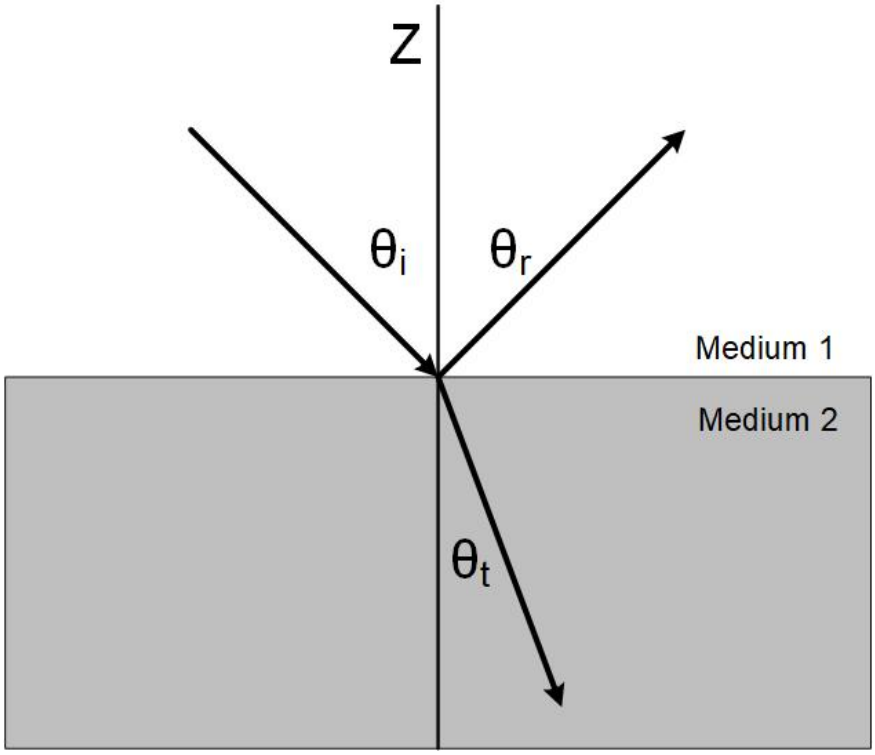

Figure 1.2. Geometry of light reflection and transmission from Medium 1 to Medium 2.

In addition to considering how light interacts directly with the surface, the interaction between the exciting light, the surface and the molecular transitions must be considered. A technique referred to as reflection absorption infrared spectroscopy (RAIRS) is a powerful tool for analyzing vibrational modes on a surface. The IR absorbance on a surface can be measured by glancing an infrared beam across the surface and detecting the reflected beam. When measuring these modes on the surface the polarization of the beam must be considered. For a vibrational transition from state $|i\rangle$ to state $|k\rangle$ the transition dipole moment is given as $\vec{\mu}_{ik}$ and $\vec{E}$ is the electric field vector. While there is absorption of the wave by the molecule induces a dipole moment, in turn a mirror image of the dipole is induced in the metal surface also. The component of the dipole which is perfectly parallel to the surface is counteracted by its reflection and conversely

perpendicular components are enhanced by a factor of two. In addition, the polarization of the electric field has the same effect where the reflection cancels out parallel components and enhances perpendicular ones.[2]

Chapter 2

Pre-excitation Spectrometer for Trace Mercury Detection Through Probing the Meta-Stable 6 $^3P_0 \rightarrow 7\ ^3S_1$ Transition

Contributing Authors: Robert Fisher, Kevin K. Lehmann

2.1. Introduction

The Experiment described in this chapter details the development of a spectrometer designed for detection of elemental mercury vapor in the atmosphere. Here a novel approach was employed using two successive electronic excitations, hereafter referred to as pre-excitation. A primary benefit to this approach being lowering the probe excitation frequency which allows for greater sensitivity, selectivity and improved cost projections. Other factors were considered in the design to address practical concerns such as measurement time, calibration requirements, and anticipated overall size which will be discussed in greater detail in the following sections.

2.1.1. Motivation

Mercury is an atmospheric pollutant with toxic effect on environmental and human health.[3-8] Atmospheric mercury exists in three forms: particle-bound mercury (Hg-p), divalent gaseous mercury (Hg(II)), and gaseous elemental mercury (Hg0 or GEM).[6, 8, 9] The most abundant form of mercury in the atmosphere is GEM, accounting for approximately 95% of all atmospheric mercury.[6] In this form, the pollutant has a residence time estimated at 6 to 18 months.[4, 6, 8] Due to this long lifetime, GEM is prone to travel long distances, deposition, re-emission and bioaccumulation contributing to its extensive biogeochemical cycle.[4] Furthermore, mercury is

classified as a neurotoxin.[3, 5] It's regulated by the United States Environmental Protection Agency and various other government agencies as a hazardous pollutant.[6, 8, 10] Toxic effects of mercury and its compounds include ataxia, constriction of vision, impaired hearing and death in extreme cases. Mercury is most commonly released into the air through burning of coal in power plants. When this happens, mercury and various other gases such as carbon dioxide (CO_2), carbon monoxide (CO), nitrogen dioxide (NO_2) and sulfur dioxide (SO_2) are also being released in a mixture referred to as flue gas.[4, 6, 11]

Nitrogen dioxide (NO_2), sulfur dioxide (SO_2), and ozone (O_3) are atmospheric gases known to absorb light at similar wavelengths to mercury which can interfere with accurate detection of mercury using the $6\ ^1S_0 \rightarrow 6\ ^3P_0$ transition. Despite these difficulties, several previous studies on mercury detection have been reported using the $6\ ^1S_0 \rightarrow 6\ ^3P_0$ transition at 254 nm. In addition to interference from competing gases, using this transition can be more expensive and less sensitive. In general, there are fewer options for tunable lasers and high-reflective mirrors in the ultra-violet (UV) region as compared to the visible and infra-red (IR) regions of the electromagnetic spectrum (EM), and are typically more expensive and of lower quality. This makes trace gas detection at 254 nm less ideal compared to a longer wavelength. For these reasons, it is important to develop new, reasonable methods for the detection and quantification of atmospheric mercury which can be used in the presence of flue gas. For these reasons a pre-excitation spectrometer was designed and tested where the mercury would undergo two successive excitations from multiple light sources. The probe excitation occurs at 405 nm, in the visible region, where lasers and higher reflectivity mirrors are more available and there's less absorption from other atmospheric gasses.

2.1.2. Previous Work

Currently, the quantification of mercury emissions in the field is commonly carried out through the use of systems with a calibration GEM generator unit and cold-vapor atomic absorption or fluorescence spectroscopy (CVAAS or CVAFS) analyzers according to EPA method 30A.[10] These GEM generators hold a reservoir of liquid mercury under controlled temperature and metered by a carrier gas and use the partial pressure of the mercury to produce accurate mercury mass concentration. These generators require routine certifications due to system drift, which ultimately makes their use time-consuming, labor intensive and costly. Using cold vapor atomic fluorescence spectroscopy, a five-minute response time is required for a detection limit of 0.1 ng m^{-3}.[12]

Cavity ring-down spectroscopy was first employed for the detection of mercury by Jongma et al. in 1995. Due to the relatively broad line-width of their pulsed laser source (7.5 GHz), they were only able to achieve a detection limit of approximately 17.5 ng m^{-3}.[13] Later, Fain et al.[14] also developed a Doppler-resolved cavity ring-down spectroscopy technique for mercury detection. Their pulsed laser had an improved line width of 0.9 GHz and allowed for a detection limit of 0.10 ng m^{-3} at a time resolution of 10 seconds.[14] Pierce et al. expanded on this work by testing in field like environments and found a similar detection limit of 0.35 ng m^{-3} in stable GEM conditions over a time resolution of five minutes.[12] Recently a new mercury detection method was developed using high-resolution laser absorption spectroscopy method. It was estimated to a detection limit of approximately 0.1 μg m^{-3}.[8] Although this method is estimated to be 100 times less sensitive than the CVAFS method mentioned above, it has the advantages of a significantly faster response time and does not require calibration. However, all

of these techniques mentioned use a probe wavelength of 254 nm to measure the 6 $^1S_0 \rightarrow 6\ ^3P_1$ transition of mercury. Because of this, these methods are all susceptible to interference from competing gases if employed for field use, and thus lose accuracy. Below in Figure 2.1 shows a mercury spectrum taken by A. Srivastava and J. T. Hodges using this high-resolution technique. Although susceptible to interfering absorbance from other gases in the atmosphere, this technique could likely be used for calibration of CVAFS devices due to its ability to determine absolute mercury concentration and fast response time.

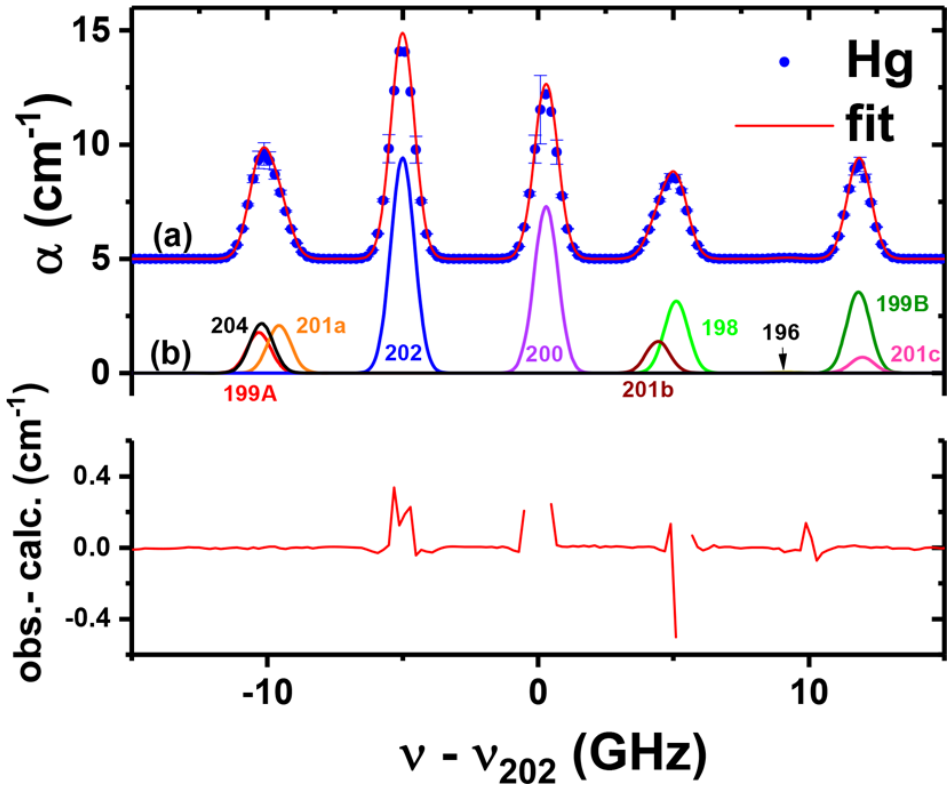

Figure 2.1. From A. Srivastava and J. T. Hodges (2018). Top panel: (a) measures (symbols) and fitted ground state (6 $^1S_0 \rightarrow 6\ ^3P_1$) absorption coefficient for mercury vapor at room temperature with no added gas (background gas pressure p < 10-6 Pa) based on weighted fit to ln(z), where z is the measured transmission and an absorption cell path length of 10 mm. The data and fit have been offset by 5 units for clarity. (b) Simulated spectra for pure mercury vapor at T = 296 K with indicated transitions, including hyperfine structure of the odd isotopes. Bottom panel: fit residuals. Gaps in residual plot represent points where absorption saturation is observed.[8]

2.1.3. Long Term Goal

In the details explained in the experimental design (section 2.2.6) a single pass vapor cell was employed for mercury detection. In order achieve the desired low detection limits (on the order of parts per trillion gas concentration by volume), cavity ring-down techniques were planned on eventually being implemented. However, due to various complications which arose over the course of the project (see section 2.14 for more detail) this endeavor was canceled. It is still possible that these complications could be addressed in future works and potential solutions are later provided. Also, as these complications are specific to mercury detection, the technique described below could likely be employed for trace gas detection of other atomic species or homo-nuclear diatomic molecules such as molecular hydrogen (H_2) and molecular nitrogen (N_2) with either no or limited low-energy ground state transitions available.

2.1.4. Complications: Reactivity with Oxygen

Over the course of the project, it was observed that the visibility of the mercury spectra would vacillate depending on the gas system conditions. This major complication led to the necessary addition of several components to the experimental design than were originally intended.

While collecting mercury spectra over the course of several months, the absorption intensity was observed to vary drastically under seemingly consistent conditions and eventually spectra became increasingly difficult to collect. Through literature review it was determined that the likely cause of the loss of the signal was caused by excited mercury reacting with trace amounts of oxygen present in the system. Research presented by Callear et al.[15] suggested the following reaction pathway

$$Hg\ 6\ ^3P_1 + O_2 \rightarrow O_2^* + Hg\ 6\ ^1S_0$$

$$O_2 + O_2^* \rightarrow O_3 + O$$

$$O_2 + O_2^* \rightarrow O_2 + O_2$$

$$O + O_2^* + M \rightarrow O_3 + M$$

$$O_3 + Hg \rightarrow HgO + O_2$$

$$O + O_3 \rightarrow O_2 + O_2.$$

Oxygen gas is known to be an effective quencher and this was anticipated prior to starting the project. However, by the mechanism proposed above oxygen would be reacting with excited mercury to produce mercuric oxide (HgO). Not only would this prevent sufficient population build up for the probe transition, but also inconsistencies in the overall sample concentration, leading to inaccuracy in the quantitative measurement. As a result of this finding, it became incredibly important to reduce oxygen contamination in the system and find ways to confirm the population in the metastable state and overall mercury concentration.

2.2. Experimental

The following section details the procedures used in this project both theoretical and experimental. Information regarding properties and relevant transitions of mercury are also discussed to provide a foundation for discussion of results in following sections.

2.2.1. Properties of Atomic Mercury

In the current section some basic properties of mercury will be discussed which will provide a basis for the framework of the research project. Mercury is a unique element, notably as the only transition metal classified as a liquid at standard temperature and pressure and it also has an appreciable vapor pressure of 0.184 Pa at room temperature (294 K). It even has a T_{fus} = 234.3 K = -38.85 °C allowing the vapor to be measured down to relatively low temperatures.[16] Mercury is rather heavy with an atomic mass of 200.592(3) Da, but for calculations used in this research the average weight used was 200 AMU.

Isotope	Atomic Mass (Da)	Isotopic Abundance (fractional)
^{196}Hg	195.96583(2)	0.0015(1)
^{198}Hg	197.966769(3)	0.1004(3)
^{199}Hg	198.968281(4)	0.1694(12)
^{200}Hg	199.968327(4)	0.2314(9)
^{201}Hg	200.970303(5)	0.1317(9)
^{202}Hg	201.970644(5)	0.2974(13)
^{204}Hg	203.973494(3)	0.0682(4)

Table 2.1. Naturally occurring isotopes of mercury their associated mass and abundances.

Mercury's reduced electronic configuration is given by [Xe] $4f^{14}$ $5d^{10}$ $6s^2$. Therefore, the ground state of mercury has two 6s electrons in its valence shell, and thus the individual orbital angular momenta of each electron combine to produce a total orbital angular momentum and similarly for the spin angular components. Electrons in s orbitals have an orbital angular momentum of $l_s = 0$ and the spin angular momentum of an individual electron can only have a value of $s = 1/2$. L, the total angular momentum can have values of $l_1 + l_2 \ldots l_1 - l_2$, for two s orbital electrons where $l_1 = l_2 = 0$, $L = 0$. Similarly, the total spin angular momentum $S = s_1 + s_2 \ldots s_1 - s_2$ and for $s_1 = s_2 = 1/2$, $S = 0, 1$ but, $S = 1$ is forbidden in this instance by the Pauli Exclusion Principle. L and S combine to give $J = L + S$, the total angular momentum, and the multiplicity is given by $2S + L$. Electronic states are characterized by $n\,{}^{2S+1}L_J$ where L is depicted as S, P, D, F for $L = 0, 1, 2, 3$ and thus the ground state of mercury is designated as 6 $^1S_0$.

2.2.2. System Energetics

As discussed in Chapter 1, individual atoms do not possess vibrational or rotational transitions, and most only have absorption transitions from the ground-state in the ultraviolet region of the electromagnetic spectrum. In the case for atomic mercury, the lowest energy, ground-state transition is at 254 nm, within the UV region. In this region, there are limited laser sources and are typically more costly compared to those in the visible and infrared regions. Furthermore, the 6 $^1S_0 \rightarrow 6\ ^3P_1$ transition at 254 nm is formally considered a forbidden transition because it requires a spin-flip ($\Delta S \neq 0$) leading it to be less intense compared to other transitions and therefore detection with this transition will be less sensitive. Despite these factors, mercury detection is most commonly measured using the 6 $^1S_0 \rightarrow 6\ ^3P_1$ transition. The excitation scheme used for this

research project is shown in Figure 2.2, which shows the relevant energy levels of elemental mercury, significant transitions and their corresponding wavelengths.

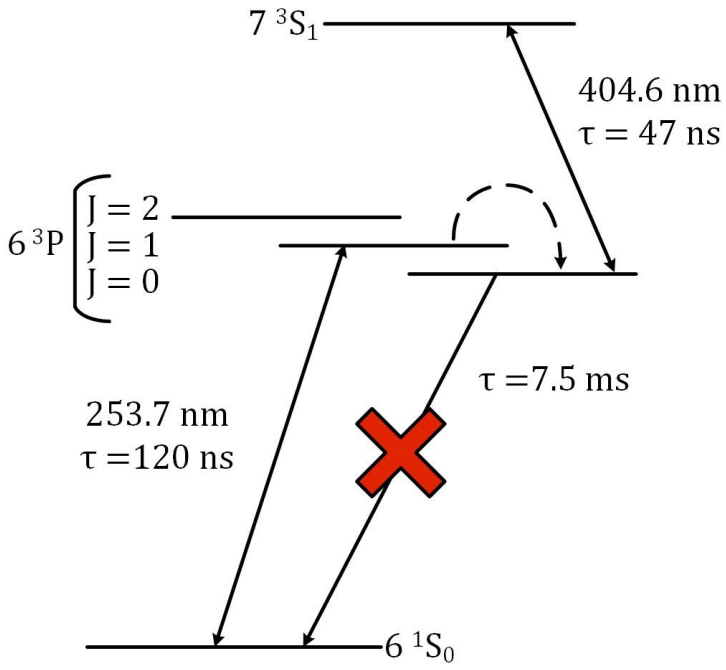

Figure 2.2. Energy level diagram of elemental mercury showing relevant transitions and their corresponding wavelengths.

In order to overcome these issues, we were developing a spectrometer utilizing two excitation steps. This will allow mercury detection to be measured using the more selective and sensitive 6 $^3P_0 \rightarrow 7\ ^3S_0$ transition at 405 nm. First, the mercury atoms will be excited through the 6 $^1S_0 \rightarrow 6\ ^3P_1$ transition at a wavelength of 254 nm mentioned earlier. When at sufficiently low pressures, these excited mercury atoms would then decay back down to the ground state with a lifetime of 125 ns (A_{12} = 8.41E6 s^{-1}).[8] However, in the presence of a bath gas, such as nitrogen, at sufficiently high pressures, these same atoms are more likely to collide with neighboring nitrogen molecules before relaxing back down to the ground state. When these collisions occur, the mercury

atoms can transfer some of their energy to the colliding molecule, causing the mercury atoms to most likely transfer to the 6 $^3P_0$ state, the lowest energy, electronically excited state (the dominant collisional energy transfer process)[17, 18]. The mercury atoms cannot decay by radiation while in the 6 $^3P_0$ state, due to the forbidden nature of the 6 $^3P_0 \rightarrow 6\ ^1S_0$ transition (selection rules dictate that angular momentum cannot be conserved, i.e., J=0 → J=0 is forbidden) and thus is long lived. Therefore, at appropriate pressures it should result in a sufficient build up in the population of the 6 $^3P_0$ state over time to promote to the 7 $^3S_1$ state using 405 nm light and measure the corresponding mercury number density in the metastable state. This should be proportional to the total mercury concentration provided that collisions between mercury atoms remains negligible and should remain accurate at mercury concentrations relevant for trace vapor monitoring in the atmosphere.

2.2.3. Kinetic Model

A kinetic model of the system was simulated to estimate expected values for the populations of the various electronic states depending on pressure and temperature of the system. In the later discussion sections, the results collected from experimental analysis will be compared to these expected values.

First, some essential values must be determined for each transition, starting with the $^1S_0 \rightarrow {}^3P_1$ transition. The spontaneous emission rate has previously been determined as $A = 8.04 \times 10^6\ s^{-1}$ the inverse of this gives the transition lifetime $\tau \approx 120$ ns. The Doppler full width at half maximum (FWHM) of the $^1S_0 \rightarrow {}^3P_1$ transition at λ=254 nm can be calculated according to

$$\Delta\nu_D = \frac{2c}{\lambda}\sqrt{\frac{2k_bT * ln(2)}{M_{Hg}c^2}} = 1040\ MHz$$

where c is the speed of light, k_b is the Boltzmann constant, T is temperature and M_{Hg} is the mass of mercury.[1, 19] The normalized lineshape factor on resonance for the Doppler broadened line is given by,[1]

$$g_D = \frac{2}{\Delta\nu_D} * \sqrt{\frac{\ln(2)}{\pi}} = 9.06x10^{-10}\ s.$$

The peak absorption cross section for the transition is calculated, neglecting hyperfine structure in spectra as a result of the isotopes. There is an additional factor of three to account for degeneracy.

$$\sigma_{254} = \frac{3 * \lambda^2 * g_D}{8 * \pi} * A = 5.6x10^{-13}\ cm^2$$

Similarly, these values were determined for the $^3P_0 \rightarrow {}^3S_1$ transition at $\lambda = 405$ nm. For the ease of the reader and to reduce repetition, all values have been included in Table 2.2 below.

Quantity	$6\ {}^1S_0 \rightarrow 6\ {}^3P_1$	$6\ {}^3P_0 \rightarrow 7\ {}^3S_1$
Transition Wavelength – λ (nm)	254	405
Spontaneous Emission rate – A (s^{-1})	$8.41x10^6$	$2.07x10^7$
Transition Lifetime – τ (ns)	118.9	47.6
Doppler FWHM – $\Delta\nu_D$ (MHz)	1040	651
Doppler Normalization Factor – g_D (s)	$9.06x10^{-10}$	$1.44x10^{-9}$
Absorption cross section – σ (cm^2)	$5.6x10^{-13}$	$5.9x10^{-12}$

Table 2.2. Essential values required for modeling the kinetics of the two electronic excitations used in this research.

To determine the metastable state population, let p_1, p_2 and p_3 be the relative populations in the $^1S_0$, $^3P_1$ and $^3P_0$ levels respectively.

$$\frac{dp_1}{dt} = -k_p p_1 + (A + k_{21}P)p_2 + k_{31}p_3 P$$

$$\frac{dp_2}{dt} = k_p p_1 - (A + k_{21}P + k_{23}P)p_2 + k_{32}p_3 P$$

$$\frac{dp_3}{dt} = k_{23}p_2 P - (k_{32} + k_{31})p_3 P$$

where P is pressure in Torr and k_p is the rate of excitation by the pre-excitation lamps and all other k values are associated with the various population states. Assuming steady-state conditions, then all population rates are equal to 0 giving

$$p_3 = \frac{k_{23}}{k_{32} + k_{31}} p_2$$

$$p_1 = \frac{1}{k_p}(A + k_{21}P + \frac{k_{31}k_{23}}{k_{32} + k_{31}} P)p_2$$

and because population is conserved, meaning $p_1+p_2+p_3=1$, then

$$p_2 = \left[[1 + \frac{k_{23}}{k_{32} + k_{31}} + \frac{1}{k_p}(A + k_{21}P + \frac{k_{31}k_{23}}{k_{32} + k_{31}} P)]^{-1} \right].$$

Finally, p_3 can then be expressed as a function of pressure and k_p, given by

$$p_3(P) = \frac{k_{23}k_p(P)}{N_{hg}(k_{21}k_{31} + k_{21}k_{32} + k_{31}k_{23}) + A(k_{31} + k_{32}) + k_p(P)(k_{31} + k_{23} + k_{32})}.$$

In order to determine the population of the $^3P_0$ state, k_p must be determined as a function of pressure. This is achieved by determining the overlap between the pre-excitation lamp emission

spectrum with the mercury absorption spectrum treated as Voigt line profiles at room temperature Doppler broadening and Lorentzian pressure broadening. This results in a pressure dependent function for k_p given by,

$$k_p(P) = \frac{5.818E3}{1 + 1.25\frac{P}{760} - 0.32\left(\frac{P}{760}\right)^2 - 0.15\left(\frac{P}{760}\right)^3}.$$

Using the collisional relaxation cross sections of mercury by nitrogen gas published by Pitre et al. (σ_{23} = 7.2x10^{-17} cm^2, $\sigma_{31} \leq$ 2.0x10^{-22} cm^2, $\sigma_{21} \leq$ 4.1x10^{-19} cm^2)[20] the various rate constants can be determined by

$$k_{23} = v_c N_{Torr} * 7.2\text{x}10^{-17} = 1.132x10^5\ s^{-1}$$

$$k_{32} = Qk_{23} = 131.3\ s^{-1}$$

$$k_{21} = v_c N_{Torr} * 4.1\text{x}10^{-19} = 628.9\ s^{-1}$$

$$k_{31} = v_c N_{Torr} * 2.0\text{x}10^{-22} = 0.314\ s^{-1}$$

where Q is the equilibrium constant for $^3P_1$ and $^3P_0$ states given by $Q = 3e^{\frac{-\Delta E}{k_b T}} = 1.16\ x\ 10^{-3}$ at 300 K, v_c is the mean collision speed for mercury and nitrogen gas, $v_c = \sqrt{\frac{8k_bT}{\pi}\left(\frac{1}{M_{N_2}} + \frac{1}{M_{Hg}}\right)} = 5.29x10^4\ \frac{cm}{s}$, and N_{Torr} is the number density of nitrogen at 1 torr, $N_{Torr} = \frac{1\ torr}{k_b T} = 2.97x10^{16}\ cm^{-3}$.[20] Finally, the rates need to include relaxation by mercury with mercury collisions by including the mercury-mercury $^3P_0$ quenching rate of 3.4x10^{13} cm^3 mol^{-1} s^{-1} given by Callear and Williams.[17] The new rate equations are as follows:

$$k_{23}(P) = (v_c N_{Torr} * 7.2\text{x}10^{-17})P$$

$$k_{32}(P) = Qk_{23}(P)$$

$$k_{21}(P,T) = (v_c N_{Torr} * 4.1\text{x}10^{-19})P + \frac{3.4x10^{13}}{N_A} N_{Hg} T$$

$$k_{31}(P,T) = (v_c N_{Torr} * 2.0\text{x}10^{-22})P + \frac{3.4x10^{13}}{N_A} N_{Hg} T$$

$$p_3 = \frac{k_{23}k_p(P)}{(k_{21}(P,T)k_{31}(P,T)+k_{21}(P,T)k_{32}(P)+k_{31}(P,T)k_{23}(P))+A(k_{31}(P,T)+k_{32}(p))+k_p(P)(k_{31}(P,T)+k_{23}(P)+k_{32}(P))}.$$

From these calculations we can visualize the pressure and temperature dependence of the metastable population, depicted in Figure 2.3.

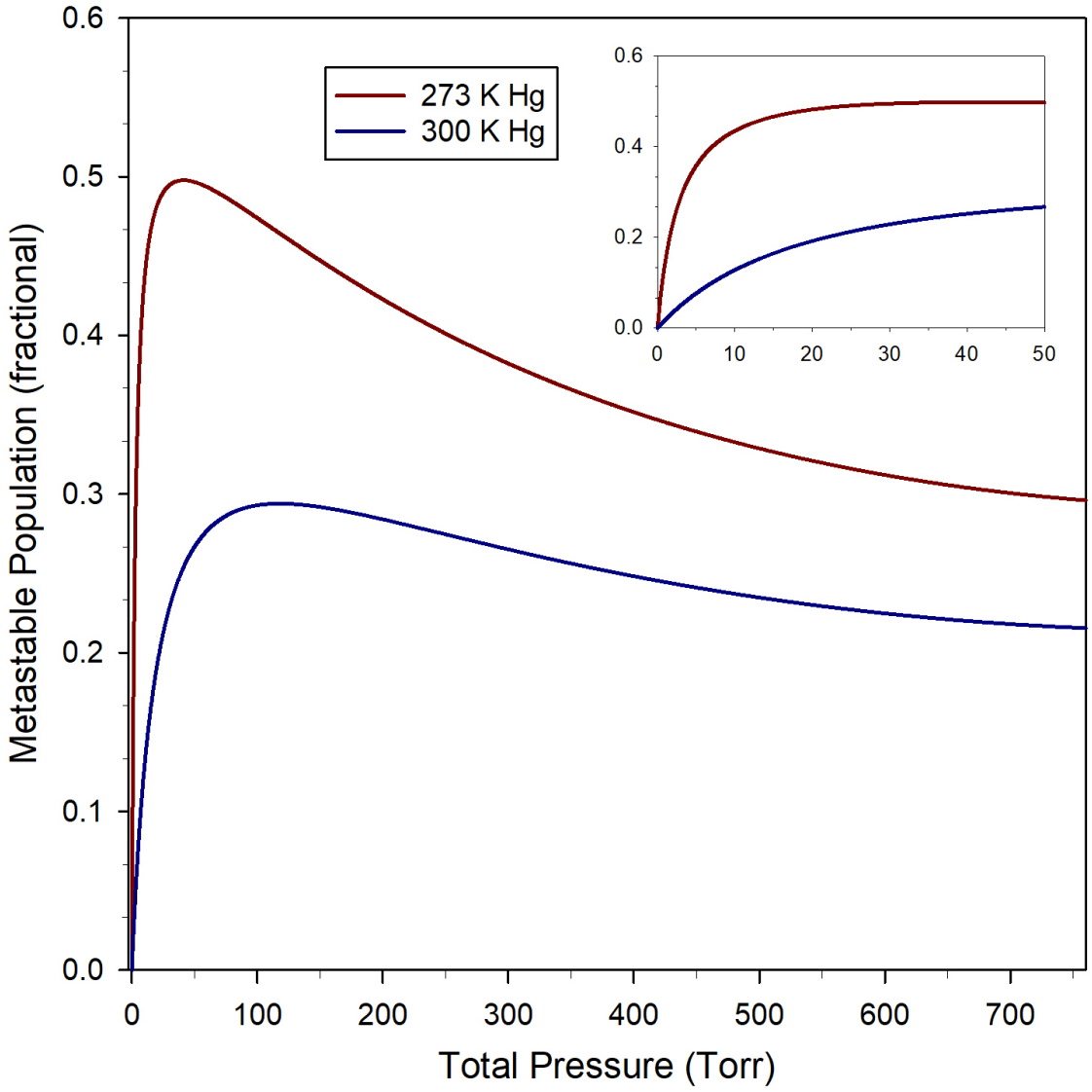

Figure 2.3. Population of the metastable state as a function of system pressure for 273 and 300 K. it can be seen that the population rapidly rises at low pressures at around a few Torr and gradually decreases after it reaches the peak.

2.2.4. Determination of Mercury Vapor Concentration

As mentioned above, in order for the assumption of the system being under steady-state conditions to be reasonable, the concentration of mercury in the spectrometer is controlled based on the vapor pressure released from a small sample of liquid mercury. Therefore, a method to

determine the vapor pressure was required. Shown in Figure 2.4 (a), using values collected from the CRC Handbook of Chemistry and Physics a relationship could be extrapolated for use under the temperature range used in this experiment.[21] By applying the data to a least-squares fit which related temperature and vapor pressure, the pressure could be determined at any temperature. By applying a natural logarithm to the vapor pressure of mercury and relating it to the inverse of the temperature, a linear relationship could be achieved and fitted. See Figure 2.4 (b) for the fitted relationship. To solve for the vapor pressure of mercury, apply an exponential function

$$P_{Hg} = \exp\left[-\frac{7412.5}{T} + 23.5\right]$$

Where P_{Hg} is the vapor pressure of mercury in Pascals and T is temperature in Kelvin. To convert pressure to number density, divide by K_bT

$$N_{Hg} = \frac{P_{Hg}}{K_bT} * \left(1x10^{-6}\frac{m^3}{cm^3}\right)$$

Where N_{Hg} is in atoms/cm^3.

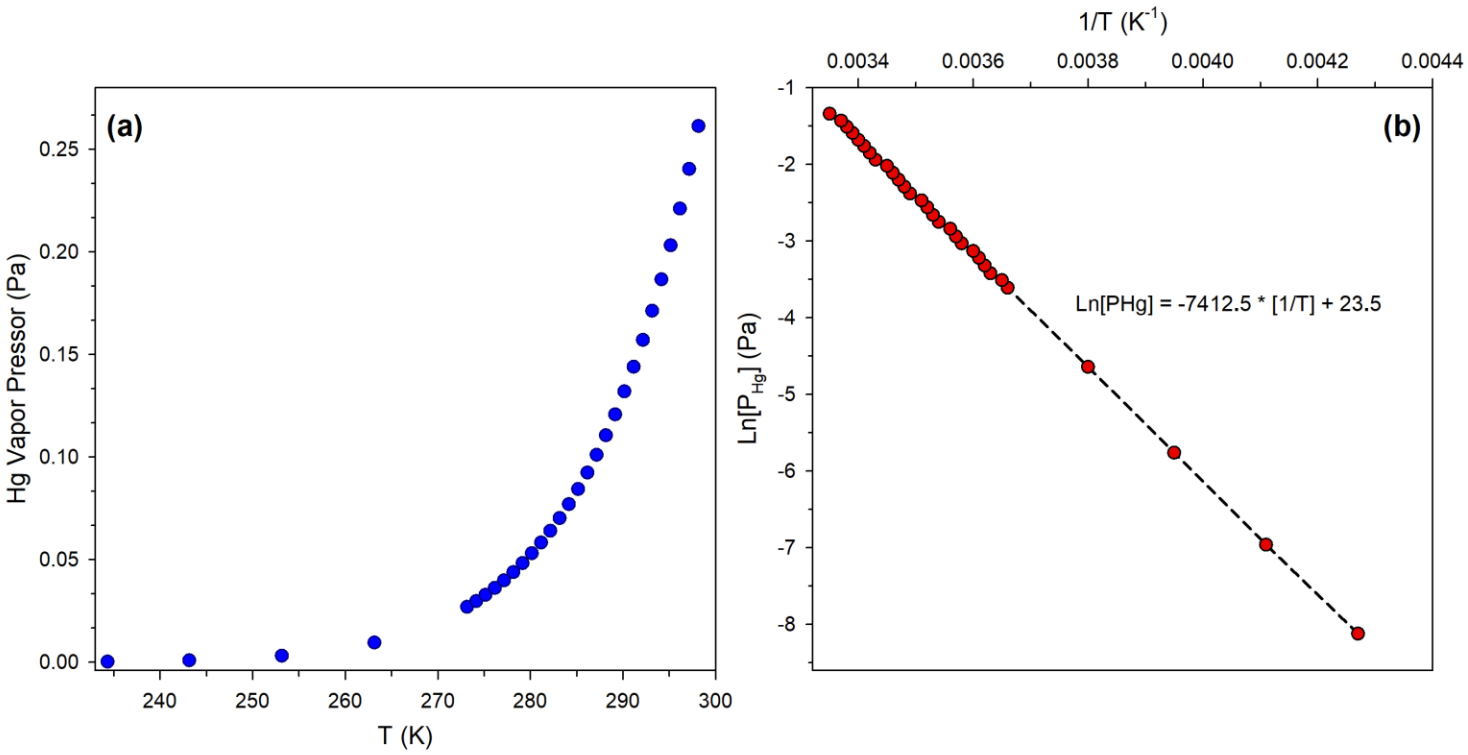

Figure 2.4. Relationship between temperature and mercury vapor pressure. (a) Values for vapor pressure taken directly from CRC handbook ranging from the freezing point up to room temperature. (b) Values from the CRC Handbook converted to result in a linear relationship and its corresponding regression fitting line.

The previous method was used in the lab to quickly estimate the mercury vapor concentration, but for precise measurements, simulated spectra, and kinetic modelling a method to calculate the vapor pressure developed by Amadei et al. was used.[22] Here it was determined that the expression

$$P_{Hg}(T) = P_0 \left(\frac{T}{T_0}\right)^{\Delta C_p/R} exp\left[-\frac{\Delta H_{vap} - \Delta C_p T_0}{R}\left(\frac{1}{T} - \frac{1}{T_0}\right)\right]$$

could describe the vapor pressure of mercury at temperature T and pressure P_0 where R is the gas constant, $\Delta H_{vap} = 61.6$ kJ/mol, and $\Delta C_p = -0.0661$ kJ/mol both at $T_0 = 273$ K. This was found

to have a high degree of accuracy over the entire temperature range of liquid mercury, with little over 5% error compared to experimental measurements at the extreme high and low ends of the temperature range.

2.2.5. Theoretical Spectra at 405 nm

Currently, minimal work by others has been done involving this transition and most work involving mercury has involved the ground state transition at $\lambda = 254\,nm$. Therefore, to have something to compare to, we have constructed a theoretical spectrum based on a model which matches the conditions of our experiment. Because we are working at pressures where pressure broadening becomes comparable to the Doppler width, each isotope peak will be represented as a Voigt profile. For the model I am using a comprehensive curve-fitting module in available in Python[23] which has a built-in Voigt profile with the form

$$f(x, A, \mu, \sigma, \gamma) = \frac{Re[w(z)]}{\sigma 2\pi}$$

where

$$z = \frac{x - \mu + i\gamma}{\sigma\sqrt{2}}$$

$$w(z) = e^{-z^2} erfc(-iz)$$

And $erfc(\,)$ is the complementary error function and $Re[\,]$ denotes the real portion of the value. Here, A represents the amplitude, and in this form the peak area, μ is the central frequency, σ is the standard deviation of the Gaussian component, and γ is the half width at half maximum (HWHM) of the Lorentzian component. In this context, the Gaussian σ is related to the Doppler full width at half max (FWHM, $\Delta\tilde{\nu}_D$) by

$$\sigma = \frac{\Delta\tilde{\nu}_D}{2\sqrt{2\ln 2}} \approx \frac{\Delta\tilde{\nu}_D}{2.35482}$$

and

$$\Delta\tilde{\nu}_D = \tilde{\nu}\ 7.2x10^{-7}\sqrt{\frac{T}{M}}$$

Where $\Delta\tilde{\nu}_D$ is in cm^{-1}, T is temperature in Kelvin, and M is the mass in AMU. For the Lorentzian component, γ is related to the pressure broadening. The pressure broadening coefficient has previously been determined by Z. Ben-Lakhdar-Akrout $\Delta\tilde{\nu}_{pb} = 0.745\ cm^{-1}Atm^{-1} = 9.8x10^{-4}\ cm^{-1}Torr^{-1}$.[24] and γ is related to $\Delta\tilde{\nu}_{ps}$ by

$$\gamma = \frac{\Delta\tilde{\nu}_{pb}}{2}.$$

Next, μ are based on the isotope shifts and hyper-fine splitting corresponding to the odd-numbered isotopes, and the normalized absorption intensity give A (Table 2.3).

Isotope	Frequency shift ($\nu - \nu_{202}$) (cm^{-1})	Normalized Peak Intensity
^{196}Hg	-0.075	0.0015
^{198}Hg	-0.0547	0.101
^{199}Hg (a)	-0.751	0.05666667
^{199}Hg (b)	0.321	0.11333333
^{200}Hg	-0.0287	0.23
^{201}Hg (a)	-0.401	0.0664
^{201}Hg (b)	0.236	0.04426667
^{201}Hg (c)	0.657	0.022
^{202}Hg	0	0.2965
^{204}Hg	0.0276	0.0685

Table 2.3. Frequency shifts and associated normalized peak intensity for all isotopes of naturally occurring mercury and hyper-fine splitting of odd numbered isotopes.[24, 25]

By summing over each peak in Table 2.3 and applying an associated Voigt profile based on the temperature and pressure conditions a simulated normalized line-shape ($g(\nu)$) can be calculated. To calculate the absorbance

$$A(\nu) = g(\nu) * S * L * N_{Hg}$$

Where S is the integrated line-strength, L is the absorption path length, N_{Hg} is the number density of mercury atoms in the cell in the metastable state. To calculate the integrated line-strength S

$$S = 3A * \frac{\nu_0^2}{8\pi c}$$

Where A is the spontaneous emission rate of the transition (Table 2.3), ν_0, is the central transition frequency, and c is the speed of light.

To calculate N_{Hg} in the cell there is an additional step than explained in Section 2.2.4. Due to a difference in pressure and temperature between the cell and the mercury reservoir, the number density in the cell can be calculated as a ratio of the number density as a result of the vapor pressure in the reservoir by

$$N_{cell} = N_{reservoir} * \frac{P_{cell}}{P_{reservoir}} * \frac{T_{reservoir}}{T_{cell}}.$$

The spectra simulated below (Figure 2.5) are calculated with the assumed conditions in the reservoir being equivalent to an atmosphere of pressure and at ice temperature (273 K). The cell is heated from room temperature due to the radiation of the mercury lamps to approximately 322 K and the pressure in the cell is varied as shown.

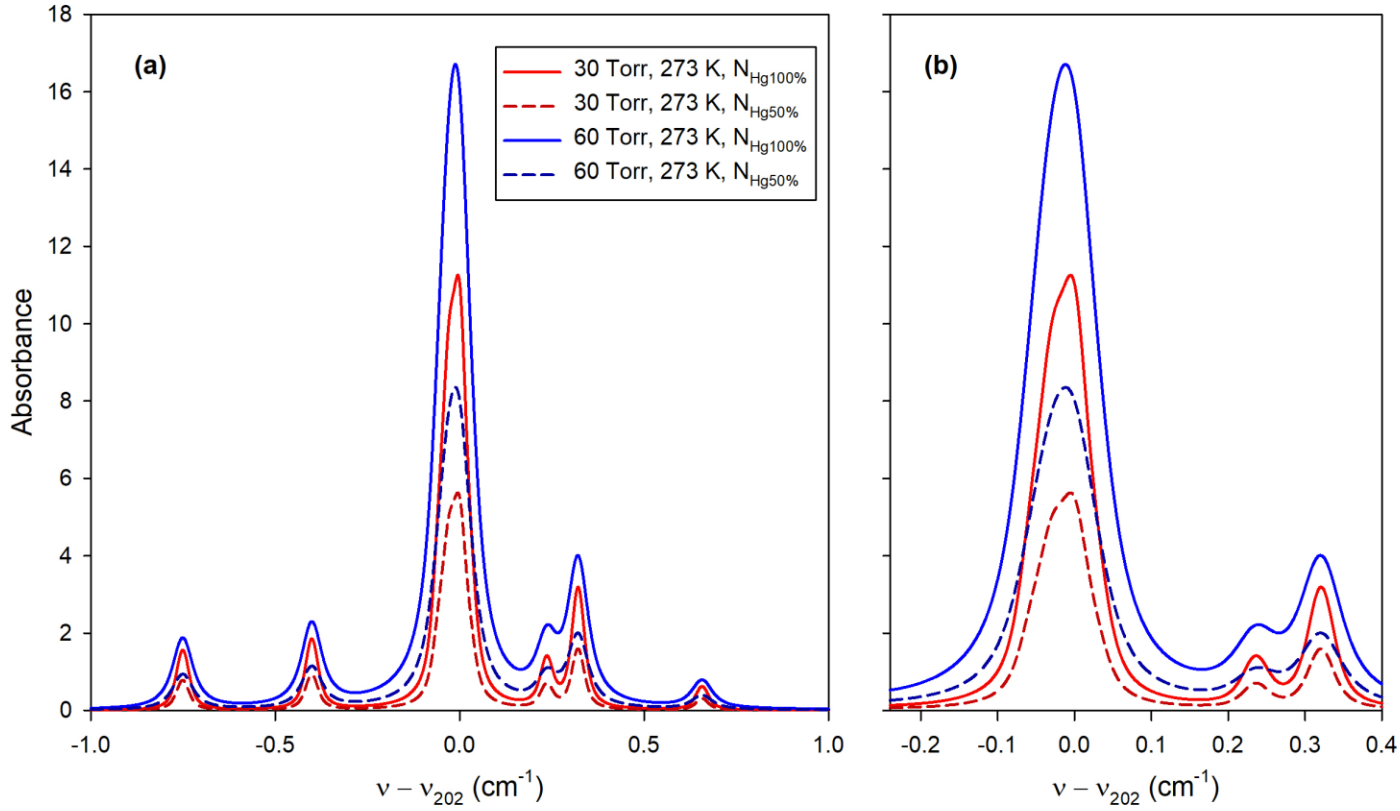

Figure 2.5. Theoretical spectra of $^3P_0 \rightarrow 7\ ^3S_1$ transition for natural mixture of mercury under conditions comparable to experimental environment. Solid lines represent an expected absorbance if all mercury vapor atoms are excited ($N_{Hg100\%}$). Dashed lines represent the expected absorbance if half of the mercury vapor atoms are excited ($N_{Hg50\%}$). Red lines are at a calculated cell total pressure of 30 Torr, blue lines are a total pressure of 60 Torr. Left panel: entire spectral range showing all isotope shifts and splitting. Right panel: Spectral range comparable to experimental range.

2.2.6. Experimental Design

The experiment described in this chapter utilizes a stainless-steel reservoir containing a few milliliters of liquid mercury where is can be assumed the vapor is in steady-state conditions. High purity nitrogen gas continuously flowed at a controlled rate through the top of the mercury reservoir before entering an optically transparent (quartz) vapor cell (L = 52 cm) until finally being pumped out of the system by a turbo pump station. The pressure in the cell and reservoir were

monitored using multiple MKS baratrons ranging up to a maximum of 1000 Torr. For each spectra taken, the pressure inside the cell was held constant while the flow rate of nitrogen gas was varied. To compensate for the change in flow rate, which was controlled via a Granville-Phillips Series 203 Variable Leak Valve, the pumping rate was simultaneously controlled to maintain the desired constant pressure by adjusting Swagelok vacuum control valves leading to the pump station. The variable leak valve had a backing pressure of approximately one Atm to maintain consistent flow rates and all flow values are represented as relative values. As mentioned in the previous section, pressure between the reservoir and the cell were monitored separately and could be accounted for. For consistency, the reservoir was kept close to an atmosphere and the pressure in the cell was varied separately.

To control the number density in the cell the vapor pressure of mercury was varied by changing the temperature. To reduce the vapor pressure, the reservoir was surrounded in an ice bath. Conversely, to increase the vapor pressure, the reservoir was wrapped with heating tape. The temperature was then monitored by *K*-type thermocouple to prevent over-heating.

Surrounding the outside of the vapor cell are two low-pressure mercury lamps (Philips TUV PL-L 95 W Hg lamp) which emit at 254 nm and provide the initial ground state excitation source. Simultaneously, an extended cavity diode laser (ECDL) beam is directed through the length of the cell, operating at 405 nm providing the source for the excited state transition. At both ends of the vapor cell the ECDL transmitted through quartz windows mounted at Brewster's Angle. The ECDL beam was split (50/50 polarizing beam splitter cube) prior to entering the cell so the wavelength could be monitored via a fiber coupler and the initial beam intensity could be measured using a photodetector (reference, I_R). Another photodetector was used to measure the beam

intensity at the exit of the cell (sample, I_S) and the ratio of the two detectors were used to generate the absorption spectra of the metastable population according to

$$A_{meta} = -\ln \frac{I_S}{I_R}.$$

While the mercury lamps were turned on the cell temperature rose considerably due to their high-power output. To reduce this effect, pressurized air was continuously flown over the outside of the cell while the lamps were in operation. Additionally, the temperature was monitored via *K*-type thermocouple to prevent over-heating.

As described in the kinetic model, in the absence of collisions, the $^1S_0 \rightarrow {}^3P_1$ transition will relax back down to the ground state in 120 ns. Therefore, to promote population buildup in the metastable state, additional pressure is required to decrease the average time between collisions. For these experiments, high purity nitrogen gas was used to control the total pressure of the system and provide the mechanism for transfer from $6\ {}^3P_1 \rightarrow 6\ {}^3P_0$ states through collision. To remove trace levels of oxygen from the nitrogen gas a filter (CRS Model 1000 Oxygen Trap) was used along the gas line prior to the inlet of the absorption cell. The filter that was used was able to be regenerated by being heated and pumped on over a period of several hours which allowed the filter to be reused without needing to break vacuum unnecessarily.

Additionally, a calibrated mercury vapor generator (PSA 10.536 Mercury Calibration System) was installed in parallel to the mercury canister. The mercury vapor output of the generator was controlled using a commercial software and its associated spectra was compared to those taken using the canister of liquid mercury. The generator was a later addition to the design when the concentration of mercury in the cell became questionable due to suspected reactivity with oxygen.

In the associated computer software, the vapor flow rate, dilution flow rate and temperature were controlled. The dilution flow was provided by the same nitrogen gas cylinder used when controlling the flow through the mercury canister and therefore the effect of oxygen reactivity should remain consistent. See Figure 2.6 for a schematic of internal flow of the calibration system. Based on the dilution of the mercury from the calibration system, a fractional mercury pressure produced can be calculated by

$$P_{Hg\ cell} = \left(\frac{P_{Hg\ generator}}{P_{Hg\ 300\ K}}\right) * \left(\frac{F_{reservoir}}{F_{dilution}}\right) * P_{cell}.$$

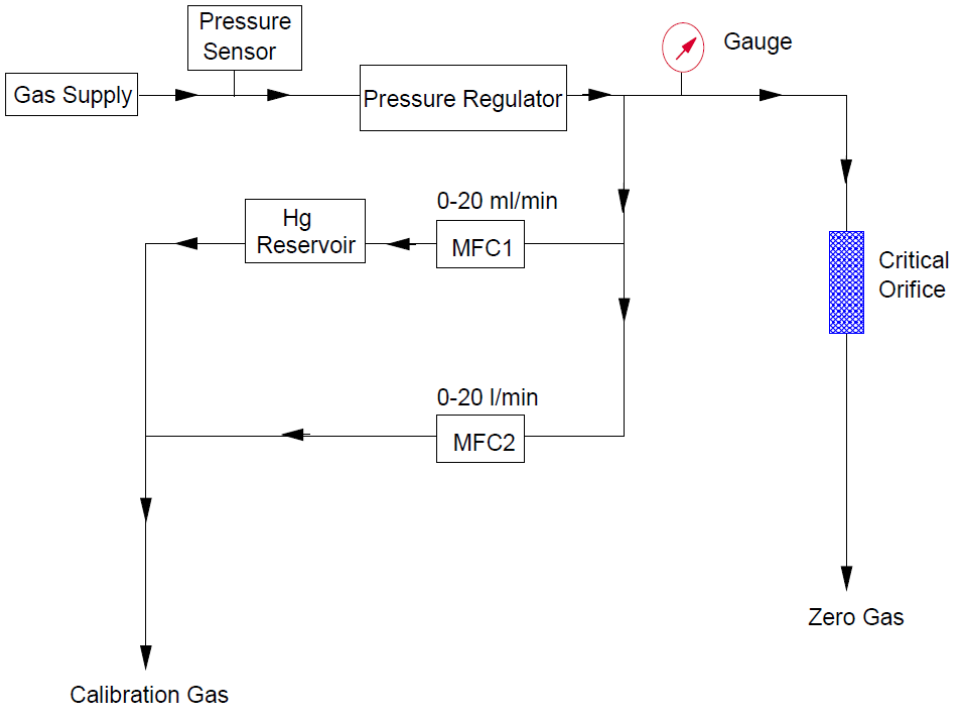

Figure 2.6. Schematic diagram of internal mercury calibration system. Where MFC1 denotes the mercury vapor mass flow control valve and MFC2 is the dilution flow control.

Another addition that was made later was the installation of a second absorption cell designed to monitor the ground state absorption. This second cell was placed in series to the

primary absorption cell in relation to the gas flow and therefore they were assumed to be in steady state with each other. In contrast to the primary absorption cell, it was optically opaque except at the ends and the only excitation source was a low-pressure mercury lamp operating at 254 nm. This cell similarly used quartz windows mounted at Brewster's Angle. The transmission through the cell was monitored by a photo multiplier tube (PMT) and a monochromator operating at the applicable wavelength. See Figure 2.7 for an overview of the experimental design.

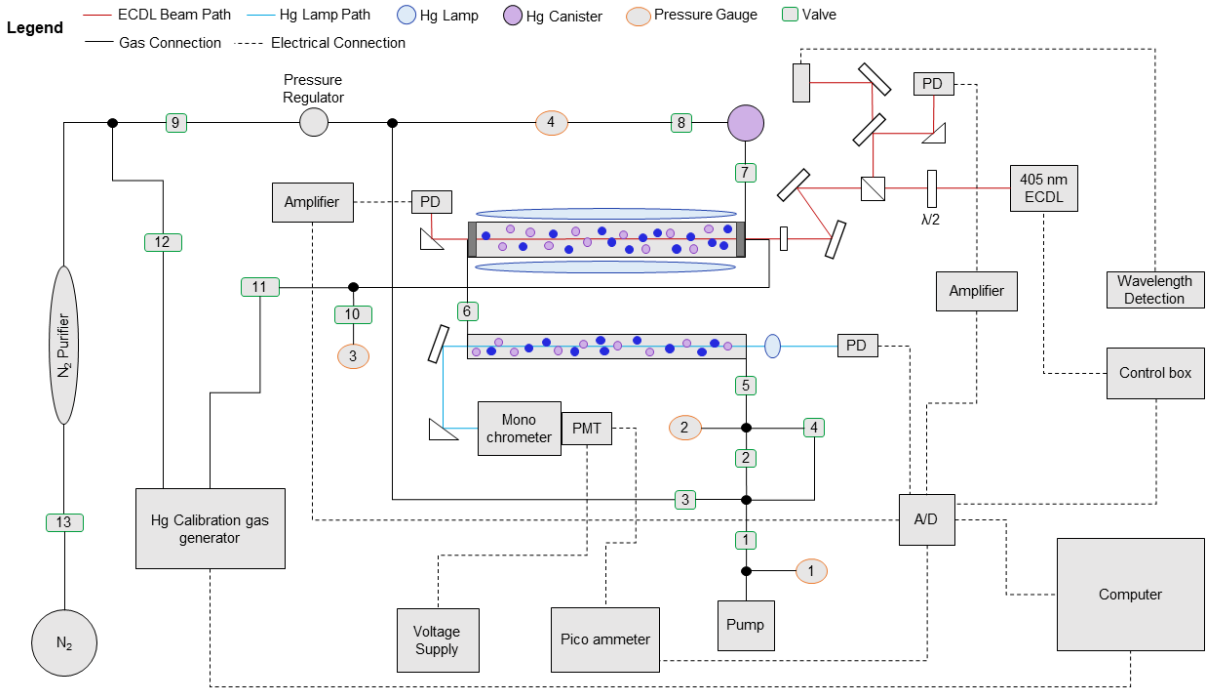

Figure 2.7. Experimental apparatus. Diagram includes additions made to address experimental complications described in Section 2.1.4. PD: photodetector; A/D: analog to digital converter; λ/2: half-wave plate; PMT: photo multiplier tube.

2.2.7. Mercury Lamp Emission

To estimate the efficiency of the ground state absorption, it's important to know the emission spectra of the mercury lamps. Notably, because the lamps are not a laser source, their emission is relatively broad and stretches over a significant portion of the visible spectrum in

addition to the dominant UV transition at $\lambda = 254\,\text{nm}$. See Figure 2.8 for a low-resolution emission spectrum taken from data provided from the product specifications sheet.

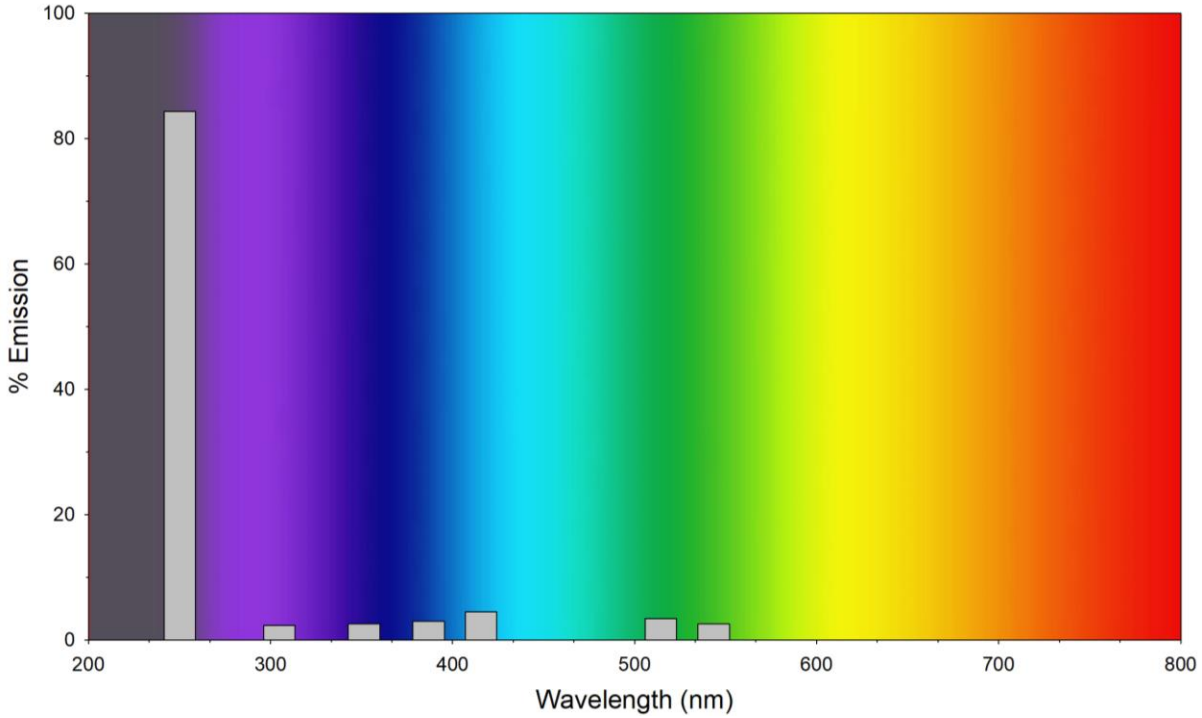

Figure 2.8. Broadband Emission of Philips TUV PL-L 95 W mercury lamp used for ground state excitation provided from the product data sheet.

Additionally, emission spectra were also taken in collaboration of Professor Chloe Dedic in the Aerospace Engineering Department. This was collected to confirm the accuracy of the spectrum provided by the manufacturer and provide insight into the ground state transition absorption efficiency, which in turn impacts the metastable population and sensitivity of the spectrometer.

2.3. Results and Discussion

2.3.1. Metastable Mercury Spectra

To test the spectrometers performance, spectra were taken over the frequency range depicted in Figure 2.9 (b), approximately 24705.10 cm^{-1} to 24705.74 cm^{-1}. The backing pressure of the variable control valve and the pressure in the reservoir were maintained. By collecting spectra across various cell pressures and nitrogen flow rates, the population of mercury in the metastable state could be estimated. For simplicity, the even isotopes can be estimated as one peak due to minimal shifts (Table 2.3) and only the fitted area of this peak will be used in analysis of the metastable mercury population as this one peak accounts for approximately 70% (69.75%) of naturally occurring mercury. As previously described in Section 2.2.5, the absorbance can be calculated where the normalized line-shape $g(\nu) = 1$ over the entire spectrum. However, because only the absorption of the even isotopes will be considered, $g(\nu) = 0.6975$ over this peak and S and L remain the same. Therefore, the metastable population can be calculated as a ratio of the absorbance of the metastable population over the expected absorbance assuming 100% of the mercury is absorbing or

$$f_{Hg\ meta} = \frac{A_{meta}}{A_{100\%}}.$$

Shown in Figure 2.9, is a spectrum collected of mercury from the metastable state with a cell pressure of 30 Torr and the mercury reservoir 273 K and therefore, should be comparable to the red lines shown in Figure 2.5. Even without detailed analysis it is plainly evident that the amplitude of absorption for the simulated spectrum is more than an order of magnitude greater for both the

case of 100% or 50% of the mercury atoms being in the metastable state. This suggests that a much smaller portion of the mercury population are in the metastable state.

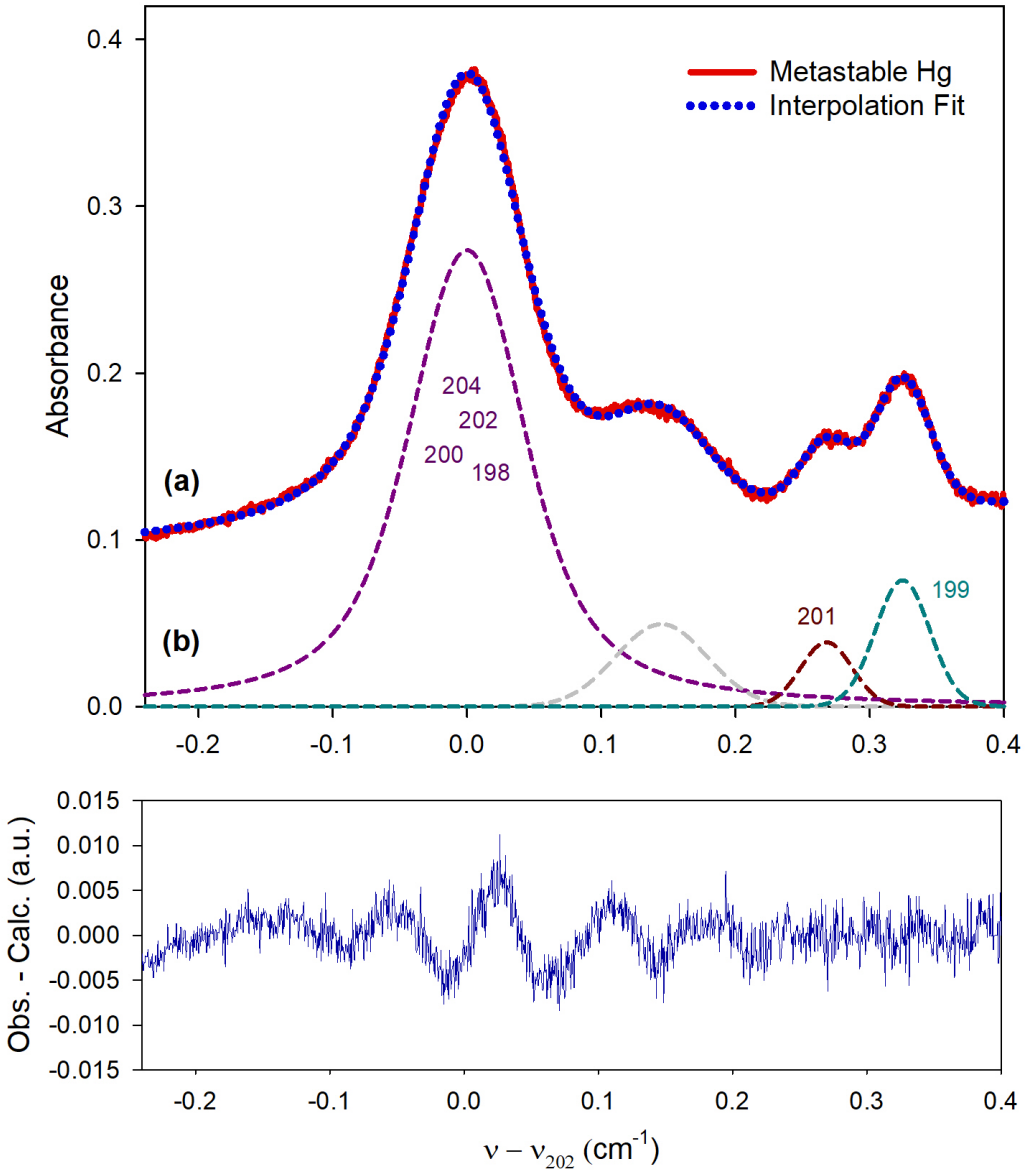

Figure 2.9. Top panel: (a) measured (line) and fitted (dotted) excited state (6 $^3P_0 \rightarrow 7\ ^3S_1$) absorption spectra for mercury vapor at 273 K and a total pressure of 30 Torr calculated as described above. The fitting model used is a combination of four Voigt profiles to account for the splitting of the odd numbered isotopes. The data and the fit have been offset by 0.1 for clarity. **(b)** The individual Voigt components of the overall fit and their associated isotope. Bottom Panel: fit residuals.

For a more precise measurement of the metastable population, the expected absorption assuming 100% of mercury atoms are in the metastable state is calculated the same as described in Section 2.2.5 except for a multiplicative of 0.6975

$$A_{100\%} = 0.6975 * S * L * N_{Hg\ 100\%}$$

Where $N_{Hg100\%}$ is calculated the same as previously described in Section 2.2.5. Then A_{meta} is determined as the area over all frequencies under the fitted Voigt profile corresponding to the even isotopes as shown in Figure 2.10. The overall fitting model is a combination of multiple Voigt profiles to compensate for overlap of the odd isotopes so the area can be considered to be only contributed to by the even isotopes. As an example, for the spectrum shown in Figures 2.9 and 2.10, the vapor pressure of mercury in the reservoir is $P_{Hg} = 2.59x10^{-2}$ Pa and $N_{Hg} = 6.88x10^{12}$ atoms cm^{-3} and therefore the total number density in the cell is

$$N_{cell} = N_{reservoir} * \frac{P_{cell}}{P_{reservoir}} * \frac{T_{reservoir}}{T_{cell}} = 6.88\text{x}10^{12} * \frac{30}{760} * \frac{273}{322} = 2.3\text{x}10^{11} \text{ atoms cm}^{-3}$$

With this number density, a cell length of 52 cm, and line strength of 1.35x10^{-13} cm, this results in

$$A_{100\%} = 1.128$$

And comparatively $A_{meta} = 0.0388$ from the fit of the spectrum. This leads to a calculated value of only 3.44% mercury in the metastable population. For reference, from the kinetic model shown in Section 2.2.3, under these conditions (not accounting for changes in flow) the expected population of mercury atoms in the metastable state is approximately 54.87% and therefore would closely resemble the dashed red line in Figure 2.5.

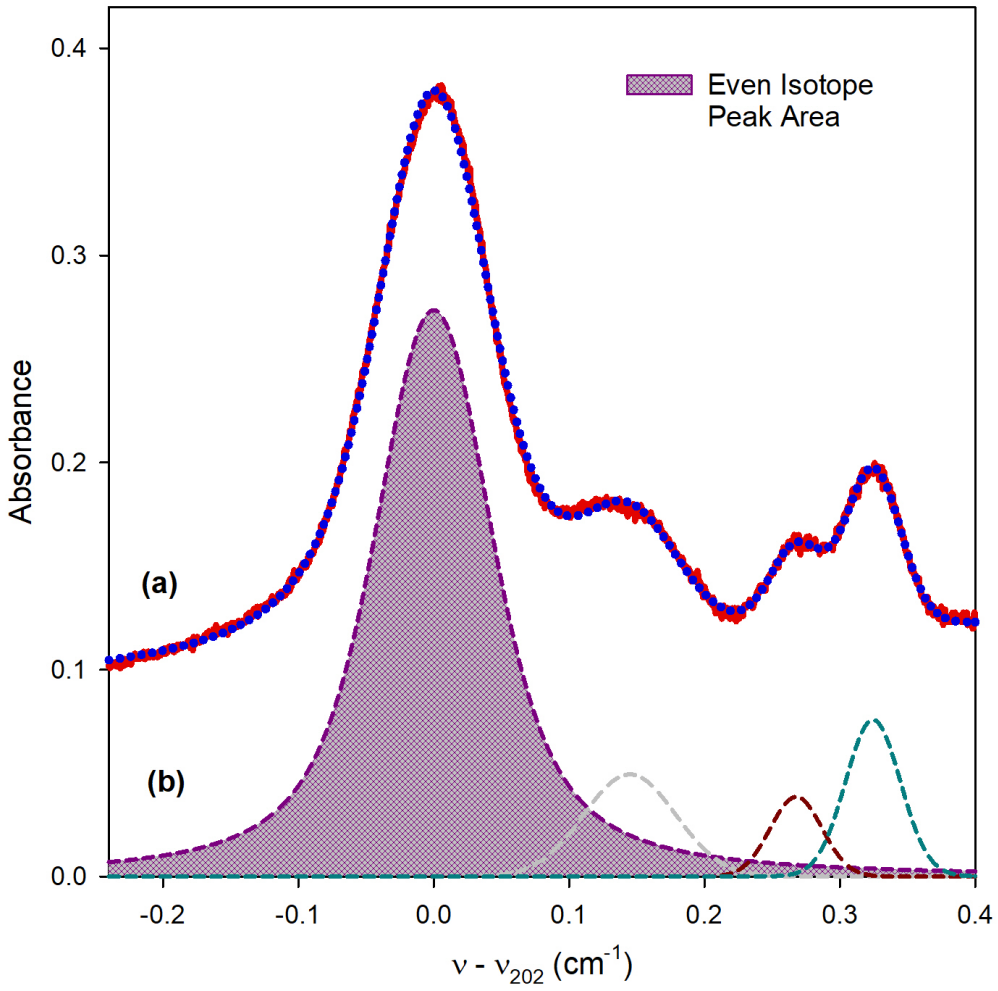

Figure 2.10. New depiction of the same spectra and interpolation fit in Figure 2.9. The fitted component attributed to the absorption of the even numbered isotopes is shaded. The total area under this curve is used to calculate the population of mercury in the metastable population.

This was repeated at 20, 30, 40, and 50 Torr and over increasing nitrogen flow rates. However, the resulting spectra of the same conditions vary greatly in amplitude and even occasionally shape, when compared over different days, making an accurate assessment difficult. When comparing spectra all taken on the same day, the results were more consistent and this is presented in Figure 2.11.

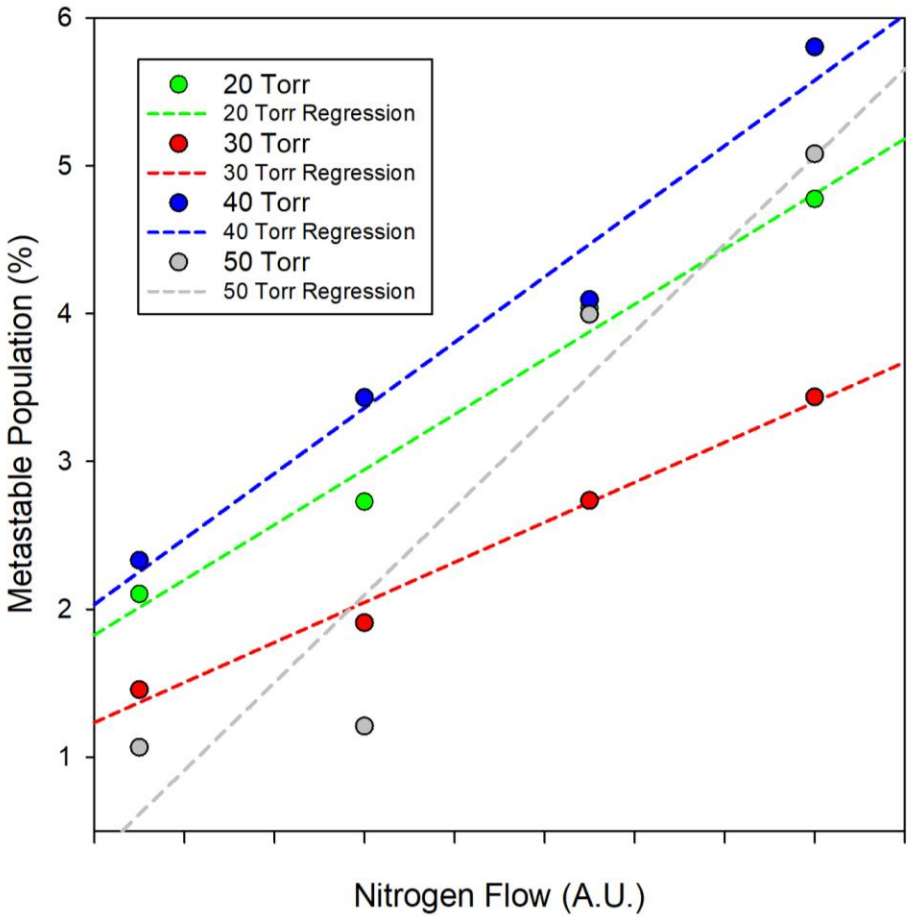

Figure 2.11. Calculation of percent of mercury population in the metastable state at various cell pressures over increasing nitrogen flow rates. All values were collected with the reservoir at a temperature of 273 K and calculated as described above.

The only trend which can be easily interpreted from Figure 2.11 is the increasing population in the metastable state as the flow of nitrogen is increased. This is not surprising as it will induce more collisions and therefore relaxation from the $6\ ^3P_1 \rightarrow 6\ ^3P_0$ states. However, as mentioned previously, when comparing these spectra to some collected in weeks prior, the metastable population was consistently significantly lower. Shown in Figure 2.12 are two spectra taken under the same conditions (pressure, temperature, and relative flow rate), only two weeks apart and their absorbance are differing by more than a factor of five.

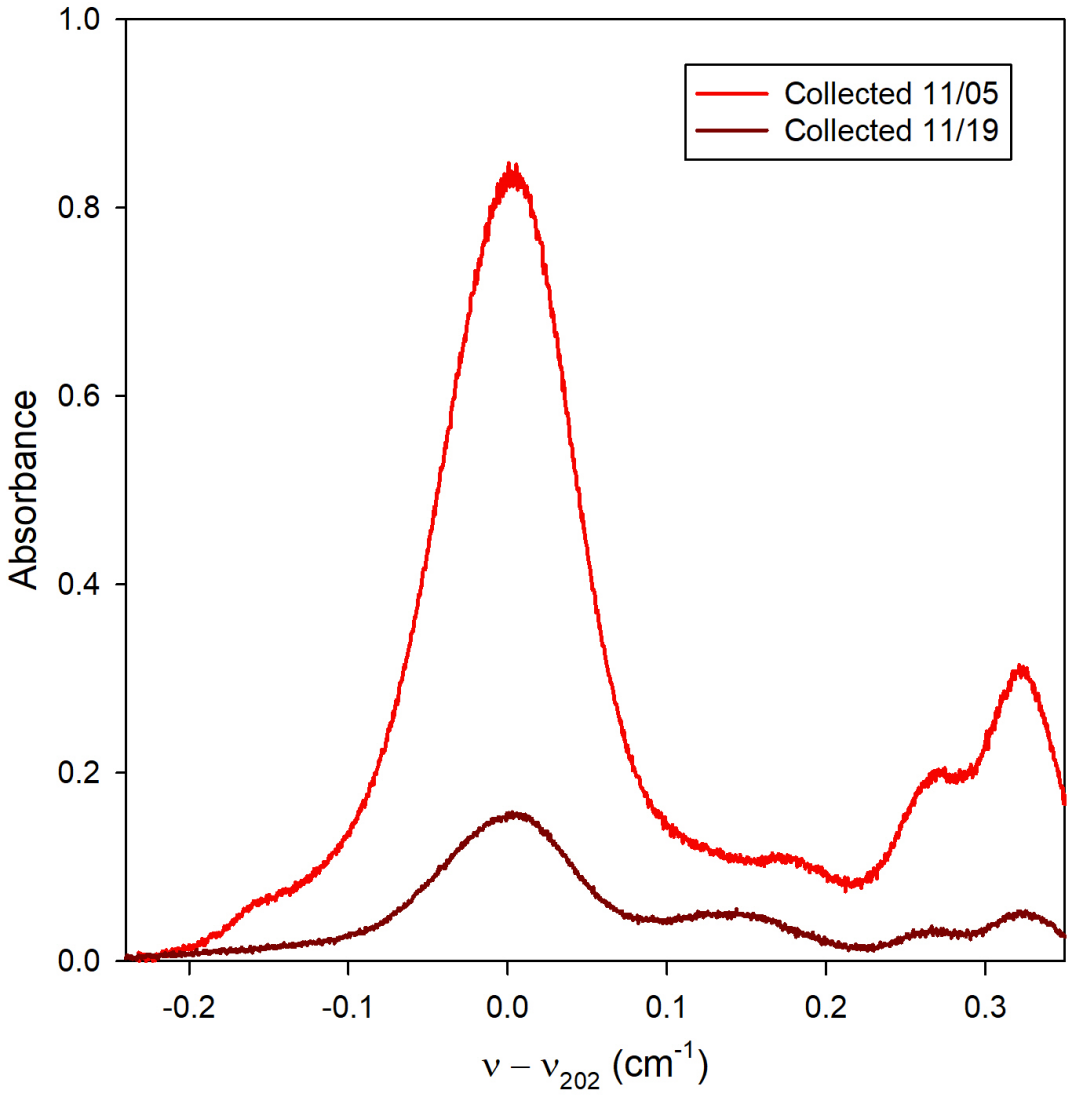

Figure 2.12. Comparison of two spectra both taken at a cell pressure of 30 Torr and reservoir temperature of 273 K taken two weeks apart.

It wasn't until much later that it was discovered that the absorption cell had signs of degradation which limited the transparency of the 254 nm light through the walls (Figure 2.13). This had not been noticed previously because the outside of the mercury lamps were kept wrapped in aluminum foil to limit the loss of intensity of the lamps output and thus increase the excitation efficiency of the ground state transition with the added benefit of protecting members in the lab

from excess UV radiation. Using a UV detector, it was determined that in the damaged region, the cell had become almost completely opaque to the 254 nm lamps. It is believed this darkening of the cell is actually film deposition as the result of reaction with oxygen. Notably, the deposition was only present on the gas inlet side of the cell. If this is the result of reaction with oxygen, this would make sense as the trace quantity of oxygen is reacted away into HgO as it enters the transparent cell and it would be expected that as the inlet becomes opaque, the region where the HgO is being deposited would gradually move towards the outlet. If this was the case, that would imply the effective absorption path length (L) would be constantly decreasing and could explain why, at least in part, the absorption under the same conditions changed so drastically between those two weeks. Another factor which could be impacting the amount of absorption over time is the efficacy of the nitrogen filtration system. As the filter would become saturated with oxygen and other contaminants it would no longer be able to filter properly. The filter was regularly cleaned as described previously, but it's difficult to know how the filter saturated which may have been affecting the spectral amplitude over time.

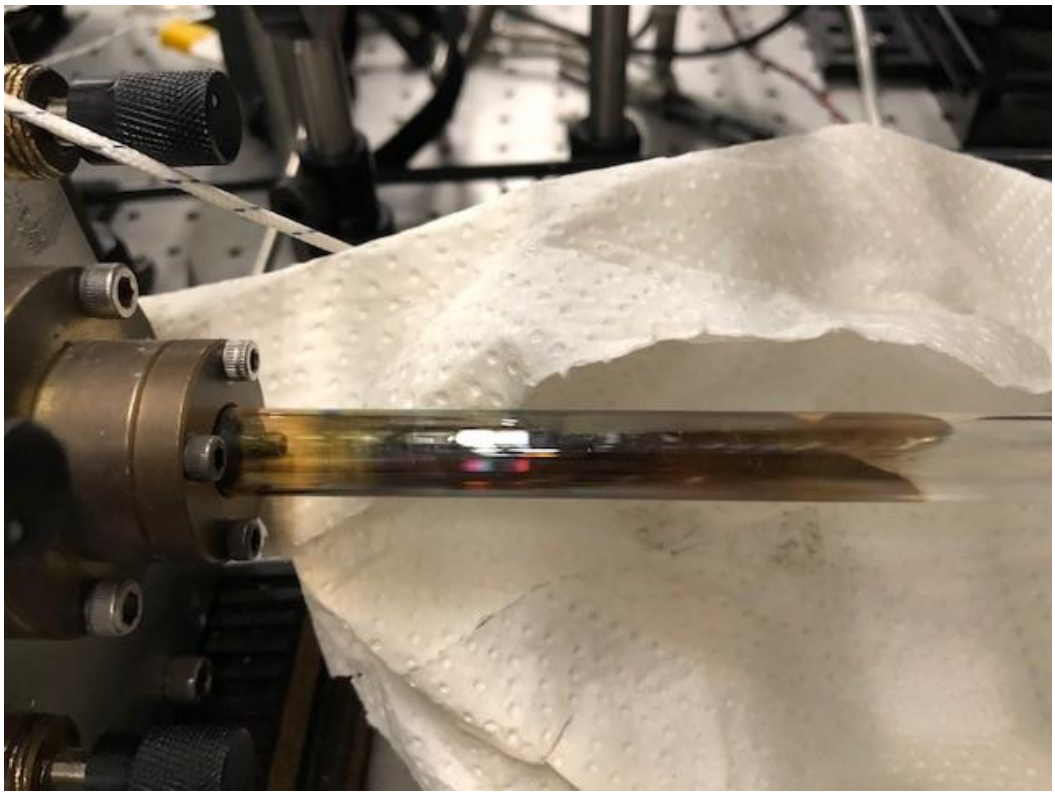

Figure 2.13. Photo taken by Professor Kevin K. Lehmann depicting HgO residue build-up inside the absorption cell located at the inlet likely as a result of excited mercury reacting with trace oxygen.

Another interesting point to note is in nearly all collected spectra there is an additional peak present as compared to the theoretical spectra shown in Figure 2.5. This is most easily seen in Figures 2.9 and 2.10 (gray, dashed line) where the spectra were fitted to a combined model of four Voigt profiles and each individual profile is plotted separately. However, in the frequency range shown, only three distinct peaks should be visible. It could be assumed that if this extra peak were associated with an isotope or hyperfine splitting its amplitude would be relatively consistent when compared to the other isotope peaks. However, while the amplitude of the other peaks remained relatively the same to one another, the peak in question varies from spectra to spectra as can be seen in Figure 2.14. Due to limitations in the ECDL the entire mercury isotopic spectrum was

never collected continuously. Ideally, the laser is intended to operate in single-mode, however, while scanning over larger frequency ranges, it would not be uncommon for the laser to begin mode-hopping. It is believed that this additional peak is attributed to the laser operating at an additional mode than intended, leading to additional absorption which could not be properly accounted for.

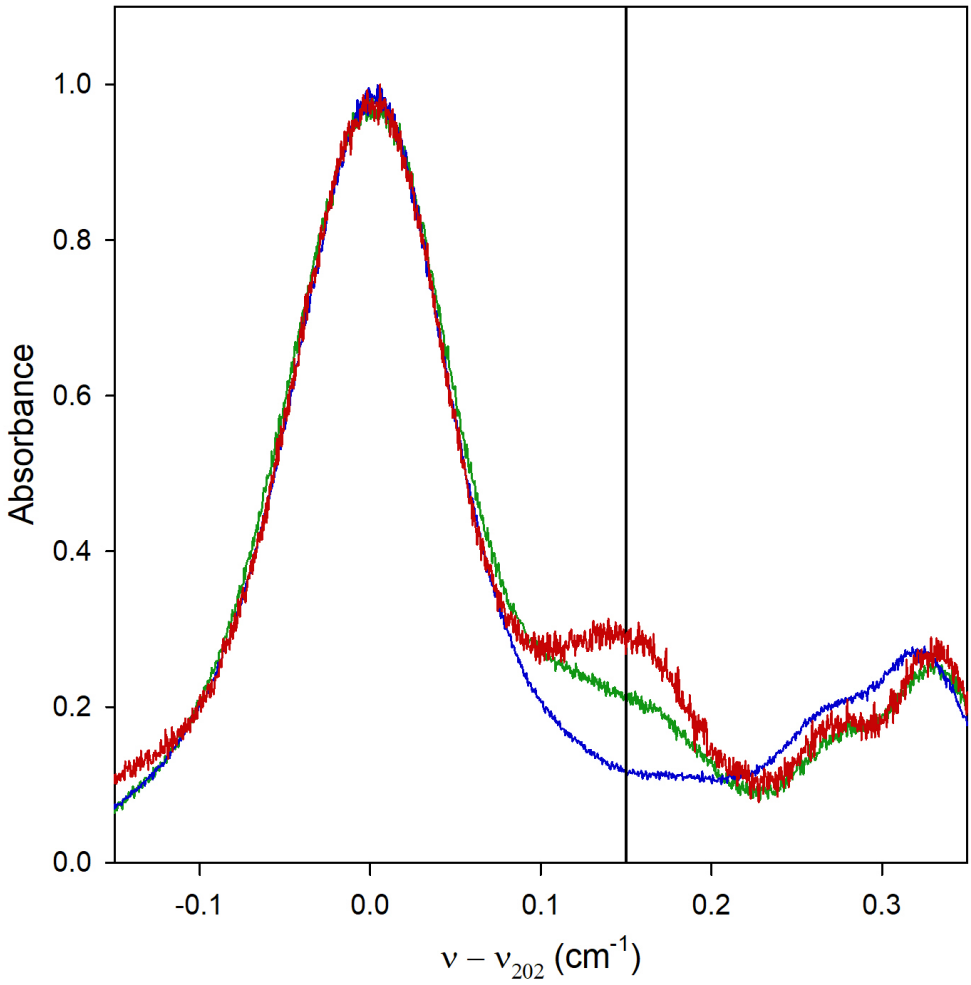

Figure 2.14. Multiple spectra overlaid to illustrate the variation of the amplitude of an un accounted absorption peak around 0.15 cm^{-1} away from the 202-isotope absorption peak. The relative intensities of each spectrum have been corrected for to ensure they are all of the same scale for ease of comparison.

2.3.2. Ground State Absorption

After observing how much lower the absorption intensity was than expected from the model, it became necessary to measure the ability to excite the ground state absorption. This was done using a second absorption cell and mercury concentration was controlled via the PSA Mercury Calibration System. The transmission of a focused low-pressure mercury pen lamp through the second absorption cell was measured using a monochromator and photo multiplier tube (PMT). After establishing the desired mercury flow rate and cell pressure, the transmission and initial lamp intensity were measured over 10 minutes and averaged over all values. The pressure was then allowed to increase and stabilize and the measurement was then repeated. To calculate the absorbance the transmission as the desired flow rate was compared to the transmission through the cell when the Calibration System had a mercury flow rate of 0 ml min^{-1} to account for leaking mercury vapor.

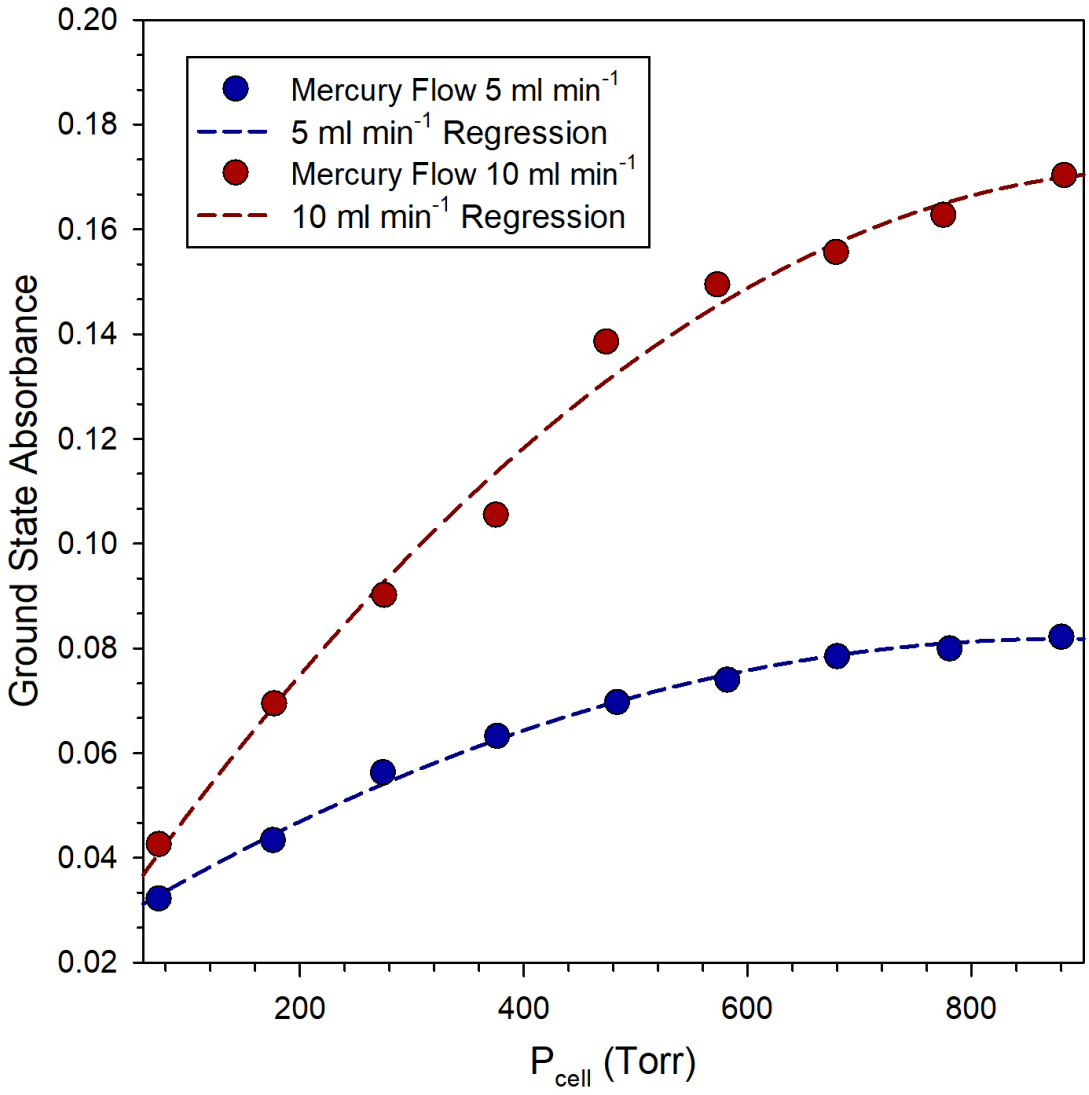

Figure 2.15. Analysis of the measured ground state absorbance in the secondary absorption cell with increasing cell pressure. Mercury flow rate was controlled via the PSA Mercury Calibration System and all values taken with a dilution flow of 1000 ml min^{-1} of nitrogen gas and mercury temperature of 40° C. Solid lines represent a second order linear regression fit.

It can be seen in Figure 2.15 as the pressure was increased in the cell over a range from 70 to 970 Torr the ground state absorption increases and eventually begins to flatten out, closely resembling a parabolic curve. Not surprisingly, the higher concentration of mercury vapor (10 ml min^{-1}) resulted in a higher overall absorbance. Although the results presented in Figure 2.15 present a clear image of the ground state absorbance under these specific conditions, it was planned

to perform this same measurement under more temperature, dilution flow, and mercury vapor flow rates. Unfortunately, following the collection of the presented data, it could not be successfully reproduced under the same conditions. The PSA Mercury Calibration System, as its name implies, is specifically designed for calibration. It's intended to be used briefly to calibrate an instrument, and not continually used. The to effects of oxygen contamination, prolonged interaction between excited mercury and high-power ground-state pump source in the presence of a bath gas with trace quantities of oxygen will decrease the response and accuracy of the measuring instrument.

2.4. Conclusion

Using the pre-excitation method described above mercury vapor spectra were successfully collected. However, due to complication with oxygen reactivity, the sensitivity of the spectrometer was constantly changing. It's believed that build-up of mercuric oxide on the inside of the absorption cell was causing the effective absorption path length to be constantly decreasing. Although mercury detection is typically done using this ground-state transition which induces reactions with oxygen, the methods used typically involve fluorescence spectroscopy and is thus not an issue. In this work, to promote sufficient population into the metastable state, a high pump power was needed, however, the use of two 95 W UV lamps provides significant photon flux to promote oxygen reactivity with excited mercury. Due to these factors, the technique presented above was found to be unsuitable for analytical detection of mercury vapor, particularly in atmospheric conditions, where a high concentration of oxygen would be present. However, as these issues are specific to mercury, it's possible this same approach could be applied to study other atoms with similar energy dynamics to mercury if the atoms are not reactive when excited. A possible suggestion would be cadmium as it has a similar electronic structure to mercury.

Chapter 3

Nonlinear Absorption Spectroscopy of Nitrous Oxide

Contributing Authors: Kevin K. Lehmann

3.1. Introduction

The following experiment described in this chapter details the development of a spectrometer for detection of nitrous oxide (N_2O) via ro-vibrational transitions in the mid-IR around 4.5 μm. Three separate transitions within a narrow frequency range are of interest in this chapter. First, vibrational ground state P(18) transition at 2207.62038 cm^{-1}. Second, the vibrationally excited R(17) at 2207.39403 cm^{-1}. Finally, the combination of the previous two transitions to give rise to the Q(18) two-photon transition at 2207.507205 cm^{-1}. All relevant transitions are of the ν_3 vibrational mode. Multiple spectroscopic techniques are employed to interrogate various aspects of interest, such as using Doppler-free Saturated absorption, frequency modulation (FM), and Doppler-free two-photon spectroscopy. This chapter will be a combination of three separate projects; determination of Doppler-free pressure broadening coefficients, impact of frequency modulation depth and saturation on line-shape, and Doppler-free two-photon spectroscopy, which are combined here due to their common subject of interest and experimental apparatus. The first two projects mentioned are focused on the P(18) transition of N_2O and the third is the two-photon Q(18) which is the combination of the ground state P(18) and vibrationally excited R(17). The similarities and differences between these various projects will be described in more detail in the following sections.

3.1.1. Motivation

Like carbon dioxide (CO_2), nitrous oxide (N_2O) behaves as a greenhouse gas and has a long residence time of approximately 114 years. It has been estimated that 40% of total N_2O emissions are due to human activity through agriculture, transportation, and industry. N_2O accounts for a relatively small fraction of the total greenhouse gas emissions in the atmosphere (7% in 2020), however, compared to CO_2, N_2O has a warming effect approximately 300 times greater per molecule. Therefore, it's highly important to have sensitive and selective methods to measure N_2O levels in the atmosphere.

Mid-infrared (IR) absorption spectroscopy is an encouraging method for N_2O detection. There are a wide variety of stable pulsed or continuous-wave (CW) quantum cascade lasers (QCL) available in this frequency range. N_2O has strong transitions in the mid-IR range with line strengths ranging from 10^{-18} to 10^{-22} cm^2 $molecule^{-1}$ cm^{-1} which allows for greater sensitivity. High-reflective mirrors are available in this range making it well suited for adaptation to cavity enhanced techniques such as cavity ring-down spectroscopy allowing for even greater sensitivity.

For atmospheric concentrations of N_2O to be determined spectroscopically by remote sensing or in situ methods pressure broadening coefficients must be determined. Furthermore, pressure broadening coefficients and line shift effects in ro-vibrational transitions help illuminate important information regarding intermolecular interactions as well as collisional impacts. To build accurate atmospheric chemical models it's critical to have spectral broadening information. Research determining the broadening coefficients of atmospheric molecules is common, however there is relatively little work which has been done on hole-burning spectral features which have the benefit of being Doppler-free. However, some work has been previously done to measure

Doppler-free pressure broadening coefficients, one such example being the work of Barger and Hall which measured the pressure shift and broadening of the P(7) transition of the ν_3 vibrational mode of methane.[26] It was found that the Doppler-free self-broadening coefficient determined by Hall was approximately 0.2 cm^{-1}/Atm compared to the value of the Doppler broadened peak given by HITRAN as 0.075 cm^{-1}/Atm.[26, 27] Therefore, Doppler-free pressure broadening information is needed to model and understand inelastic collisional effects.

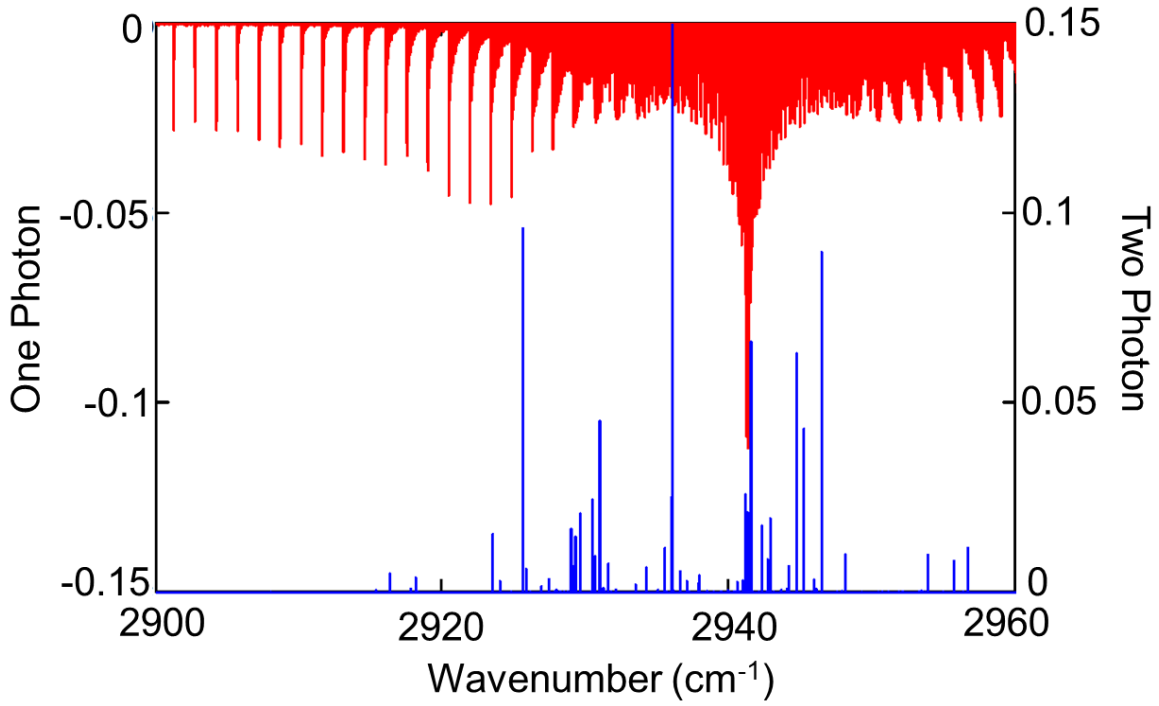

Figure 3.1. Calculated One-photon (in red) and Two-photon (in blue) absorption spectrum for C_3H_8 gas at 300 K. Each transition is plotted as a stick with a height equal to its fraction of the total intensity. The OPA spectrum is multiplied by -10^3 for clarity.

The long-term goal of this project was to eventually convert the spectrometer to a Doppler-free cavity ring-down (CRD) two-photon spectrometer due to its increased sensitivity and selectivity particularly for specific transitions of polyatomic molecules. This technique has been previously described in theory by Lehmann in detail.[28-30] Using one-color two-photon absorption

from counterpropagating fields cancels out first order Doppler broadening. This can result in linewidths on the order of a few megahertz (depending on pressure) as opposed to hundreds of MHz. Reduced linewidth is important for decreasing possible peak overlap of multiple transitions in a spectrum which leads to confusion in degree of absorption if they are not well resolved. Also, polyatomic molecules contain a high density of transitions which also contributes to spectral overlap. However, as seen in Figure 3.1 the density of two-photon transitions is significantly lower than one-photon transitions. Furthermore, the two-photon absorption strength is greatly increased when the two transitions are nearly degenerate, leading to improved sensitivity as well.

One drawback however to CRDS is it can be time consuming. If the transition frequency is known, the laser can be locked to an absolute frequency reference. Under these circumstances, time is not an issue, the laser can be quickly tuned to the transition frequency and highly sensitive measurements can be made. If, instead, the frequency of the transition is not known to high precision this poses an issue. CRDS cannot be scanned continuously and rather must have time to "ring-down" at each frequency to determine the absorbance. Thus, it is advantageous to have a method, although perhaps not as sensitive, but can quickly be scanned to "find" the two-photon transition frequency. This is the goal of a Doppler-free saturated two-photon spectrometer.

3.1.2. Linear and Nonlinear Absorption

For the Following sections to be clear, it's imperative that a basic relationship between linear and nonlinear spectroscopies to be understood. For the transition $E_i \rightarrow E_k$ the change in laser intensity (dI) moving through an absorbing medium (dz) can be described as

$$dI = -I\sigma\Delta N dz$$

Where ΔN is the difference in population density between levels $|i\rangle$ and $|k\rangle$, $\sigma(\nu)$ is the frequency dependent absorption cross section per molecule, and I is the intensity of the beam. Under these conditions the absorption coefficient $\alpha(\nu)$ can be determined as

$$\alpha(\nu) = \Delta N \sigma$$

where

$$\Delta N = N_i - \left(\frac{g_i}{g_k}\right) N_k.$$

It's important to note that at sufficiently low incident intensities I_0, the absorption coefficient is independent of I and by extension ΔN is also independent of I. This means that while in this regime the absorbed power dP is linearly dependent on incident intensity. This also means that the measured *absorbance* will be independent of incident intensity.

As the intensity continues to increase, eventually the population N_i in the absorbing level will begin to deplete as the pumping rate overcomes the relaxation rate. As a result of the depleted initial state, the overall absorption decreases until it reaches a constant value. The degree of saturation can be described by the saturation parameter S

$$S = \frac{B\rho_\nu}{R^*}$$

where

$$R^* = \frac{R_i R_k}{R_i + R_k}$$

Gives the induced transition probability ratio, $R_{i,k}$ are the respective relaxation rate constants for states $|i\rangle$ and $|k\rangle$, B is the Einstein absorption coefficient, and ρ_ν is the spectral energy density.

When $S \ll 1$, absorption is in the linear regime, whereas $S > 1$ is saturated, and $S = 1$ is when the pumping rate equals the relaxation rate.[31]

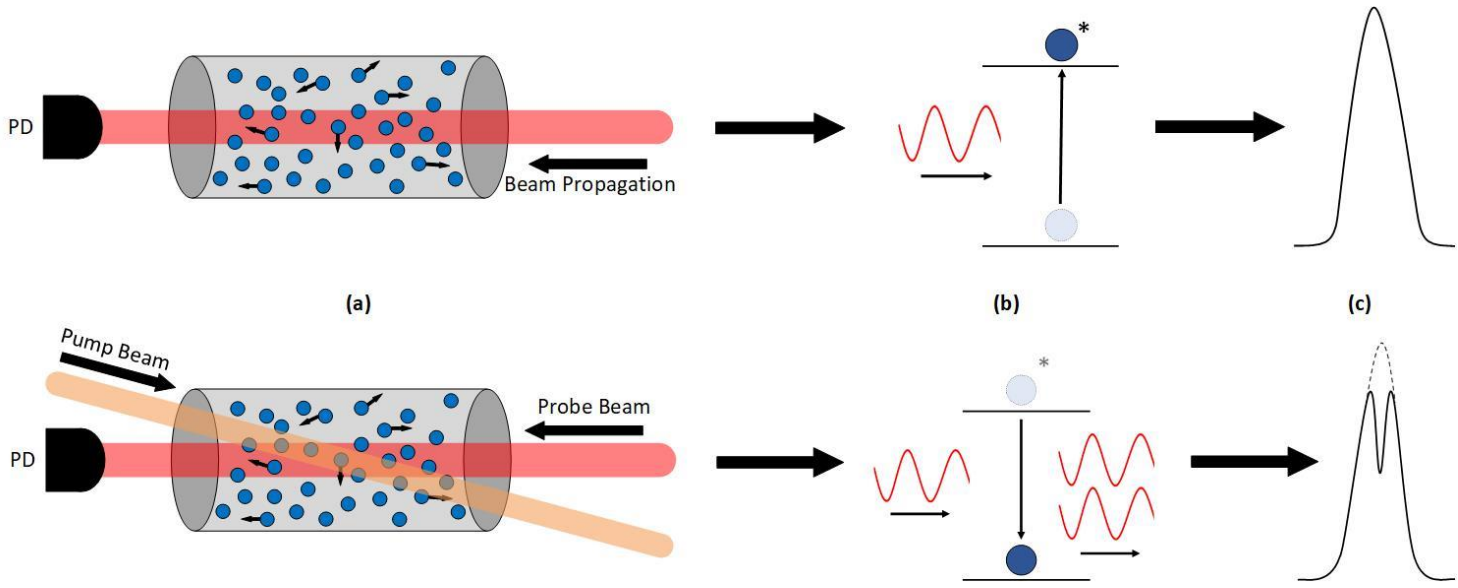

Figure 3.2. Comparison of direct absorption spectroscopy and saturated absorption spectroscopy. **(a)** Basic experimental design. Direct absorption spectroscopy utilizes one singular directional laser to measure absorbance. In contrast, saturated absorption spectroscopy utilizes counter propagating beams. In both, the gas analyte exhibits a Maxwell Boltzmann velocity distribution which contributes to Doppler broadening of absorbance line**.** Note, the pump beam is displayed at an angle to the probe beam for clarity**. (b)** Two level energy diagram. In saturated absorption spectroscopy the counterpropagating pump beam induces a reduction of population in upper energy level. **(c)** Resulting absorption feature. saturated absorption spectroscopy produces spectral hole-burning effect (Lamb-dip), Doppler-free Lorentzian centered at ν_0.

As a result of this saturation, and using counterpropagating waves of the same frequency a hole-burning feature or Lamb-dip in this can appear in the spectrum with careful alignment (Figure 3.2). When saturated, the population density in state $|i\rangle$ (N_i) decreases and conversely increases in state $|k\rangle$ (N_k). While the counter propagating waves scan over transition frequency due to their opposite directions of propagation, there apparent frequencies in the atomic frame are shifted from one another, see Figure 3.3. This occurs for all frequencies of the transition line shape except at

the central transition frequency and when the absorber is at rest relative to wave propagation (perpendicular). This results in those absorbers being probed by both waves simultaneously. This can affect the absorbers in different ways. Either pump from the ground state to the excited state or induce relaxation back to the ground state. If the excited population is dropping in just one frequency, the result is the Lamb-dip in the spectra. This feature is also Doppler-free due to the frequency shifts canceling.

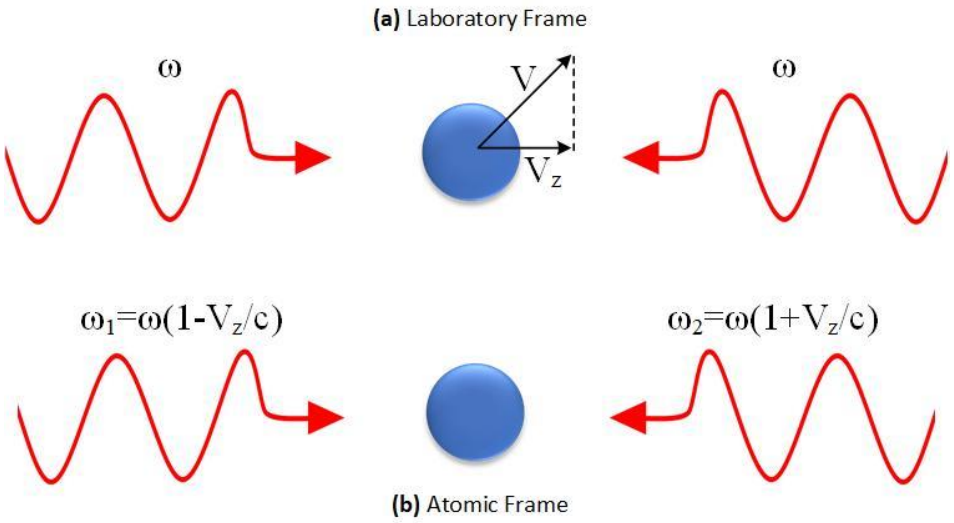

Figure 3.3. How one color two-photon spectroscopy from counterpropagating waves is Doppler-free. **(a)** The laboratory frame. The absorbing medium is traveling at a velocity of V which can be described as a vector pointing in the direction of movement. This vector can be broken up into its components to give the velocity in the direction of the propagating waves (V_z). The waves are both traveling towards the absorber with angular frequency ω but in opposite directions. **(b)** In the atomic frame the frequencies are up/down shifted depending on direction of molecule velocity. These two frequency shifts cancel resulting in Doppler-free line-shape.[32]

Therefore, according to Figure 3.3, those velocities v_z which fall within the homogeneous linewidth γ around the central absorption frequency can significantly contribute to absorption. Due to saturation, the population in the absorbing state $|1\rangle$ with velocities v_z is decreasing while

simultaneously the population density in state $|2\rangle$ with velocity v_z is increasing. Thus, the saturated homogeneous linewidth can be described as

$$\gamma_s = \gamma\sqrt{1 + S_0}$$

Where S_0 is the saturation at the central frequency ω_0 and $\gamma = \gamma_i + \gamma_k$ is the homogeneous width of the transition.[31]

3.1.3. Pressure Broadening

Consider a two-level energy system such as that described in previous sections with the spontaneous emission lifetime of the excited state of τ seconds. The state of the system in the absence of electromagnetic radiation can be described by the wavefunction

$$\Psi(t) = a_i\Psi_i(t) + a_k\Psi_k(t).$$

where $a_{0,1}$ are constants. If the system becomes excited the dipole moment of the system is given by

$$M(t) = \langle\Psi|\mu|\Psi\rangle$$

$$= 2a_i a_k \mu_{ik} \cos(\omega_{ik} t)$$

where the dipole moment of the system oscillates at the Bohr angular frequency ω_{ik} and μ is the dipole moment operator. When a surrounding gas is present collisions may occur. If a collision is sufficiently strong, the phase of the oscillating dipole moment will be randomly altered (dephasing). As a result, the infinitely long cosine wave oscillating at the Bohr angular frequency is disrupted by successive collisions of average length T_2 or the average time between collisions. As the pressure is increased the frequency of collisions increases as well and the oscillation is

described by an increasing number of segments. A Fourier transform can be applied to convert the waveform into its corresponding frequency distribution resulting in a Lorentzian lineshape with a FWHM given by[1]

$$\Delta\nu_{1/2} = \frac{1}{\pi T_2}.$$

3.2. Experimental

The following section details the experimental procedures used in this project. This will also provide additional information regarding some details which will provide context for the discussion in the following sub-sections.

3.2.1. Properties of Nitrous Oxide

N_2O is considered a linear molecule, which can be seen in Figure 3.4, and therefore has four (3N-5) normal vibrational modes. One symmetric stretch, one asymmetric stretch and two degenerate bending modes. For this research we will be focused on the ν_3 asymmetric vibrational mode.

Figure 3.4. Chemical Structure of N_2O with bond information provided by NIST.[33]

In Table 3.1Table 3.1 isotopes of N_2O are listed along with their abundance. It's important to note that for all transitions of interest here, only the first most abundant isotope is absorbing. This information is important for spectral analysis and generating theoretical spectra as well.

Isotope	Mass (amu)	Abundance
$^{14}N_2{}^{16}O$	44	0.9903
$^{14}N^{15}N^{16}O$	45	0.0036
$^{15}N^{14}N^{16}O$	45	0.0036
$^{14}N_2{}^{18}O$	46	0.0020
$^{14}N_2{}^{17}O$	45	3.6928×10^{-4}

Table 3.1. Natural isotopes of nitrous oxide, their associated mass, and natural fractional abundances.[27]

The majority of this chapter will be focused on the P(18) ro-vibrational transition ($\nu_0 =$ 2207.62038 cm^{-1}) starting in the vibrational ground state and rotational $J = 18$ exciting to $V = 1$ and $J = 17$ ($\Delta J = -1$ resulting in P-branch designation). The R(17) transition ($\nu_0 =$ 2207.39403 cm^{-1}) starts from the P(18) excited state with $V = 1$ and $J = 17$ and excites to $V =$ 2 and $J = 18$ ($\Delta J = +1$ resulting in R-branch designation). Finally, the two-photon Q(18) transition ($\nu_0 = 2207.507205$ cm^{-1}) is the combination of the previous transitions starting from the initial state of P(18) and exciting to the final state of R(17) ($\Delta J = 0$ denotes Q-branch). The detuning between P(18) and R(17) transitions is only $\Delta\nu = 0.113$ cm^{-1} resulting in resonance enhancement of the two-photon transition strength proposed by Lehmann[29] and measured in Zhao et al.[34] The multi-level energy system needed to describe the combination of projects in this chapter shown in Figure 3.5.

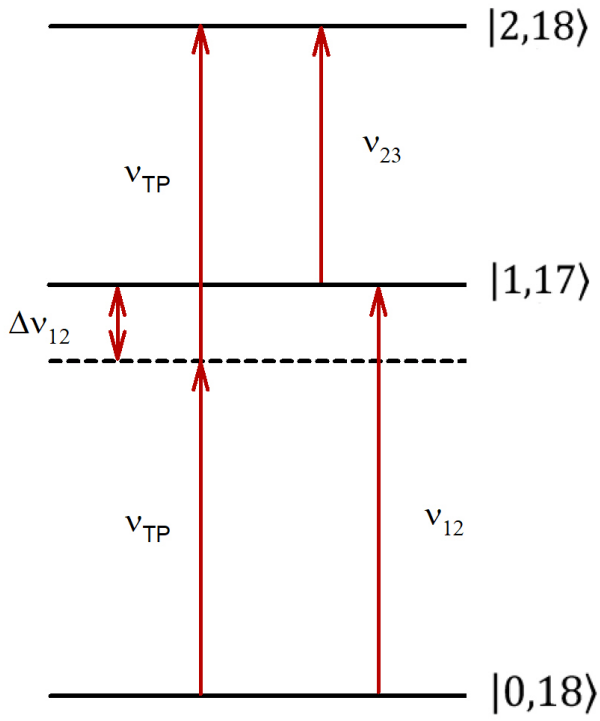

Figure 3.5. Energy level diagram of relevant N2O transitions referencing P(18) (ν_{12}), R(17) (ν_{23}), two-photon Q(18) (ν_{TP}), and detuning ($\Delta\nu_{12}$) frequencies. Energy levels are for illustrative purposes and not drawn to scale for clarity.

3.2.2. Theoretical Linear Spectra

Similar to Chapter 2, multiple spectra were produced over the frequency region of interest. For comparison, it is helpful to compare the saturated experimental spectra to their non-saturated counterpart. One important reason for this is it provides a reference to see how saturated the experimental spectra is by comparing the absorbance of the Doppler broadened peaks. As mentioned in Section 3.1.2, the saturated absorption is dampened from the linear absorption. Therefore, as the saturation level changes, the degree of absorption changes as well.

Transition	Frequency (ν: cm^{-1})	Transition Strength (S: $cm^{-1}*molec^{-1}*cm^2$)	Self-Broadening (γ_{self}: cm^{-1}/atm)	Air-Broadening (γ_{air}: cm^{-1}/atm)
P(18)	2207.62038	$9.072x10^{-19}$	0.98	0.0765
R(17)	2207.39403	$3.927x10^{-23}$	0.098	0.0765

Table 3.2. Transition constants relevant for generating a theoretical spectrum for the P and R branch transitions from HITRAN database.[27] The two-photon, Q(18) transition information is not available in the database.

The unsaturated spectrum was generated similarly to the spectra described in Section 3.1.2 and will be described briefly here. For this spectrum only one transition is of interest and therefore only one Voight profile is needed for the normalized line shape function. The central frequency (ν_0), integrated line strength (S), and absorbing isotope are all provided in the HITRAN Database.[27] The number density of N_2O is more simply determined from the pressure in the absorbance cell and similarly an additional number density of a non-absorbing gas can be chosen from a desired additional pressure. The absorption path-length is known to be ½ of a meter long. From these values the absorbance can be calculated by

$$A(\nu) = g(\nu) * S * L * N_{NNO}$$

Where *g(ν)* is the Voigt spectral lineshape function given in Section 2.2.5.

The degree of Doppler and pressure broadening must be determined. The Doppler FWHM can be determined by,[1]

$$\Delta\nu_D = 7.2x10^{-7} * \nu_0\sqrt{\frac{T}{M}} = 0.00413\ cm^{-1} = 124.01\ MHz$$

where T is the temperature of the gas in Kelvin (298 K) and M is the mass in AMU (44 amu). The Doppler FWHM was assumed constant for all experimental data neglecting any minor fluctuations in room temperature.

The pressure broadening was determined by converting the pressure into number density combined with the pressure broadening coefficients. The pressures of N_2O used typically were only a few mTorr and therefore were never enough for pressure broadening to overcome the Doppler broadening. The air broadening coefficient (Table 3.2) was used to simulate the addition of non-absorbing gasses. The Lorentzian FWHM due to added pressure can be determined by

$$\Delta\nu_L = b * \frac{P_{torr}}{760} * 2$$

where b is the HWHM pressure broadening coefficient in cm^{-1} atm^{-1}. The resulting spectrum can be seen in Figure 3.6. Using the simulated spectra, it can be easier to see how saturated our experimental spectra are by how damped the absorbance is compared to the unsaturated absorbance.

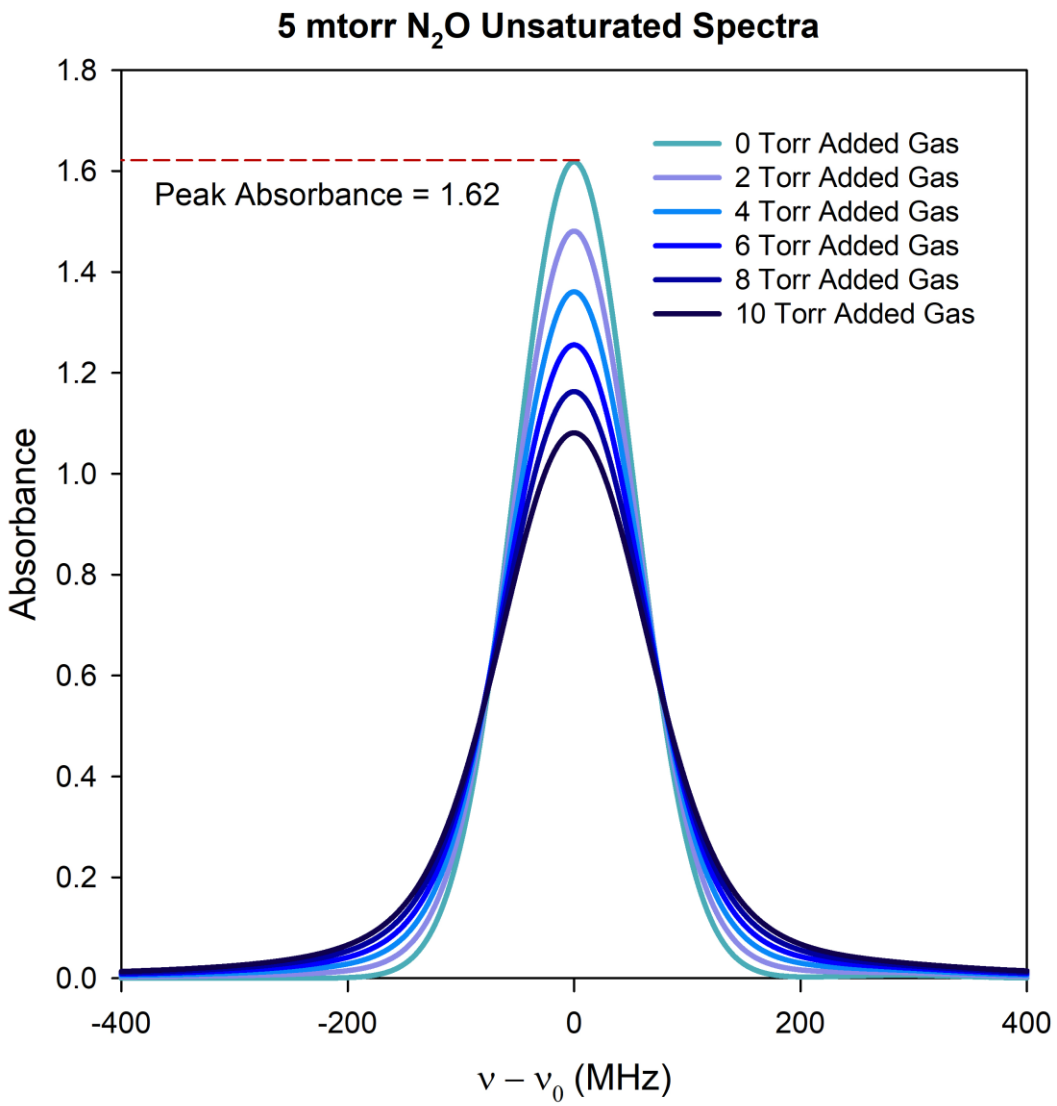

Figure 3.6. Theoretical unsaturated spectra of 5 mTorr of N_2O with various amounts of additional gas (air) included indicating the effect of pressure broadening. While in the linear regime, increase in air pressure does not result in a change in total absorbance, as the lines become more broad, the peak height decreases so the area is conserved.

3.2.3. Experiment Design

In this chapter the absorbance of N_2O was measured by dosing gas into an evacuated stainless steel absorption cell. Following dosing, the pressure of N_2O could be adjusted using a turbo pump station operating around $1x10^{-7}$ Torr. The pressure inside the cell was monitored using

two Baratron pressure gauges (10 Torr and 50 mTorr full scale, only one pictured in Figure 3.7). Once the desired pressure was reached the cell was sealed to maintain the pressure while spectra were collected.

A tunable, continuous-wave (CW), quantum cascade laser (QCL) from Daylight Solutions operating around 4.53 μm was used as the excitation source. It was capable of being tuned over a wide range including the R(17), P(18) and Q(18) rovibrational transitions of interest. The laser was horizontally polarized. The polarization was rotated using a half-wave plate at the output of the laser. This allowed the beam to be deflected by the acousto-optic modulator with high efficiency. The modulator was used to modulate the power in the cell and control the saturation level. Lenses were used to control the focusing into the cell and an etalon designed to stabilize fluctuations in the laser frequency. By controlling the beam size entering a cavity the light can more efficiently couple to the cavity. To improve the amplitude of the Lamb-dip, having the counter propagating beams overlap as much as possible is ideal. To ensure this, it's important for the beam size to be known so the back reflection can be focused to maintain the same beam size as the forward propagation. Also, it benefits to have the beam size to be symmetrical in the cell, but this will be discussed in more detail later. After the beam passes through the cell a beam-splitter reflects the beam to a focusing mirror which sends the beam back towards the laser. The radius of curvature of the mirror ($R = 50$ cm) was chosen to maintain the focusing in the back reflection. An isolator in front of the laser prevents the back reflection from entering the laser and causing instability.

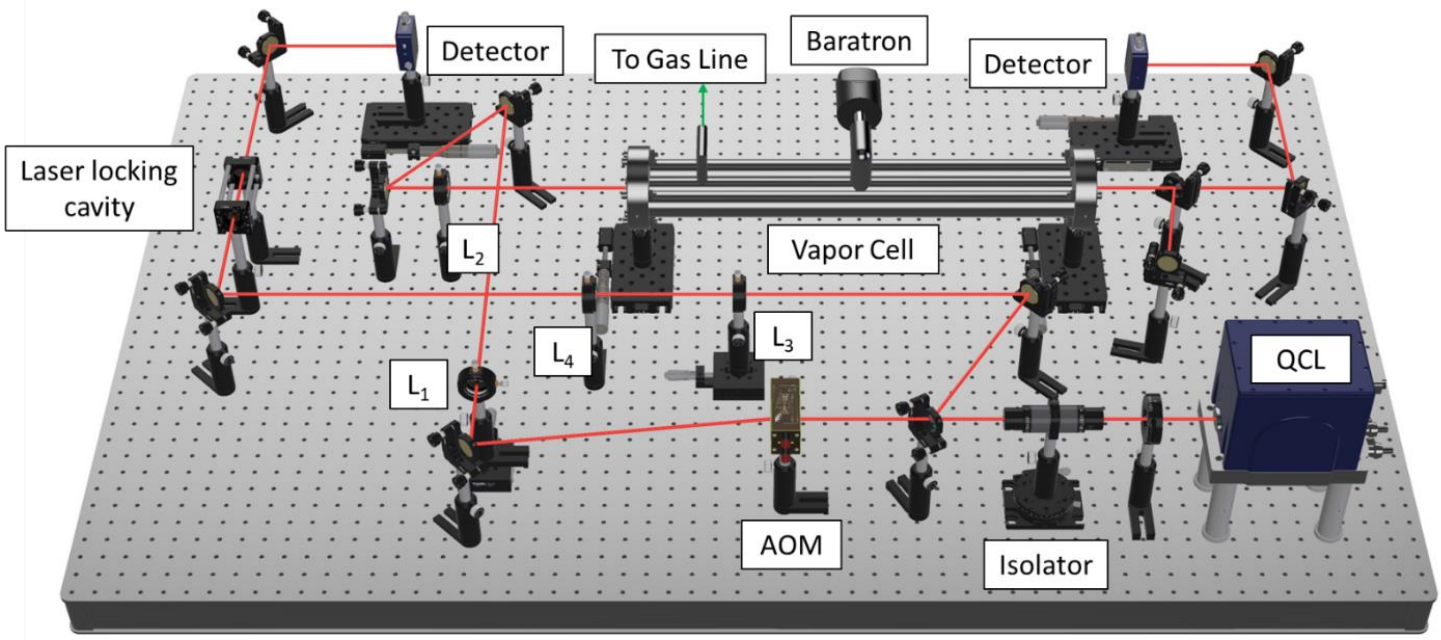

Figure 3.7. Simplified experimental apparatus depicting quantum cascade laser (QCL) beam path in red. The first order deflected beam from the acousto-optic modulator (AOM) is used in the absorption cell to allow for power modulation. Lenses ($L_{1\text{-}4}$) are used to control the beam size in the cell and laser locking cavity. A beam-splitter following the absorption cell reflects to a curved focusing mirror (radius of curvature $R = 50\ mm$) which sends the transmitted beam back through the cell towards the QCL until it is blocked by the isolator. The radius of curvature was chosen maintain the beam size in the reverse propagation to the forward propagation to maximize beam overlap.

3.2.4. Beam Profiling

This section will describe how the beam size of the QCL was determined. To see how the beam is propagating through space, first, the beam "spot size" must be determined at various distances along the propagation direction. The spot size is defined as the distance from the center of the beam where the intensity drops by a factor of $1/e^2$. By capturing thermal images of the beam cross-section these images can be related to the beam's intensity profile. For this laser, the output is the TEM_{00} transverse mode. The intensity profile for this beam should closely resemble a Gaussian distribution. In this case there are three dimensions needed to describe the Gaussian

profile. The X and Y axes represent the area of the cross-section and Z is needed to display the intensity. Therefore, to find the spot size of the beam from the thermal image a 3-D Gaussian least-squares interpolation fit is used in the form

$$I = A * Exp\left[-\frac{(x-x_0)^2}{2\sigma^2} + \frac{(y-y_0)^2}{2\sigma^2}\right] + b$$

Where A is the amplitude, x_0 is the location in x of the peak center, y_0 is the location in y of the peak center, and σ is the Gaussian standard deviation, and b is the offset to account for thermal noise of the room (Figure 3.8). The standard deviation can then be converted to the beam spot size omega (ω) where $\omega = 2\sigma$. This process is then repeated for several cross-sections until the propagation can be determined.

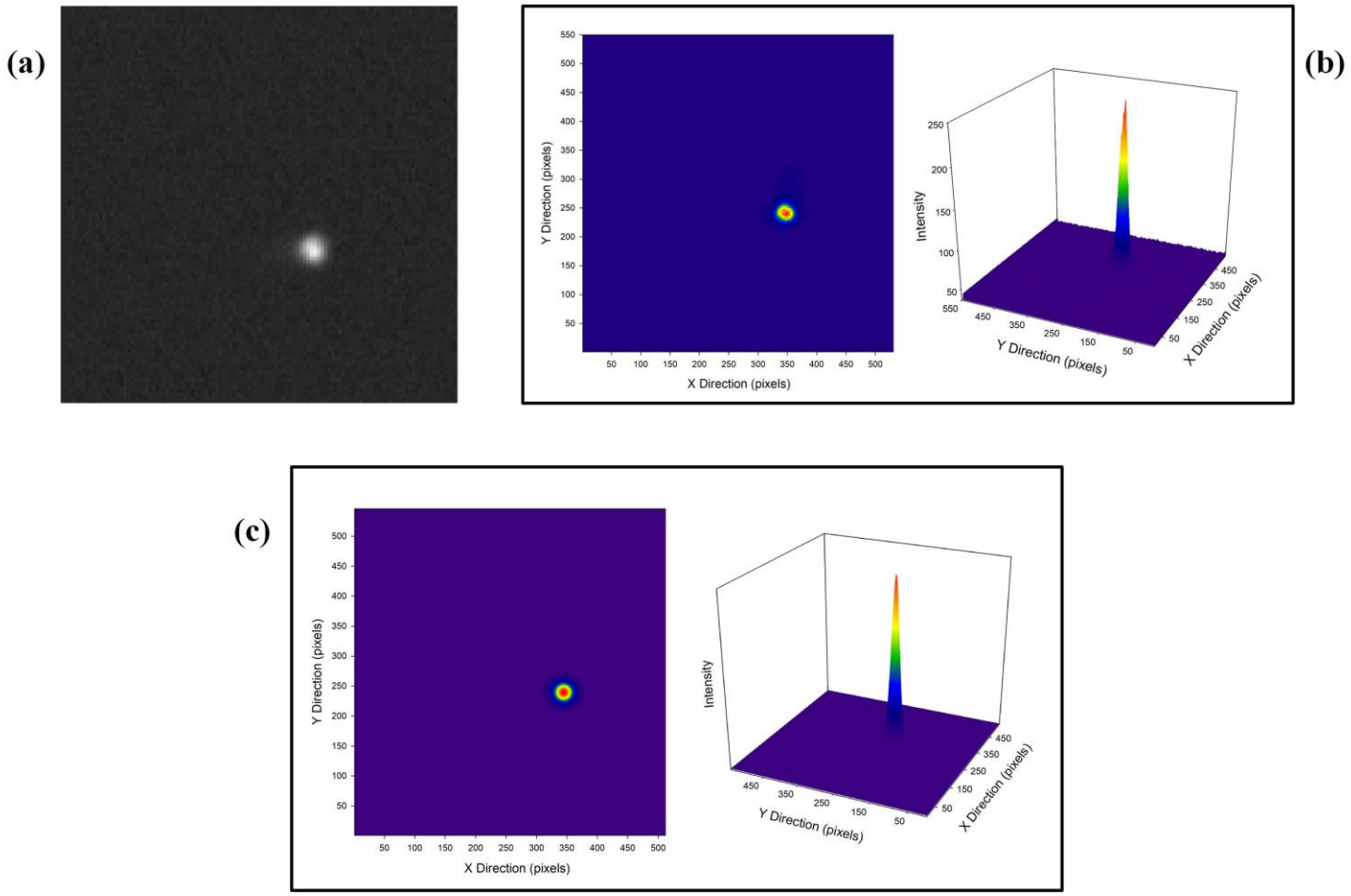

Figure 3.8. IR cross-sections of beam fitted to Gaussian Profile. **(a)** The raw thermal image of the beam taken with Spiracon Pyrocam. **(b)** The thermal image is then converted to a matrix where each pixel is assigned a value denoting how bright it is. Can be shown as both a contour plot or a mesh plot to show the 3-D Gaussian shape. **(c)** The matrix is then fitted using least-squares methods to a Gaussian function to determine the spot size at this particular position. From a collection of these fits the overall beam propagation can be determined.

To determine the overall beam propagation the values for omega can be used with

$$\omega(z)^2 = {\omega_0}^2 * \left(1 + \frac{z^2}{{z_0}^2}\right)$$

Where ω(z) is the spot size at a position along the k-vector, ω_0 is the minimum spot size or waist, z is the position along the k-vector with 0 being at the waist, z_0 is the distance away from the waist

for the beam size to increase by a factor of √2. This is the equation for propagation of a Gaussian Beam in a homogeneous medium.[35] To account for the fact that the location of the waist was unknown and thus where $z = 0$ is located an alteration to this equation was made.

$$\omega(z) = \sqrt{{\omega_0}^2 * \left(1 + \frac{(z - z_s)^2}{{z_0}^2}\right)}$$

Where the new variable z_s is the shifted position from 0 where the waist is located.

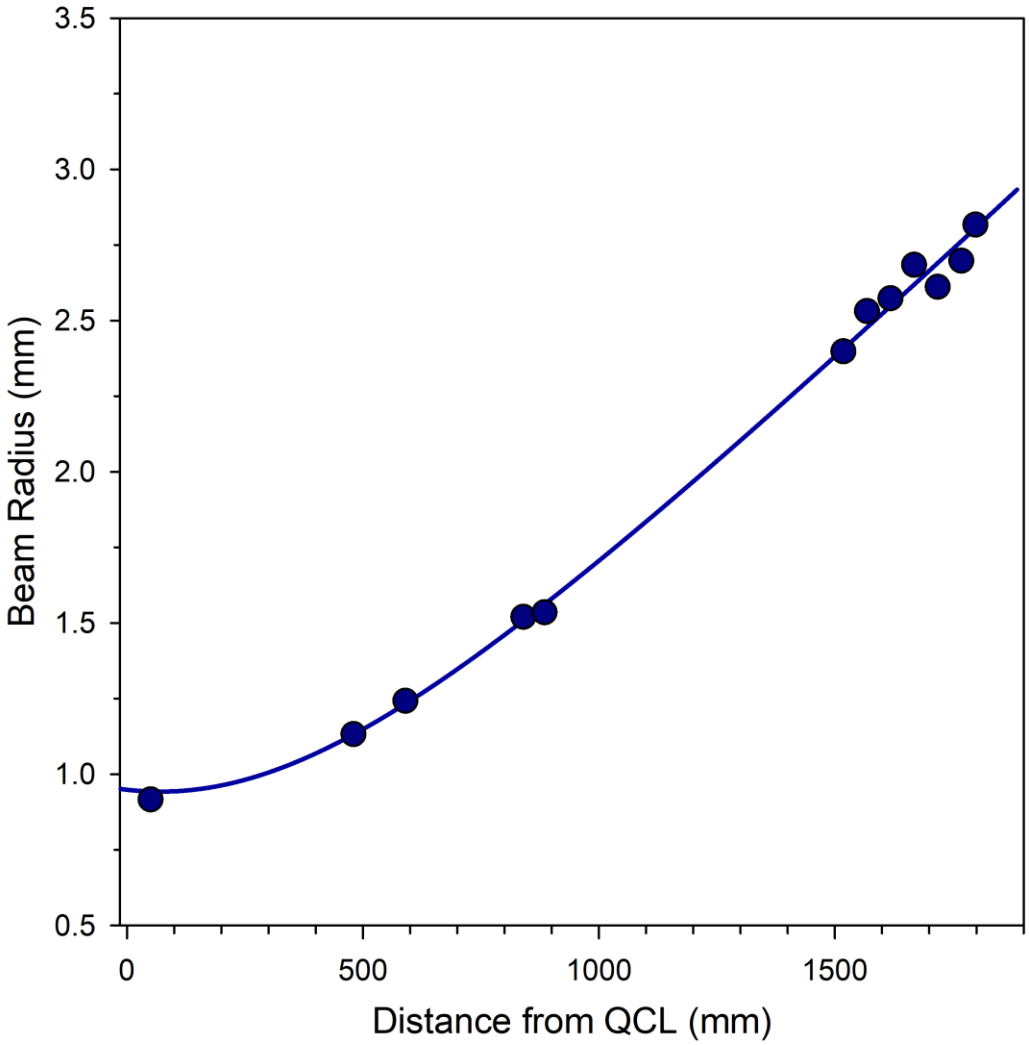

Figure 3.9. Beam propagation of QC laser output without any focusing. This was used to help determine proper lens/telescope options to focus beam to desired size in absorption cell. The beam waist ω_0 was determined as 0.942 mm and z_0 = 616.119 mm.

This beam profiling procedure was done several times. First to determine the parameters of the beam of the QCL without any focusing optics to alter the propagation. The results can be seen in Figure 3.9. Knowing the original beam parameters allowed for the beam size to be calculated as it propagated through various optics. This aided in choosing the ideal lenses to use and their location to provide the preferential focusing in the cell. The resulting beam size in the cell after focusing can be seen in Figure 3.10.

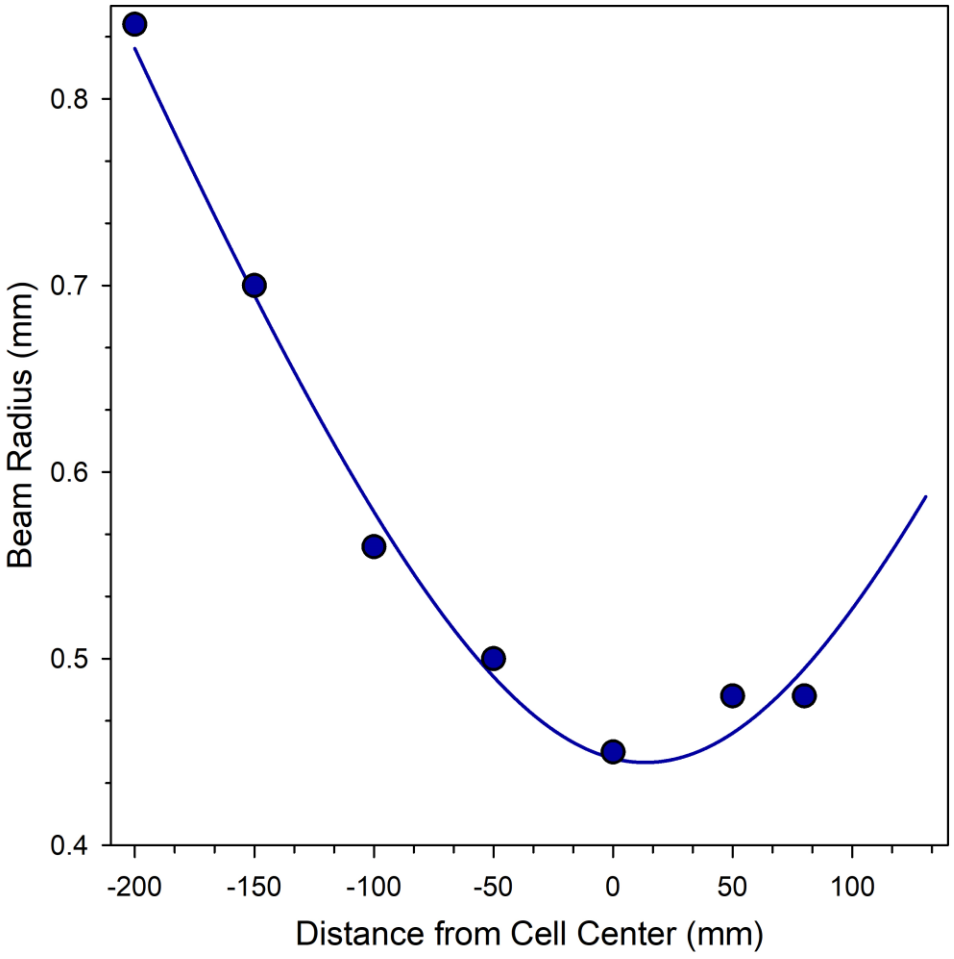

Figure 3.10. Beam propagation fit in absorption cell after adjusting telescope to focus into the center of the cell. New waist was determined as 0.444 mm and z_0 = 135.969 mm.

3.2.5. Spectral Analysis

This section will describe how the degree of pressure broadening was determined from the collected spectra. By using least-squares interpolation fitting to a functional model representative of the peak line shape. Before measuring the pressure broadening of the Lamb-dip under saturated one-photon spectroscopic conditions, the pressure is sufficiently low that the dominant peak is Doppler-broadened and therefore can be accurately represented by a Gaussian function. The Lamb-dip, however, is Doppler-free and is dominated by pressure broadening and therefore can be treated as a Lorentzian function. The lamb-dip and the Doppler-broadened peak can be treated as two separate peaks rather than a convolution of the two (a Voight profile). By fitting to a model which is a combination of a Gaussian and Lorentzian profile each component can be separated out and the fitting parameters for the Lamb-dip can be determined.

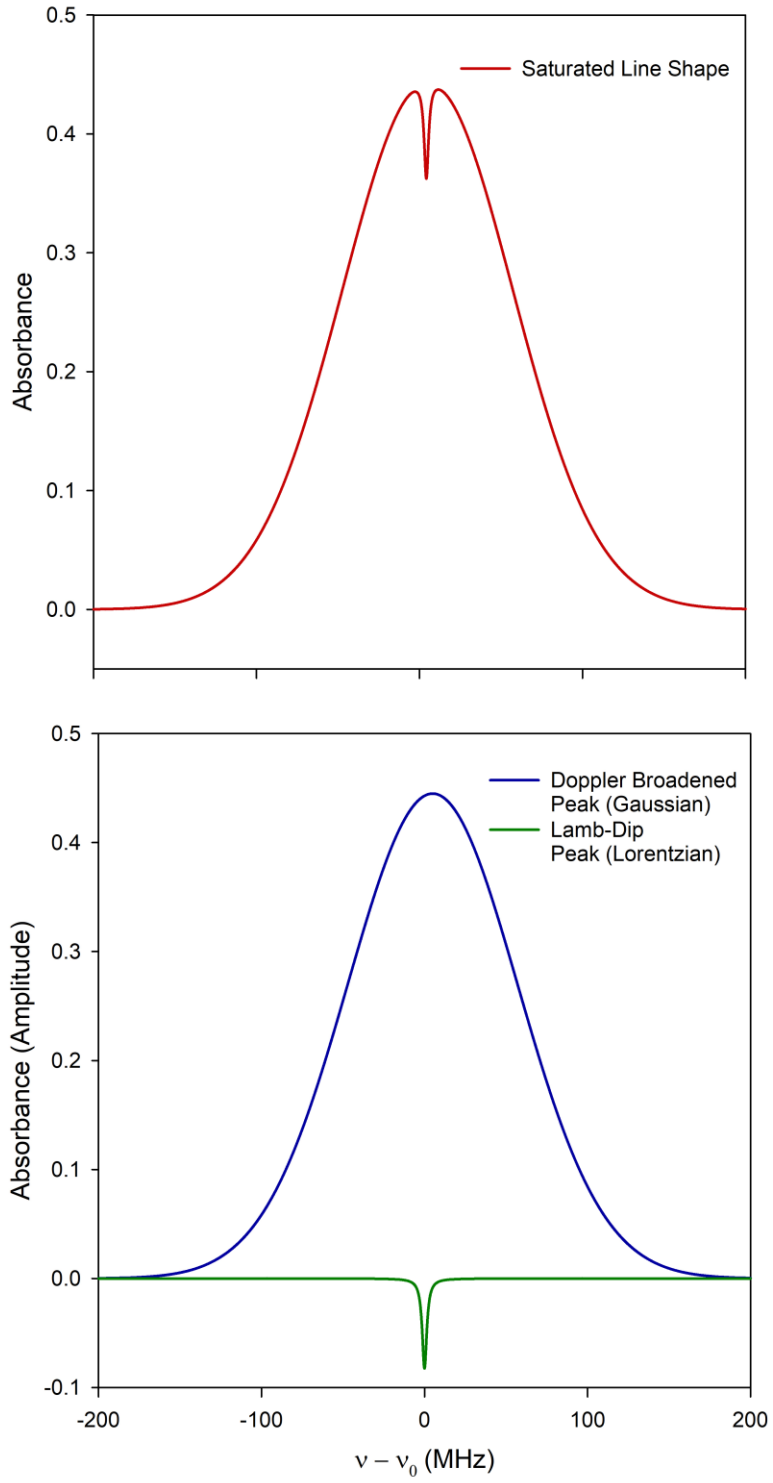

Figure 3.11. Representation of the fit to the saturated absorption line shape and breaking it down into Gaussian and Lorentzian components.

When the laser is being frequency modulated (FM) the same principles can be applied however the fitting function differs. The resulting line shape is affected by the modulation due to the differential absorption at the side band frequencies. The Doppler-broadened peak can be described as the derivative of the Gaussian function. Similarly, when the backwards propagation is not blocked the Lamb-dip can be represented as the derivative of the Lorentzian function.

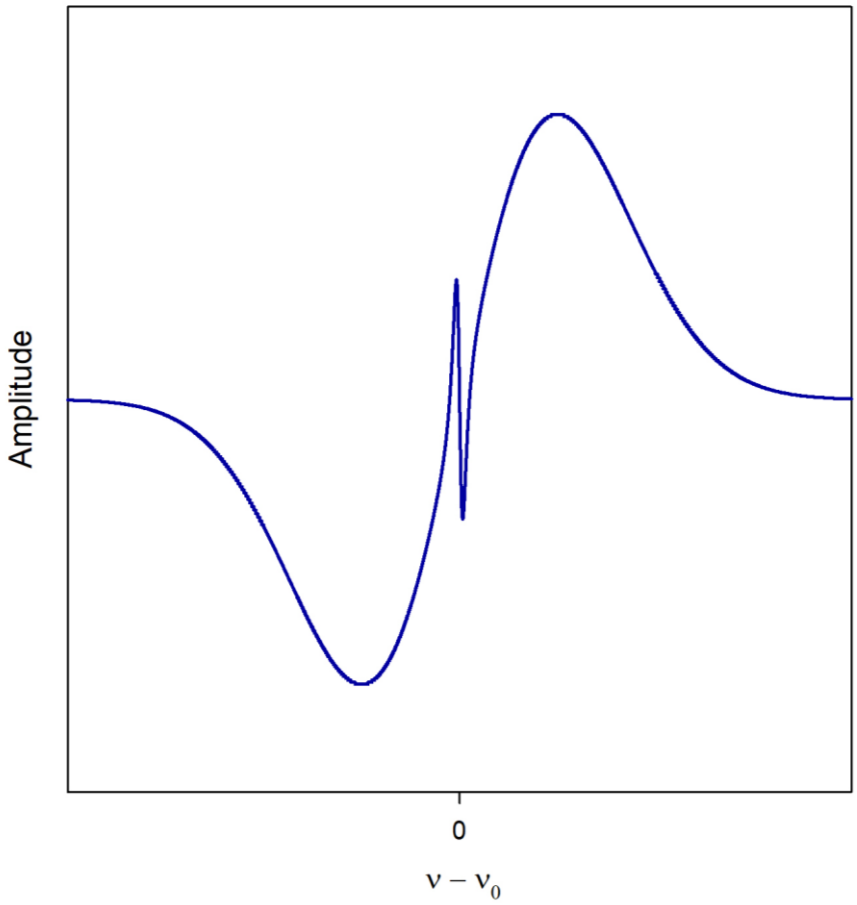

Figure 3.12. Generated line shape depicting the frequency modulated absorption of a Gaussian derivative with an added Lorentzian derivative at the central frequency ν_0. If the back reflection is blocked the Lorentzian component will not be visible.

Finally, the two-photon absorption is expected to have a simple Lorentzian line shape. As discussed earlier, one color two-photon absorption from counter propagating waves in inherently

Doppler-free due to first order Doppler shifts canceling out (see Figure 3.3). This results in pressure or collisions as the primary dominant contribution. Pressure broadening is a type of Homogeneous broadening and typically represented as a Lorentzian function.

3.3. Results and Discussion

3.3.1. Doppler-Free Pressure Broadening Coefficients of P(18) Transition of N_2O

To find the pressure broadening coefficients of the Doppler-free Lamb-dip of the P(18) transition of N_2O the desire was to find coefficients for the self-broadening as well as broadening caused by prominent atmospheric gasses. Starting with self-broadening, due to the high transition strength of this transition ($S = 9.072\text{x}10^{-19}$ cm^{-1}/(molecule * cm^{-2})) only small amounts of N_2O could be used before the absorbance would saturate the detector.[27] Therefore, while measuring the broadening, the starting pressure was limited typically to only a few millitorr. In Figure 3.13 **(a)** is a spectrum of N_2O taken at 5 mTorr. By using a least-squares interpolation fit to a Gaussian function of the form

$$f(x: A, \mu, \sigma) = \frac{A}{\sigma\sqrt{2\pi}} e^{-(x-\mu)^2/2\sigma^2}$$

Added with the Lorentzian form

$$f(x: A, \mu, \gamma) = \frac{A}{\pi}\left[\frac{\gamma}{(x-\mu)^2 + \gamma^2}\right]$$

The amplitude and width of the Lamb-dip could be determined. The specific Gaussian and Lorentzian forms used here are from the same python curve-fitting module mentioned in Chapter 2.[23] In both functions A represents the amplitude and area of the peak, μ is the peak center. In the Gaussian function σ is the standard deviation which is related to the FWHM as

$$FWHM_G = \sigma * 2\sqrt{2\ln 2}$$

And the Lorentzian function γ is the HWHM or

$$FWHM_L = \gamma * 2.$$

For the Lamb-dip shown in Figure 3.13, the Lamb-dip was measured to have an Amplitude of 0.436 +/- 0.027, a depth of 0.083 +/- 0.004, and a FWHM of 3.369 +/- 0.267 MHz.

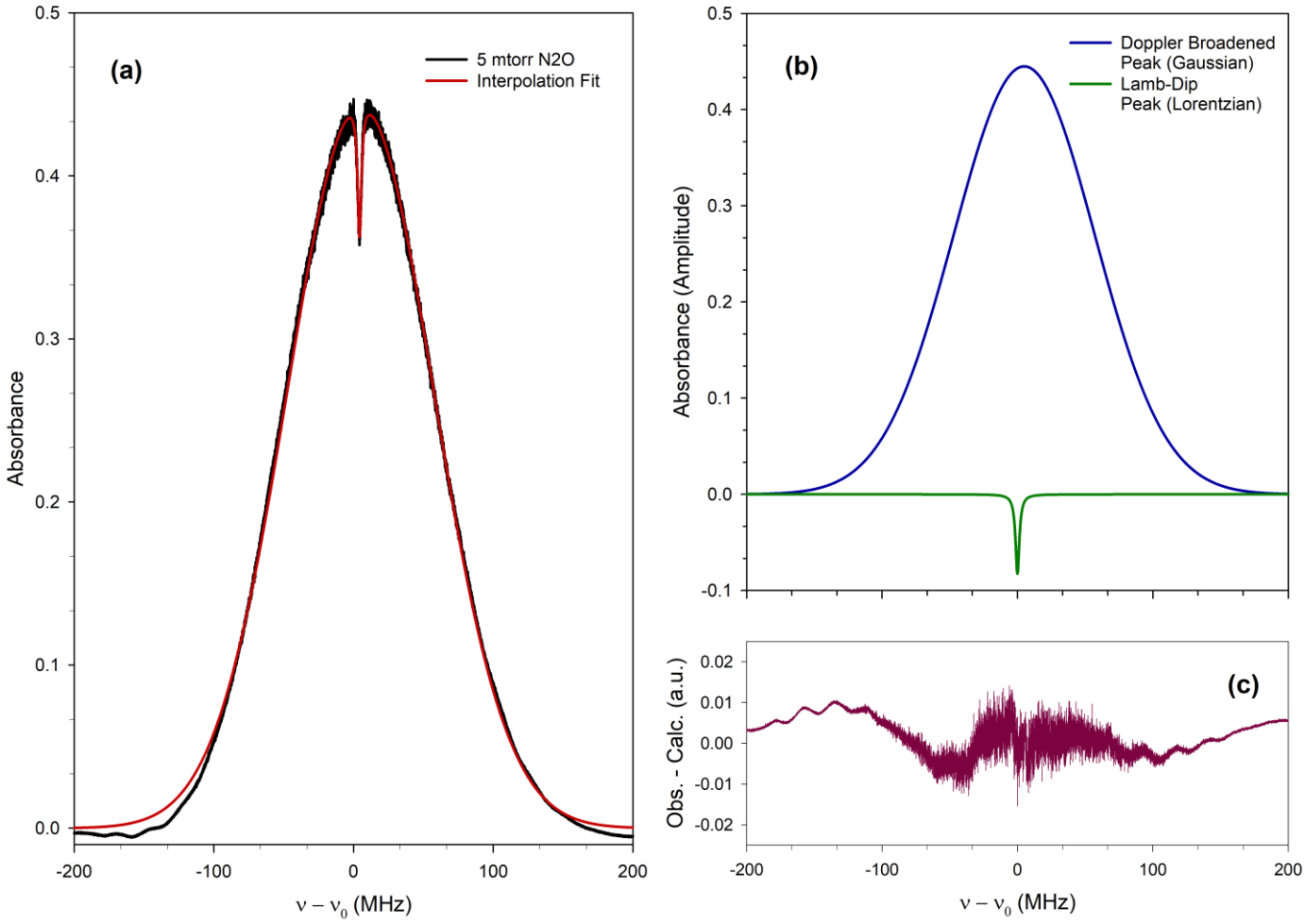

Figure 3.13. Spectrum of 5 mTorr of N_2O. (a) Absorbance spectrum and least-squares interpolation fit. (b) The Gaussian and Lorentzian components which combine to the interpolation fit. (c) Residuals between absorbance spectrum and fit.

Similarly, this process was repeated at increasing pressures of N_2O in the cell. Unfortunately, due to the strong absorbance of the transition, only a few mTorr additional N_2O gas could be added without saturating the detector. See Figure 3.14 for the spectra of increasing N_2O.

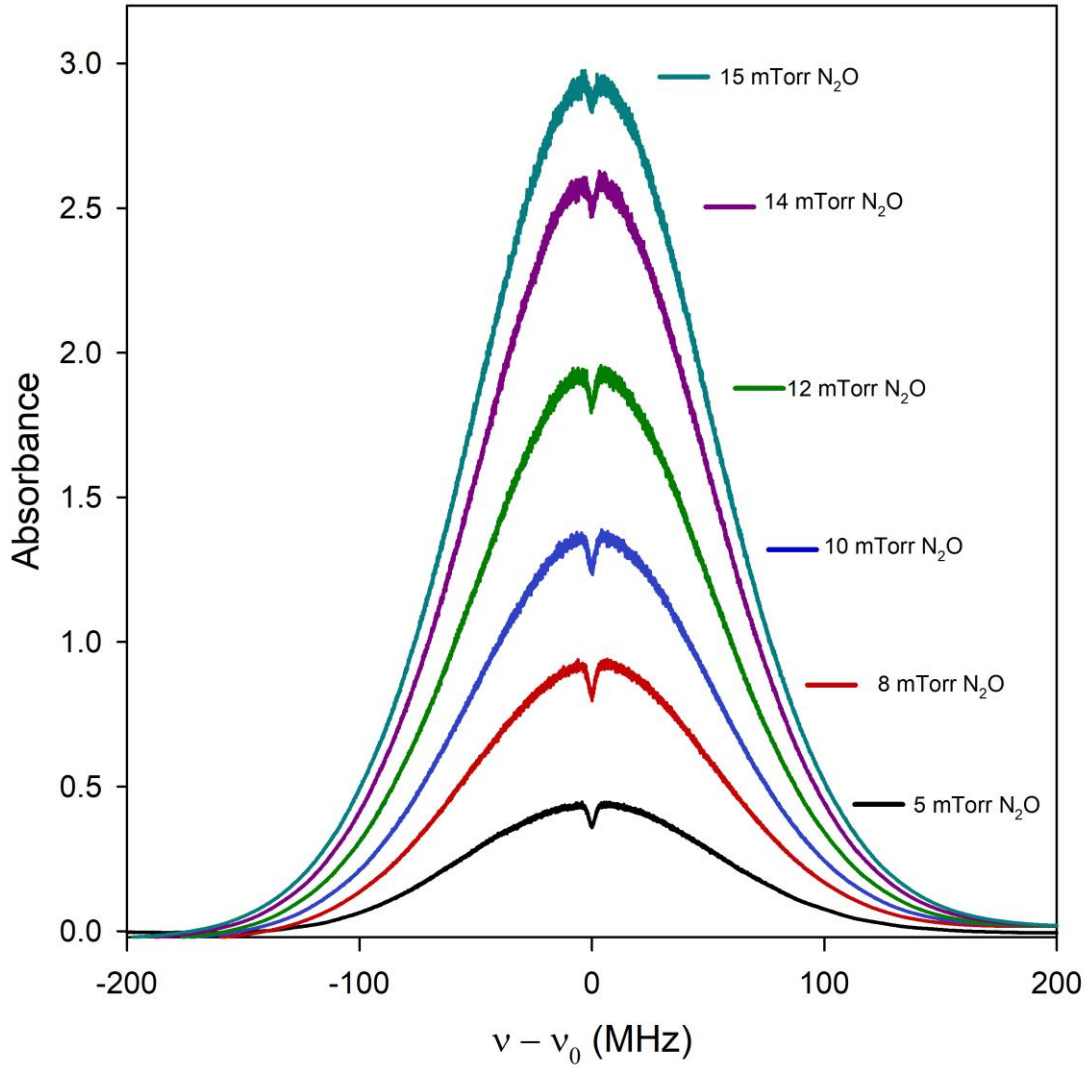

Figure 3.14. Saturated absorption spectra taken at increasing pressures of N_2O starting from 5 mTorr to 15 mTorr. As the pressure was increased the Lamb-dip became smaller and more difficult to measure.

As expected, in Figure 3.14 as the number density of the analyte increases the overall absorbance of the Doppler-broadened peak increases. However, as the pressure increased the Lamb-dip as a whole was decreasing in size. As mentioned above, the amplitude of the Lamb-dip in the 5 mTorr spectrum was 0.436 compared to the Lamb-dip at 15 mTorr is 0.064 +/- 0.008. Each spectrum was also taken with the same laser power of 13 mW at the entrance of the absorption cell.

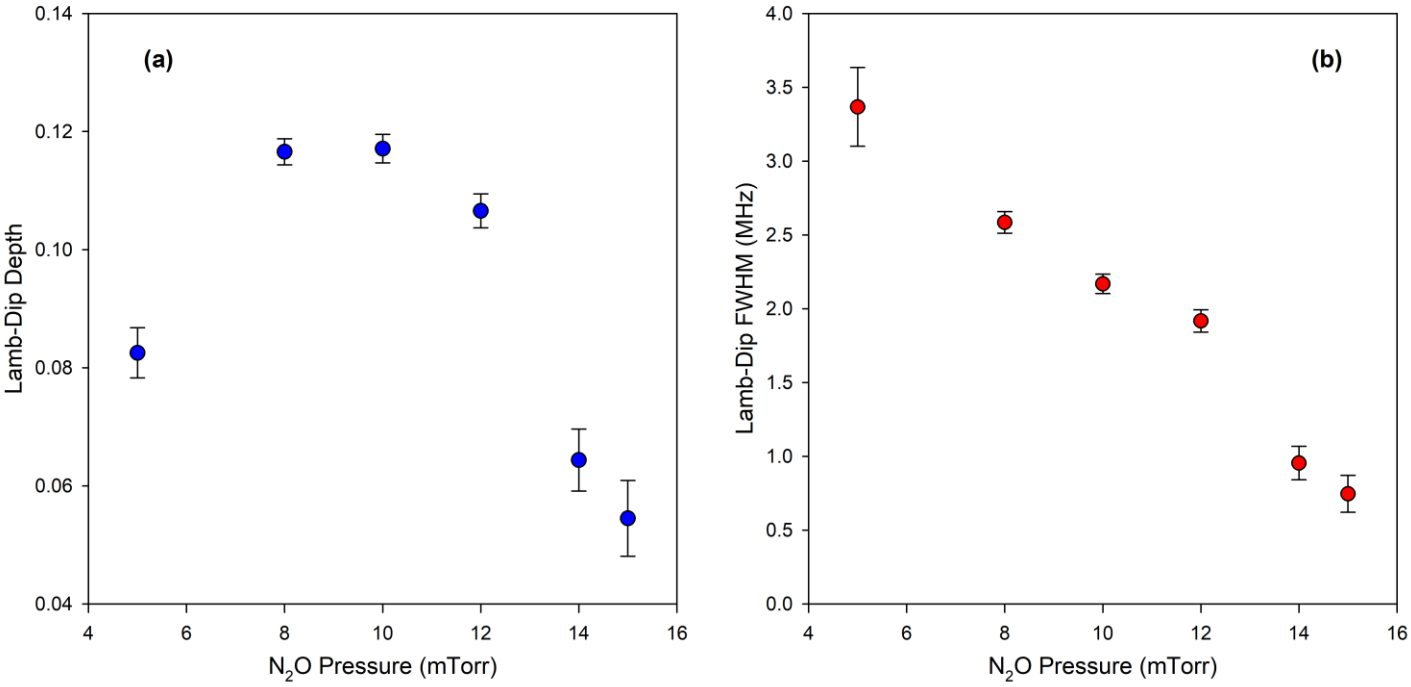

Figure 3.15. Comparison of the Lamb-dip size as N_2O pressure increased in reference to spectra shown in Figure 3.14. **(a)** The depth (height) of the Lamb-dip as pressure increased. **(b)** The FWHM of the Lamb-dip as pressure increased.

Due to the shrinking of the Lamb-dip, it was impossible under the current conditions and methods to accurately measure the broadening as the width was changing with the decreasing amplitude (see Figure 3.15). As discussed in Section 3.1.2 the depth of the Lamb-dip is dependent on the population density of the two levels and thus the saturation level and the homogeneous

width of the Lamb-dip as well. Furthermore, the inability to increase the N_2O pressure high enough where broadening effects would be substantial was another complication. Therefore, the focus turned towards measuring the broadening impact of other atmospheric gasses.

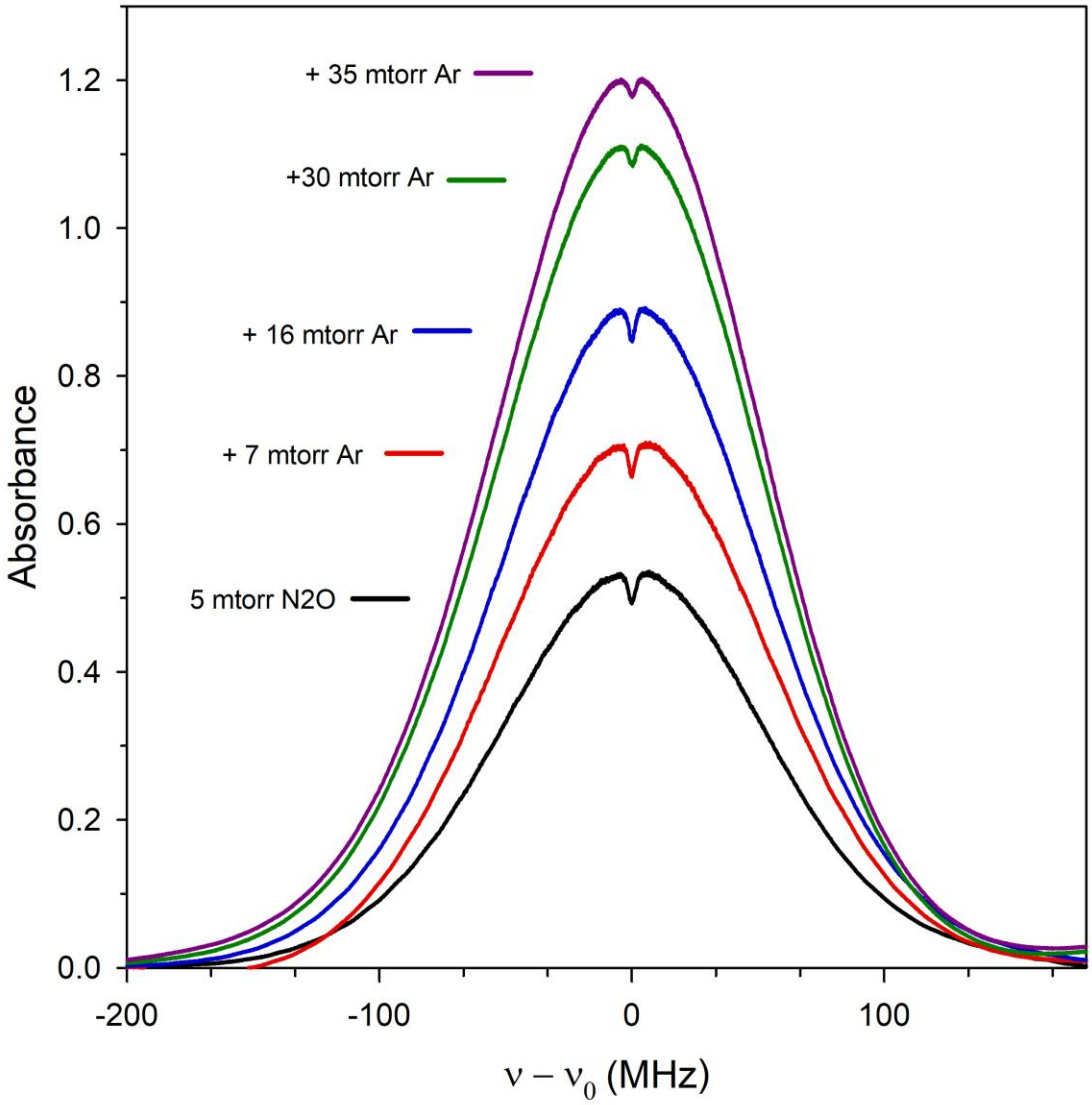

Figure 3.16. Saturated absorption spectra of 5 mTorr of N_2O with increasing amount of added argon gas. Increase in overall absorbance of Doppler broadened peak indicates a reduction in saturation as pressure is increased.

To measure the argon broadening coefficient the same experiment was repeated but with increasing pressure of added argon gas. In Figure 3.16 the spectra of 5 mTorr N_2O added with increasing pressures of argon is shown. It's important to note that as the pressure of argon was increased, the absorbance of the Doppler-broadened peak was increasing. This was not surprising when trying to measure the self-broadening in Figure 3.14 because the amount of the absorber was increasing. However, here it's unexpected due to the number density of N_2O remaining constant in each spectrum. Referring back to Figure 3.6, when unsaturated spectra of 5 mTorr of N_2O were generated at increasing background pressure, the Doppler-broadened peaks all possessed the same absorbance and only the width changes as the pressure broadening becomes comparable to the Doppler width. Here in Figure 3.16 the absorbance is increasing as the pressure is increasing. This suggests that the saturation parameter is decreasing with increasing pressure. If the degree of saturation is changing it would explain why the Lamb-dip is becoming so small at higher pressures and difficult to measure and also result in inconsistent widths.

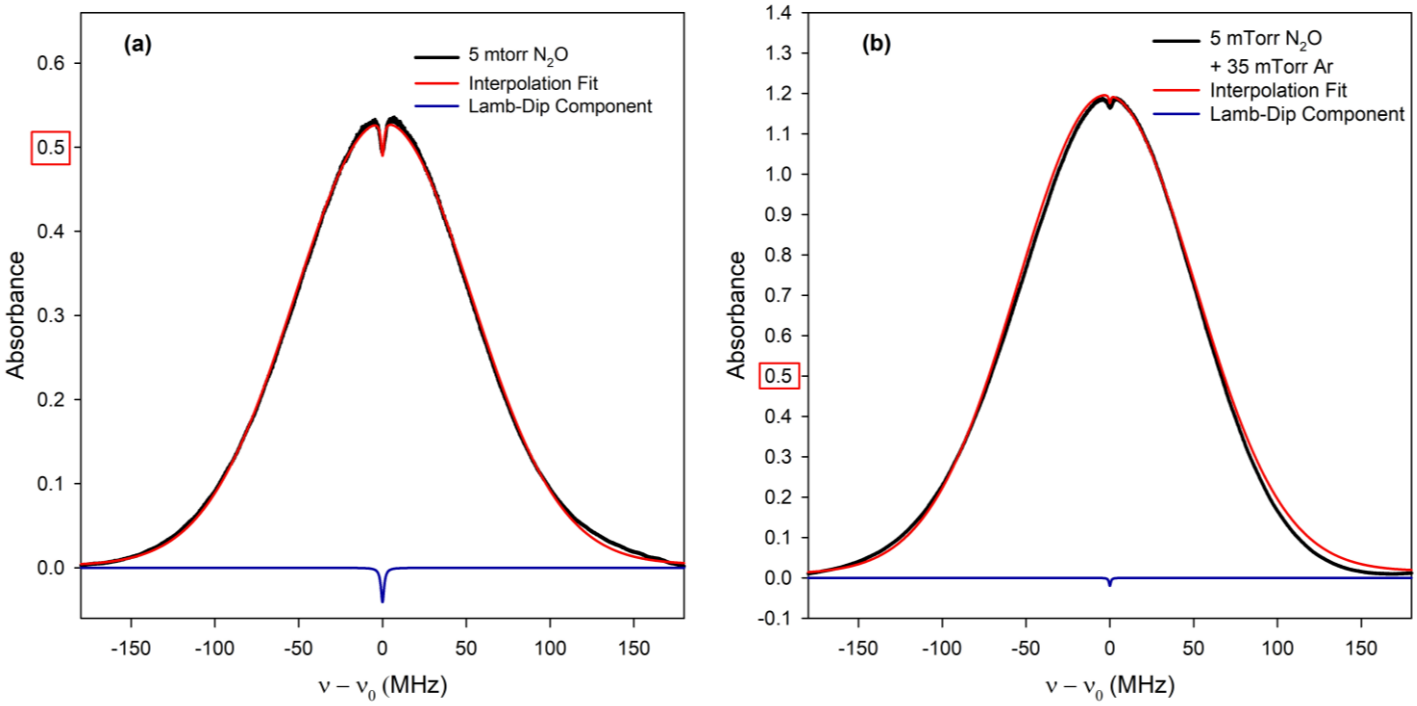

Figure 3.17. Side-by-side comparison of the **(a)** 5 mTorr N_2O absorbance spectrum to **(b)** 5 mTorr N_2O with 35 mTorr argon spectrum showing the overall absorbance increasing by more than a factor of 2 as well as the depth of the Lamb-dip, indicating the loss of saturation.

To understand how the Lamb-dip amplitude is changing with pressure see Figure 3.18. The Depth (absolute height) is compared to the Doppler-broadened absorbance. Due to the constant amount of N_2O, if saturation were constant, the absorbance would remain constant. Therefore, the peak absorbance indicates the degree of saturation. While the absorbance increases, the saturation **decreases** and approaches the linear regime.

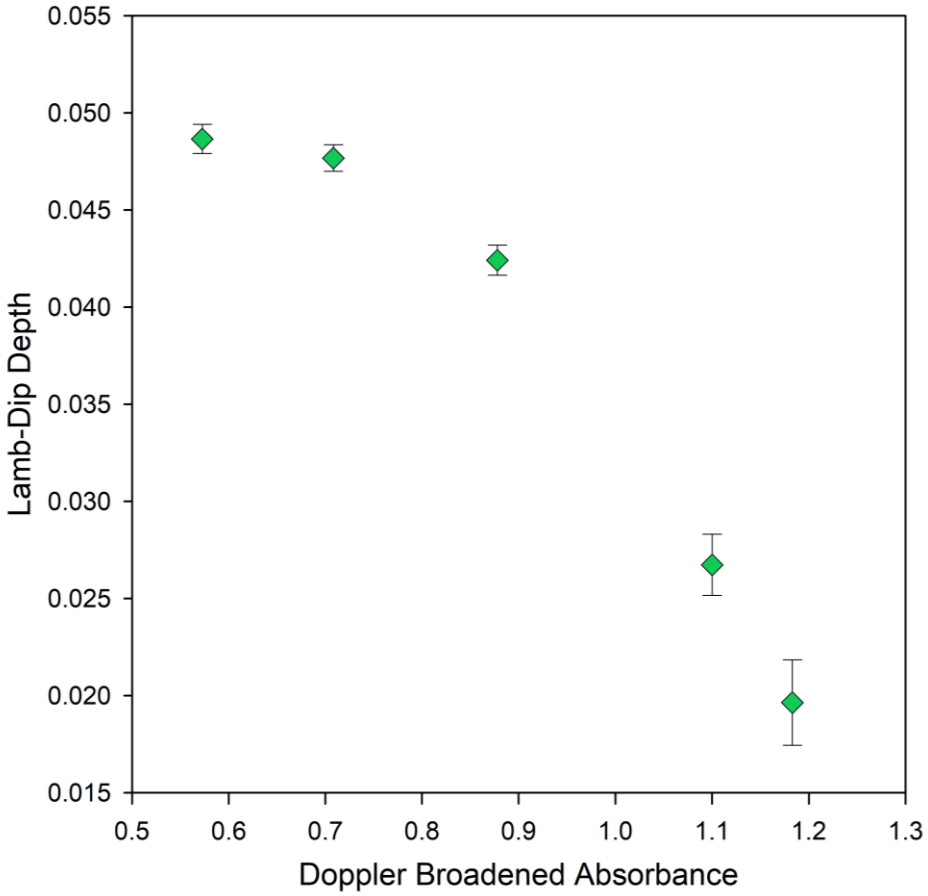

Figure 3.18. A comparison of Lamb-dip amplitude as the Doppler-broadened absorbance increases. Values used are based on fitted values from spectra in Figure 3.16 which were taken under the same conditions. As the Doppler-Broadened absorbance increases while N_2O population remains the same, the saturation parameter must be decreasing.

As seen in Figure 3.18, the Lamb-dip depth is decreasing as the saturation is decreasing and pressure is increasing. This is consistent as the relaxation rate would increase with increasing pressure. It would be possible theoretically to increase the laser power while increasing the pressure to try and maintain the saturation, however this is difficult to do in real-time while collecting spectra and several of the spectra shown were taken at full power.

Currently, work is being done to correct for the loss of the saturation. As mentioned previously the absorbance of the Doppler-broadened peak can indicate the degree of saturation. To actually convert one to the other is much more complicated. The power of the beam inside the cell can be calculated as it propagates through the cell (dP/dz) using the beam size parameters described in Section 3.2.4. There's an additional factor to include which accounts for how the beam intensity is lost during propagation due to absorption. The effect of optical pumping on the saturation of population densities of a two-level nondegenerate system can be described by

$$\frac{dN_{\mathrm{i}}}{dt} = -\frac{dN_{\mathrm{k}}}{dt} = -B_{\mathrm{ik}}(\omega)\rho(\omega)N_{\mathrm{i}} - R_{\mathrm{i}}N_{\mathrm{i}} + B_{\mathrm{ik}}(\omega)\rho(\omega)N_{\mathrm{k}} + R_{\mathrm{k}}N_{\mathrm{k}}$$

Where N_i is the population density, R_i is the relaxation rate for state i, $B_{ik}\rho(\omega)$ is the probability for the transition $|i\rangle \rightarrow |k\rangle$.[31] The relaxation rate will be dependent on pressure and the collisional relaxation cross-sections for N_2O – N_2O and N_2O – Ar. Once the saturation can be determined, the Lamb-dip size/shape can be corrected for and hopefully pressure broadening coefficients can be extracted.

3.3.2. Impact of Frequency Modulation Depth and Saturation on Line-Shape

The results discussed in the following section are preliminary results. Here while frequency modulating the QC laser and saturating the transition an SRS lock-in-amplifier is used to capture the demodulated spectrum. The goal was to see the impacts of N_2O pressure, saturation, modulation depth, and modulation frequency had on the demodulated line shape. Initially to see if there were any observable trends in preliminary data the peak-to-peak amplitude of the demodulated spectrum was compared as modulation depth was increased. Figure 3.19 shows the increasing amplitude of the demodulated height with increasing modulation depth. This was done for three different laser powers in the absorption cell, two well saturated and one on the cusp of

saturation/unsaturated. All spectra represented in Figure 3.19 are taken with 1 mTorr N_2O, modulating at 50 kHz sine wave with a 10 ms time constant. The amplitudes shown have been corrected for the lock-in-amplifiers sensitivity scale. More work needs to be done to understand how the actual shape is being affected rather than just the amplitude. Also, other factors such as pressure and modulation frequency are to be considered in the future.

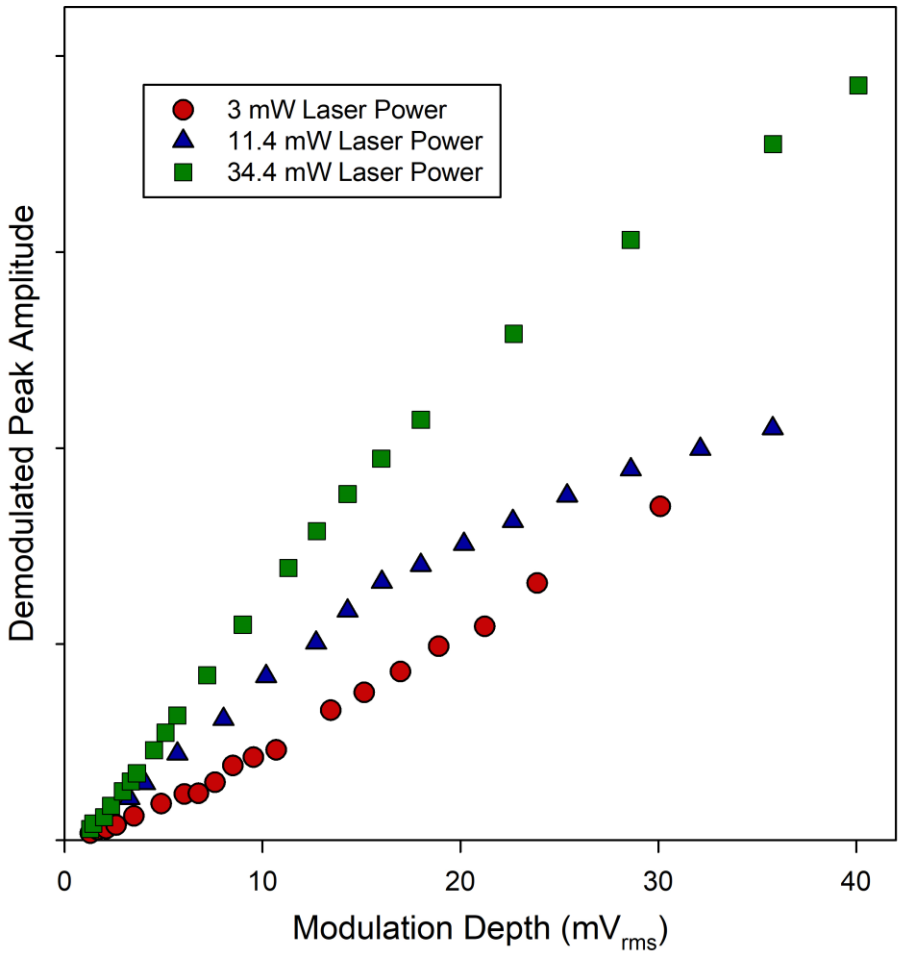

Figure 3.19. The change in amplitude of the demodulated peak while the modulation depth was increased. The amplitude shown is a relative value. Spectra shown, the modulation frequency was 50 kHz sine wave and the lock-in amplifier used to demodulate the spectra had a time constant of 10 msec and 1 mTorr of N_2O.

3.3.3. Doppler-Free Two-Photon Spectroscopy of Q(18) Transition of N_2O

The results discussed in the following section are only preliminary results and little work has been done on this subject to date. It is the hope of the writer that this work continues because of its high potential. As shown in Figure 3.5 the Q(18) transition is shifted due to the nondegeneracy of the R(17) and P(18) transitions. By using the counter propagating waves generated for detection of the Lamb-dip shifted to the Q(18) transition frequency, the two-photon absorption should be detectible. The greatest difficulty here being one of the attractions of two-photon absorption, the narrow line-width. This specific transition is being used because it has been measured previously[34] and the frequency is known to high precision. However, at low pressures (a few mTorr) the expected width would only be a few MHz. The only frequency detector available in the lab in this range had a precision of 0.01 cm^{-1}. Even while locking the laser to fringes of the etalon shown in Figure 3.7 the QCL was still susceptible to drift several MHz/sec. The combination of these conditions made it difficult to ensure that the QCL was even scanning in the correct region. To try and ensure the two-photon absorption would be observed, a broadband spectrum was initially taken to ensure the two-photon transition frequency was covered. This could then be compared to a theoretical spectrum generated from HITRAN which does not include information regarding the two-photon transition. The hope being any peaks present in the spectrum which are not present in the theoretical spectrum would be easily noticeable. Also, this was repeated with the back reflection blocked, which would prevent the two-photon transition from occurring and any differences between the spectra should indicate the desired absorption.

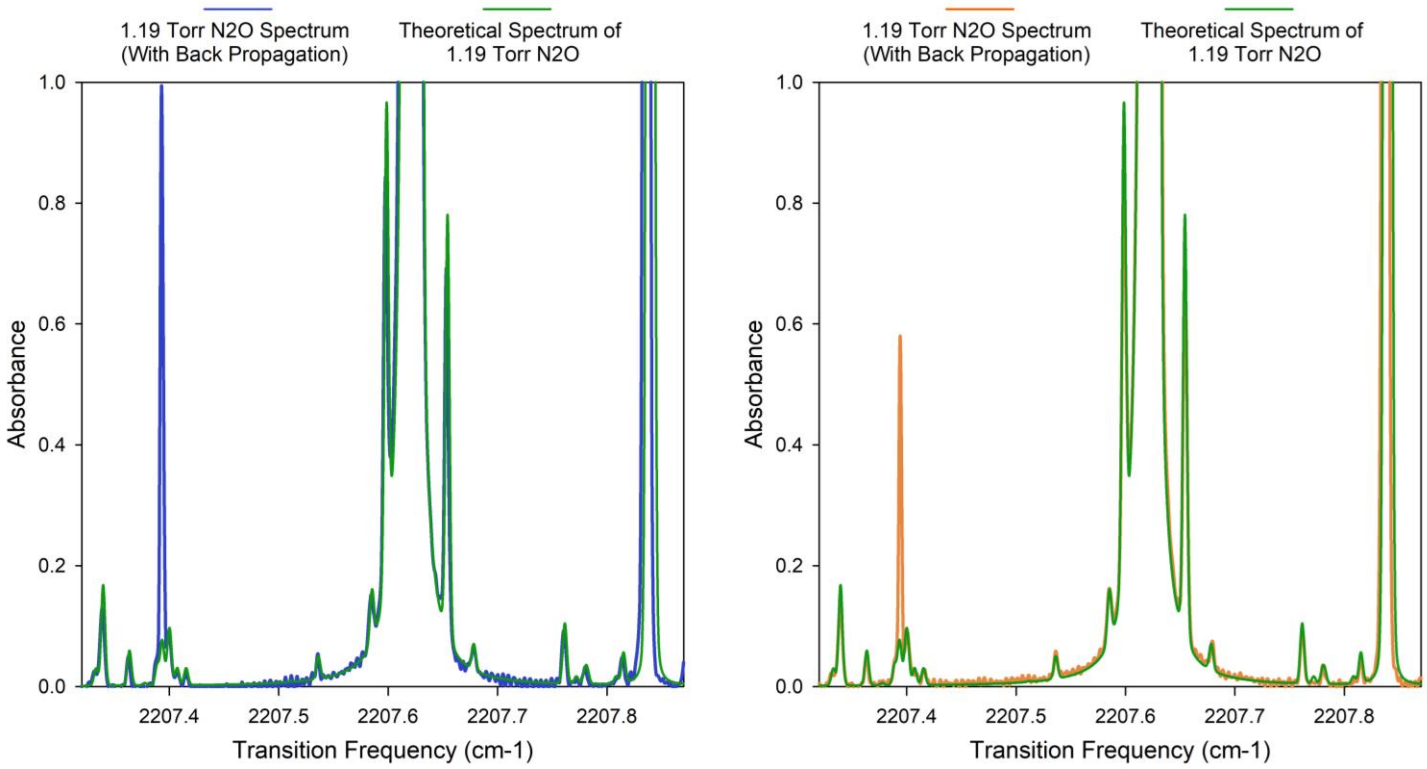

Figure 3.20. Broadband spectrum of N_2O at 1.19 Torr with no added gas scanning over a region encompassing the R(17), P(18) and the Q(18) is expected to be seen. The experimental spectrum is compared to a theoretical spectrum generated from HITRAN database which does not contain two-photon data. Evidence of vibrational heating can be seen around 2207.39 cm^{-1}. The Y-axis is restricted to 1 for clarity of the smaller transitions.[27]

Seen in Figure 3.20 are the 1.19 Torr N_2O spectra and the associated theoretical spectra. The theoretical spectrum is generated the same as described in Section 2.2.5 but each transition listed in HITRAN for this region is assigned a Voight profile based on its frequency, transition strength, and broadening coefficients. There is no peak visible at the expected two-photon frequency (2207.5 cm^{-1}) but interestingly, there is enhancement of the excited state R(17) transition at 2207.39 cm^{-1}. Also, interesting to note that the degree of this enhancement is dependent on the presence of the back reflection wave. It is unclear at this time what is the cause of this enhancement which needs further investigation.

3.4. Conclusion

As shown above N_2O saturated absorption spectra were collected and the Lamb-dip was visible indicating proper alignment of the back reflection. Problems with being able to maintain saturation with increasing pressure has made it difficult to measure the Doppler-free pressure broadening coefficients. Increasing the available laser power is one way to combat this. Work has already been done to improve the optical alignment to maximize the power in the cell. One major cause for a loss of power was the isolator. Although necessary for blocking feedback, it's difficult to find isolators available with high transparency in the mid-IR region. By replacing the isolator with a polarizer and quarter-wave plate, power losses may be reduced. If a solution can be found to correct for the loss of power in real time, this should allow the broadening coefficients to be measured otherwise post collection correction should be possible. The two-photon spectrometer is promising, more work can be done by confirming alignment and using lock-in-amplifiers to "find" the transition.

Chapter 4

Infrared Photodesorption of Molecular Methane from Pt(111) via C-H Stretch Excitation

Contributing Authors: Mark E. Bernard, Kevin K. Lehmann, Ian Harrison

4.1. Introduction

The experiment described in this chapter details the exploration of mode-selective chemistry and dynamics of inter and intra molecular vibrational energy redistribution. Here methane (CH_4) was adsorbed onto a platinum (Pt) single crystal (Pt(111)). Following physisorption, the methane was irradiated with a high-power mono-chromatic light source referred to as an Optical Parametric Oscillator (OPO). The desorption efficiency of methane was measured and compared when the irradiation frequency used was on or off resonance from vibrational modes of methane. From the measured desorption efficiency, an upper-bound effective IR photodesorption cross-section was determined. The work in this chapter is soon to be submitted for review.

4.1.1. Motivation

Currently, models predicting gas-phase and gas-grain processes in pre-stellar cores underestimate the abundances of simple hydrocarbons, such as methane (CH_4), determined via spectral observations.[36-42] IR observations have indicated the presence of carbon or silicate-based dust grains in these dense star-forming regions. It is believed that these dust grains behave as catalysts for interstellar chemistry, whereby atoms and molecules can adsorb noncovalently

(physisorb) on the grain surface, dissociate or form complexes, and desorb contributing to gas-phase species observed in the interstellar medium (ISM).[43, 44] Current rate-based gas-grain models commonly account for thermal, ultra violet (UV), and cosmic ray (CR) based processes to assist in desorption from the dust grain surface. However, in the cold outer envelopes of pre-stellar objects ice grains are well shielded from UV and CR photons, and due to the low temperatures (commonly below 20 K) there is typically not enough thermal radiation to promote thermal desorption.[45, 46] Even in warmer regions with ample UV and CR radiation, current models underestimate the abundance of small organic molecules.[40, 47] For these reasons it is important to consider other pathways which could promote desorption. Here, the ability for resonant IR radiation to promote methane desorption is measured.

Previously, IR photoexcitation has been shown to promote desorption of surface-bound molecules from metal surfaces, thin films, or ice grain analogues.[48-51] Here, a relatively favorable case for IR photodesorption via vibrational energy transfer was explored in some detail.

4.2. Experimental

The following section details the methods and procedures used in this project. In addition, information regarding properties and vibrational transitions of methane are discussed to provide context for discussion of results in future sections.

4.2.1. Properties of Methane

CH_4 is a highly symmetrical molecule with a tetrahedral geometry with the carbon atom surrounded by the four hydrogen atoms with a T_d point group symmetry. The chemical structure can be seen in Figure 4.1 below. The work described in this chapter focuses primarily on the ν_3 antisymmetric vibrational mode and briefly on the ν_1 symmetric mode. These modes were chosen due to their frequency being in the available excitation range of the OPO and one quanta of the transition providing sufficient energy to overcome the desorption barrier (discussed in greater detail in following section).

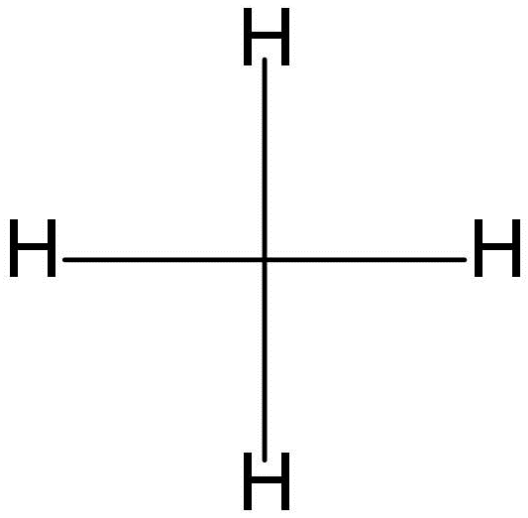

Figure 4.1. Chemical Structure of CH_4.

The vibrational modes of methane and their associated frequencies are described in Table 4.1. Similar to Chapter 3, the number of normal vibrational modes of a molecule can be determined, however, in this case the molecule in nonlinear, resulting in $3N - 6 = 9$ normal vibrational modes. Due to degeneracies, there are only four distinct frequencies. It is important to note that the surface-bound frequencies are red-shifted from their gas-phase counterparts. The change in vibrational frequency is due to frustrations in the methane bonds imposed upon by the surface. As more layers are added to between the surface and adsorbate, the effect of the surface weakens, and the vibrational frequencies move back towards their gas-phase values.

Gas-Phase Modes (cm^{-1})	Bulk CH_4 Modes (cm^{-1})	CH_4/Pt(111) Modes (cm^{-1})	Vibrational Mode
2917	2905	2883	Symmetric Stretch (ν_1)
1534	1538	-	Symmetric Bend (ν_2)
3019	3010.9	2997	Antisymmetric Stretch (ν_3)
-	-	3016	Overlayer Antisymmetric Stretch (ν_3^M)
1306	1304.8	1297	Antisymmetric Bend (ν_4)

Table 4.1. Description of Methane Vibrational Modes: gas-phase and surface bound frequencies included.[52-55]

4.2.2. System Energetics

A major goal of this project is to better understand the transfer of energy through the system from vibrational excitation to desorption or dissipation via other channels. As such it is important to discuss the possible energetic pathways available and their possible impact on desorption efficiency. Below in Figure 4.2 is a modified diagram provided by Chuang[56] and Gortel and Teshima[57, 58] depicting various IR photodesorption pathways. While a molecule is adsorbed to a

metal surface there is an energy barrier (E_d) which is necessary to overcome for desorption to occur. Therefore, if a bound molecule were to absorb a single photon which is on resonance with an internal vibrational transition of energy greater than the desorption energy then desorption from the surface may be induced, returning the molecule to the gas-phase. For this to successfully occur, the internal vibrational energy of the molecule must be transferred to energy levels in the adsorbate-surface potential to promote desorption. This process is facilitated via bound-state – bound-state transitions with the probability $P_{i'i}^{v'v}$ (where v and v' represent the available internal vibrational levels and i and i' represent the adsorbate-surface bound states).[57, 58]

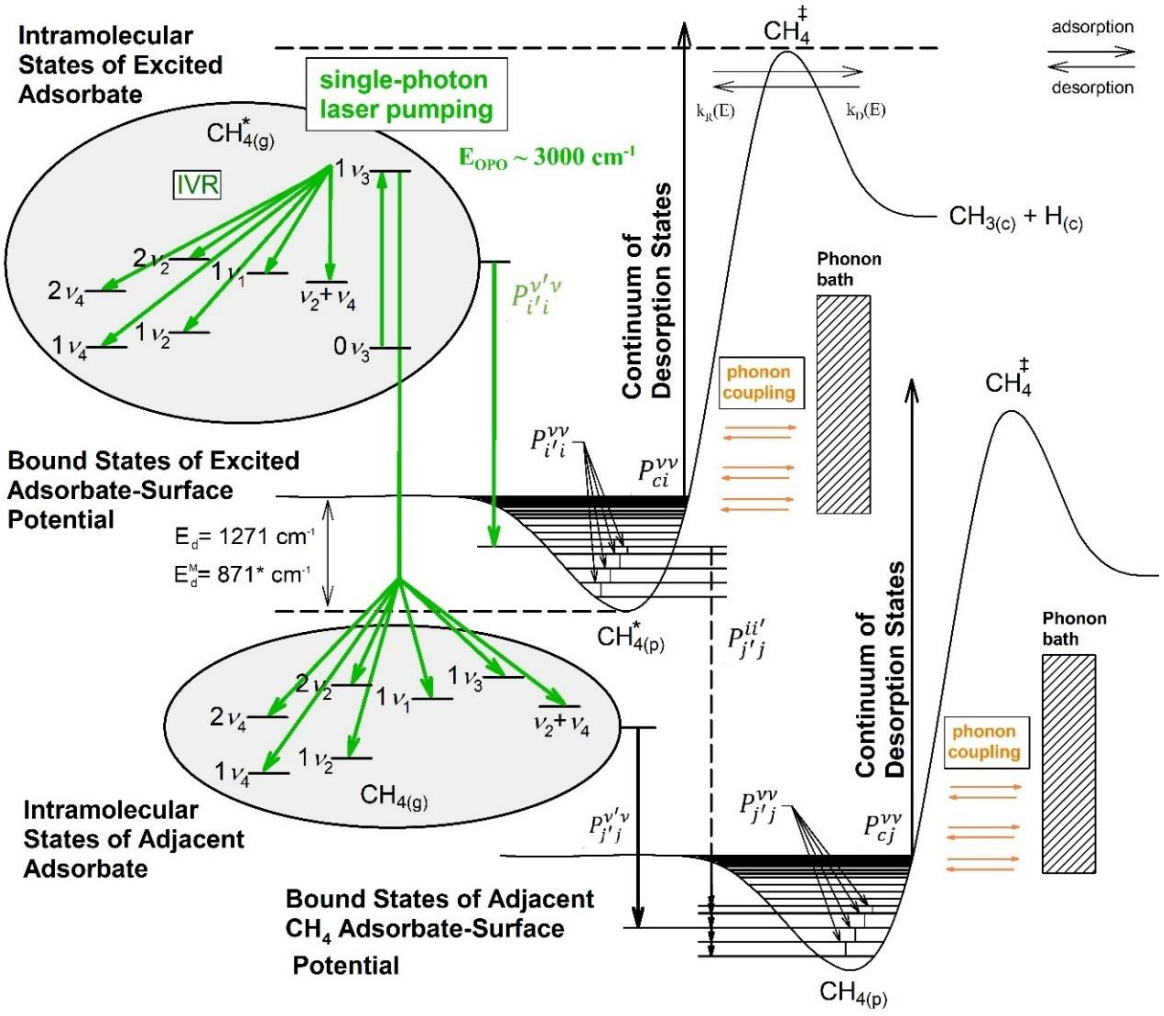

Figure 4.2. Diagram representation depicting various vibrational energy dissipation pathways for physiosorbed on Pt(111).

Due to the shifted surface-bound vibrational frequencies from their gas-phase counterparts (Table 4.1), it is expected that methane adsorbed on platinum has some degree of surface coupling whereby internal vibration excitation can be transferred to the adsorbate-surface potential which could promote desorption. However, the internal vibrational energy can similarly be transferred elsewhere in the system, leading to relaxation and no desorption. The surface substrate itself possesses a wide range of low-energy vibrational modes referred to as the phonon bath. Due to the

high density of states and low frequency of these modes increases the probability of coupling. This can induce a phonon cascade with successive downward transitions generating more phonons. The cascade of phonons can result in indirect localized heating (resonant heating) which can also aid in desorption thermally if the temperature approaches the desorption temperature.[59] Similarly, the substrate can also engage in direct photon absorption and as a result heating (substrate heating) and contribute to thermal desorption.

In addition to relaxation via adsorbate-surface energy transfer, vibrational energy can be transferred to other vibrational modes in neighboring methane molecules. Energy transfer between vibrational modes (V-V) is more or less efficient depending on transition frequency coupling. The stretching modes of methane are around 3000 cm^{-1} compared to the bending modes around 1400 cm^{-1}. V-V transfer has been observed in the gas-phase between the stretching modes and bending overtones resulting in relaxation on the order of microseconds with V-V transfer rates around $3x10^{-12}$ to $3x10^{-11}$ cm^3 $molecule^{-1}$ S^{-1} at 294 K. Similarly, vibration to rotational energy transfers have also been observed in the gas-phase, indicating rotation can also contribute to relaxation. Following energy transfer from one methane to another, energy can be further transferred again either to the substrate or to other neighboring methane molecules, leading to a vast array of relaxation pathways. The efficiency of IR photodesorption depends on the competitive rates, efficiencies and probabilities of the pathways for promotion of desorption and vibrational energy dissipation.

4.2.3. Determination of Methane Adsorption and Desorption

In order for the efficiency of methane to be measured a method must be established to determine the degree of methane coverage on the Pt(111) surface. The primary method used to

determine the adsorbed material on the Pt(111) surface was a form of Fourier-transform infrared spectroscopy modified for surface detection referred to as reflection absorption infrared spectroscopy (RAIRS). Figure 4.3 depicts a RAIRS spectrum of both the ν_1 and ν_3 vibrational transitions of methane on the Pt(111) crystal surface. From this spectrum the FWHM of each peak was measured. Methane was dosed on the surface to saturation of the monolayer which corresponds to a coverage of $\theta_S = 0.33$ monolayers of platinum and 1.5 x 10^{15} methane molecules cm^{-2}.

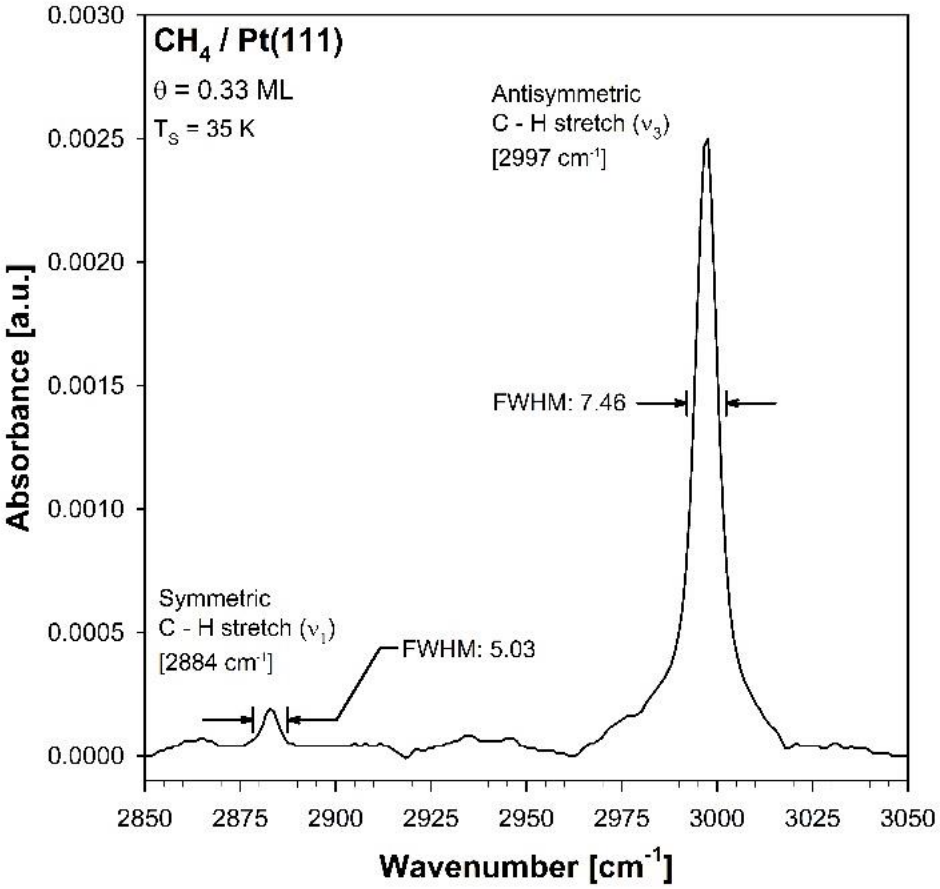

Figure 4.3. RAIRS spectrum depicting detection and characterization of physiosorbed methane $CH_{4(p)}$ on Pt(111). The symmetric and antisymmetric modes and their respective absorption FWHM's are highlighted. The spectrum was collected at a surface temperature $T_s = 35\,K$ and saturation of the monolayer, equivalent to 0.33 platinum monolayers.

Due to the distinct peak frequencies and desorption temperatures between the monolayer and the multilayer and the known coverage density of the monolayer a calibration of the RAIRS spectral intensity can be made to determine the coverage of the surface. As methane is continuously dosed beyond the monolayer, the interaction between the surface and adsorbate is weakened resulting in the different absorption peaks. In addition, the multilayer also has a lower desorption energy compared to the monolayer and similarly lower desorption temperature than that for exactly one monolayer adsorbed to the surface. Although the spectral intensity of the RAIRS peaks increases with increasing coverage, it's not necessarily associated directly with the coverage. However, by combining thermally programmed desorption (TPD) techniques and RAIRS intensity, a correlation with coverage can be determined. The absolute methane coverage can be determined by integration under a TPD spectrum. Therefore, by comparing the coverage of the monolayer desorption to various methane coverages, the RAIRS spectral intensity can be calibrated to associate it with an absolute coverage. The evolution of methane coverage and associated RAIRS spectra can be seen in Figure 4.4.

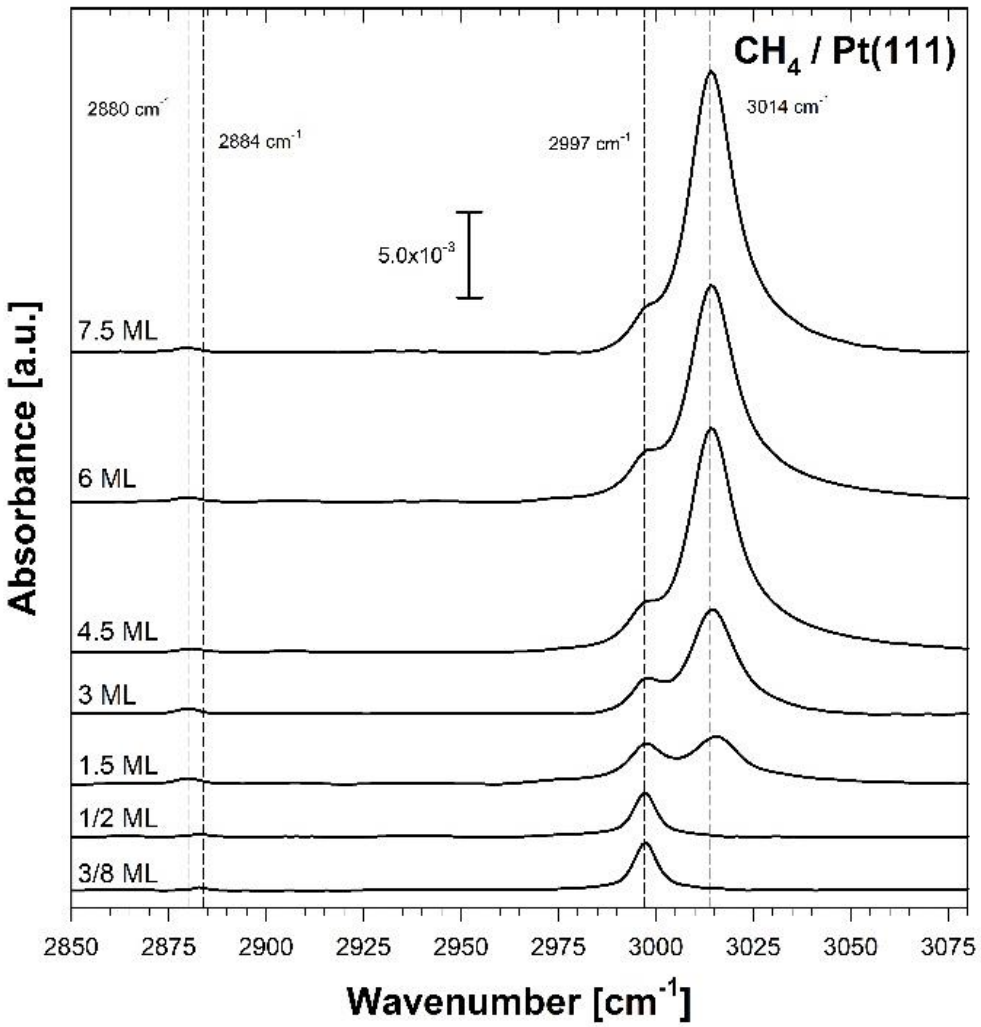

Figure 4.4. RAIRS absorption spectra and associated methane coverage. As coverage increases beyond saturation of the monolayer, the multilayer peak forms.

4.2.4. Experimental Design

The work described in this chapter was conducted in an ultra-high vacuum chamber with an operating pressure less than $2x10^{-11}$ Torr. The platinum single crystal sample is mounted inside the chamber on a copper (Cu) mount. The crystal temperature can be varied from 35 to 1200 K via either cooling from a Gifford-McMahon helium refrigerator or heated radiatively by applying voltage across a tungsten filament located behind the crystal and the temperature was monitored

via a chromel-alumel *K*-type thermocouple spot-welded to the crystal edge. In addition to RAIRS and TPD mentioned earlier the chamber is also equipped with several other surface sensitive detection techniques such as low energy electron diffraction (LEED), Auger electron spectroscopy (AES), X-ray photoelectron spectroscopy (XPS), and time-of-flight (TOF) mass spectroscopy. The chamber also supports ion sputtering which can aid in cleaning the surface prior to adsorption.

Vibrational excitation was achieved using a Lockheed Martin Acculight Argos 2400-SF tunable, single-mode, continuous-wave (CW) optical parametric oscillator (OPO). The OPO idler beam is tunable over a range of 3.2 to 3.9 microns and capable of exciting either the ν_1 or ν_3 vibrational modes. The frequency of the idler beam was monitored using a Burleigh Wavemeter (accurate to within 0.01 cm^{-1}) and has a linewidth less than 1 MHz). The excitation beam was aligned to be *p*-polarized with respect to the Pt(111) crystal to be in accordance with surface selection rules and allow absorption of the OPO beam. The idler beam entered the chamber through a calcium fluoride (CaF_2) window and incident on the crystal surface at 50° creating an elliptical irradiation area on the surface. The beam spot size was measured using the same method described in Chapter 3 to give the resulting Gaussian diameter at the surface as 4.13 mm and the elliptical area of the beam on the surface to be 83.34 mm^2. The OPO beam and FTIR beams were aligned to be centered on top of one another with the FTIR beam accounting for a larger total area of surface coverage. A diagram depicting the optical alignment in combination with the UHV chamber is shown in Figure 4.5.

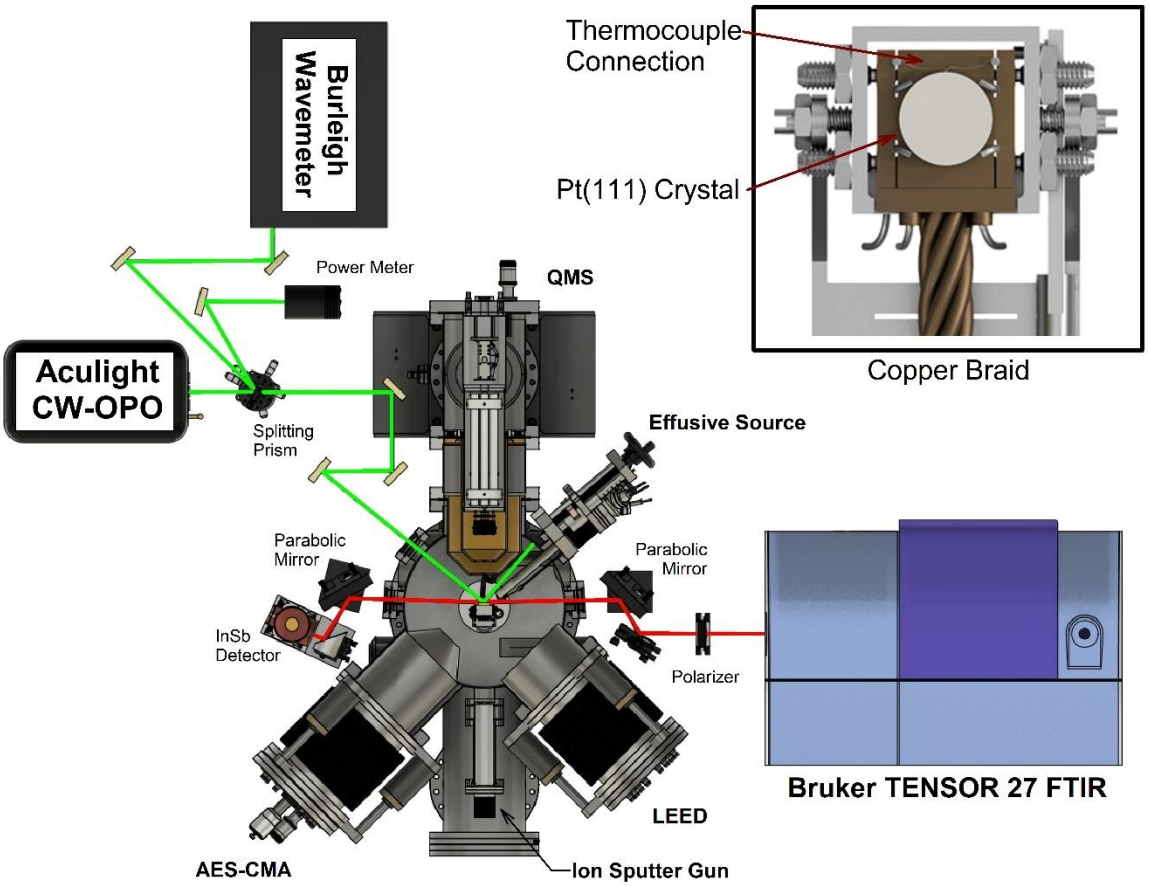

Figure 4.5. Experimental apparatus. Diagram includes ultra-high vacuum (UHV) chamber with…

Prior to adsorption of methane on the crystal sample, the surface was cleaned using a combination of Ar^+ and O_2 thermal desorption at 800 K, followed by thermal annealing to 1200 K. Auger electron spectroscopy was employed to survey surface contamination. Once the surface was determined to be clean, methane was dosed ambiently onto the surface at temperatures of 35 – 45 K based on exposure time (measured in Langmuirs) and TPD spectra described in Section 4.2.3. For more details regarding the experimental design, refer to PhD thesis presented by Mark E. Bernard.

4.3. Results and Discussion

4.3.1. Monolayer Desorption

The methane monolayer on Pt(111) was filled to saturation and irradiated with the OPO idler beam at frequencies on resonance with either the symmetric or antisymmetric stretch of the physiosorbed methane. RAIRS spectra were collected of the surface both pre and post excitation to measure any change in methane coverage. Following excitation, no appreciable change in RAIRS peak intensity could be determined for either vibrational mode regardless of photon flux up to 1.5 W of excitation power. The associated RAIRS spectra are shown in Figure 4.6. The same process was repeated off-resonance from the vibrational modes and resulted in the same outcome. Measurements were also taken using TOF mass spectrometry by chopping the OPO beam as a trigger, and no increase in ion flux was detected, regardless of mass.

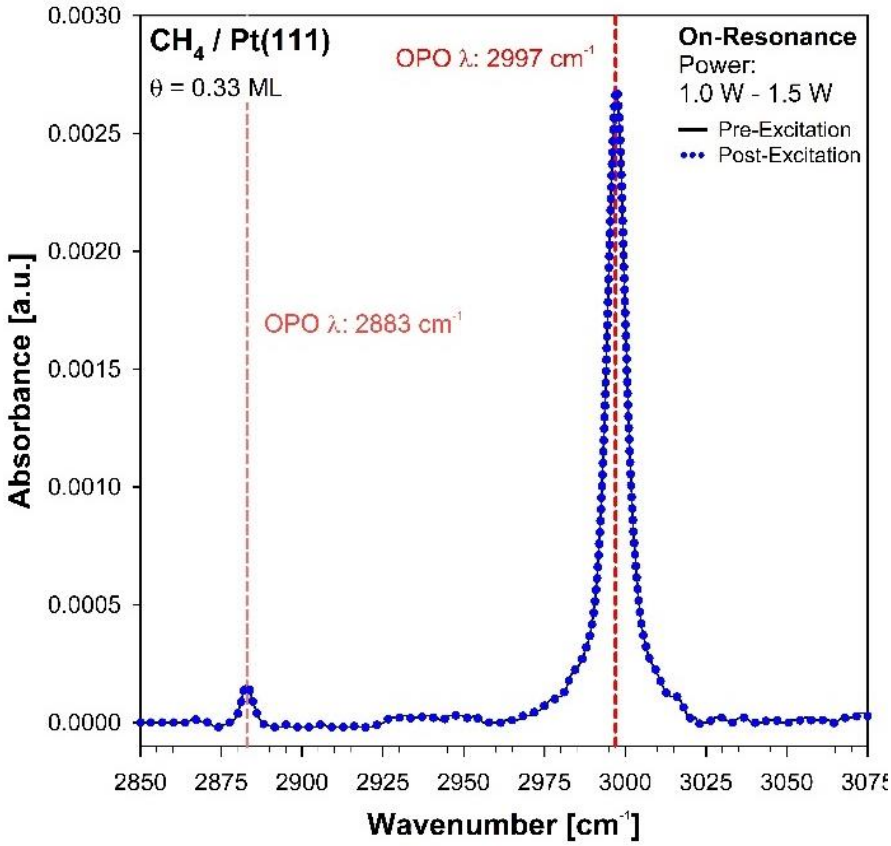

Figure 4.6. RAIRS spectra of methane coverage pre and post irradiation with OPO of the symmetric and antisymmetric vibrational modes. Little to no desorption of the monolayers was observed.

This indicates that despite the energy of desorption of the monolayer being significantly lower than the energy of one quanta of symmetric or antisymmetric stretch (E_d = 1271 cm^{-1}, ν_1 = 2884 cm^{-1} and ν_3 = 2997 cm^{-1}) vibrational excitation was insufficient to promote desorption while surface temperature remains less than the desorption temperature ($T_s \leq 60$ K, $T_d = 77$ K). In order for IR photodesorption to occur, the lifetime of the excited state must exceed the timescale required for desorption. If the excited state relaxes prior to desorption, the energy is dissipated elsewhere in the system and cannot contribute to photodesorption. Dissipation via phonon excitation typically occurs on the order of 10^{-12} seconds, leading this to be a highly competitive rate.[60] However, the

rate of phonon-mediated energy dissipation is dependent on the ratio of the vibrational excitation frequency and the Debye frequency of the substrate (ω_D). If the Debye frequency of the Pt(111) surface can be assumed as equivalent to that of bulk platinum (240 cm^{-1}) then relaxation of one quanta of symmetric or asymmetric stretch would generate $(2997 \text{ or } 2884 \text{ cm}^{-1})/240 \text{ cm}^{-1} \rightarrow 12$ or 13 phonons. It has been observed that the probability of multi-phonon dissipation decreases on the order equivalent to the number of generated phonons.[60]

In an attempt to isolate the monolayer from the Pt(111) surface additional layers of xenon were adsorbed between the methane monolayer and the crystal surface. Xenon was chosen due to its equivalent saturation coverage to methane on Pt and should inhibit the dissipation from methane vibrational excitation into the substrate phonon bath.

4.3.2. Multilayer Desorption

The same experiment described in the previous section was repeated, but with methane coverage increased beyond saturation leading to the formation of a distinct multilayer peak visible in RAIRS spectra which is blue shifted slightly from the monolayer peak at 3014 – 3016 cm^{-1}. Similarly, the on-resonance excitation frequency was blue shifted to maintain irradiation at the peak absorbance frequency. In Figure 4.7 the evolution of RAIRS spectral intensity over intervals of increasing irradiation time is shown both on and off resonance. The rate of methane desorption was measured at four different OPO idler beam power levels (500 mW, 1.0 W, 1.25 W, and 1.5 W) corresponding to four different photon fluxes. All RAIRS spectra depicting methane desorption of the multilayer are shown in Figure 4.7.

The desorption rate of methane was found to be photon flux dependent, where no desorption was detected with only 500 mW irradiation power (on or off resonance Figure 4.7 (a))

and conversely near immediate desorption occurred when the power was increased to 1.5 W (Figure 4.7 (d)). At irradiation powers of 1.00 and 1.25 W a gradual depletion of methane coverage over time allowed for a rate to be determined and compared to off-resonance excitation. In Figure 4.7 (b) and (c) the desorption rate of methane is shown to be higher when photo-excitation frequency is on-resonance with methane vibrational transition frequencies as compared to off-resonance. This suggests the presence of resonant IR photodesorption, however this is complicated by the fact that higher power excitation leads to surface heating which can approach the desorption temperature. Therefore, in order for an effective cross-section to be determined thermal impacts on desorption need to be decoupled for photo-excitation contributions.

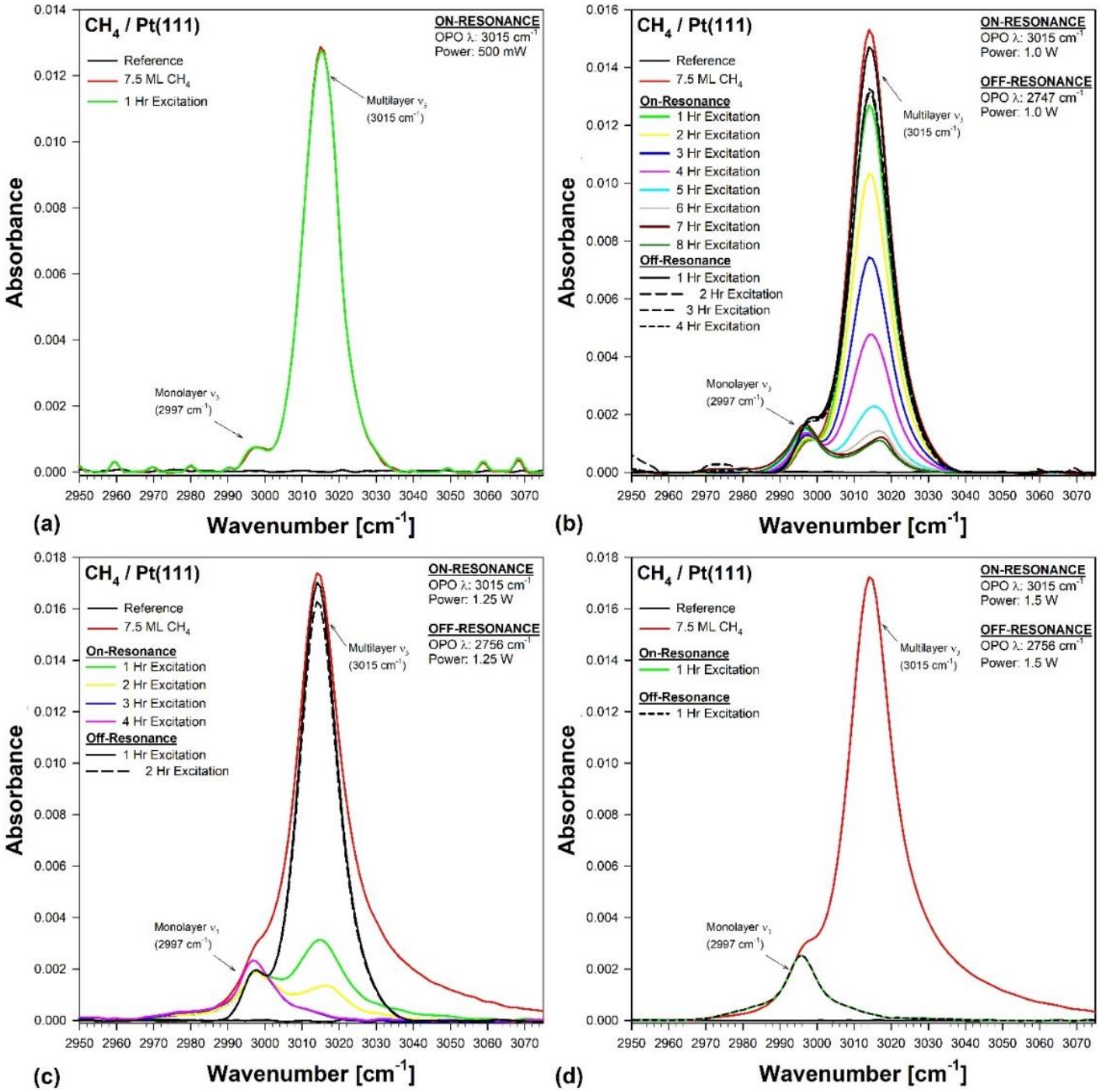

Figure 4.7. RAIRS spectra representative of methane coverage following OPO irradiation both on and off resonance with the ν_3 antisymmetric stretch. Methane desorption was measured at several different irradiation powers **(a)** 500 mW, **(b)** 1.00 W, **(c)** 1.25 W, **(d)** 1.5 W. For all spectra shown the surface was cooled to 40 K.

Again, desorption was attempted to be measured via TOF, however chopping the excitation beam with a 50/50 duty cycle chopper wheel leads to the reduction of the photon flux. Therefore, even at the highest output power of the OPO idler beam, 1.00 W at the surface could not be achieved while chopping the beam. In agreement with the RAIRS spectra, no desorption via TOF was observed below 1.00 W of excitation power.

4.3.3. IR Photodesorption Cross-Sections

Assuming that the on-resonance excitation depletion is the result of resonant IR photodesorption rather than heating effects caused by excitation, a maximum effective photochemical cross-section (σ) can be calculated based on the rate of observed desorption. The desorption can be described as the change in methane coverage as a result of photon absorption by

$$\Delta N = N_0(1 - e^{-\sigma \Im t})$$

Where N is the number of desorbing methane molecules on the surface, $\Im$ is the photon flux and t is time. The coverage as a function of time can then be described as

$$N(t) = N_0 e^{-\sigma \Im \left(t - \frac{\Delta N - N_0}{N_0 \sigma \Im}\right)}.$$

The depletion rate of methane as a function of photon flux for 1.00 and 1.25 W excitation powers is shown in Figure 4.8. It can be easily seen that the desorption rate changes dramatically once coverage drops below three monolayers. To account for this, the calculated depletion rate of methane can be described differently for each region, resulting in

$$N(t) = \begin{cases} \Delta N - N_0(\sigma \Im)t, & 0 \le t < \dfrac{\Delta N - N_0}{N_0 \sigma \Im} \\ N_0 e^{-\sigma \Im \left(t - \frac{\Delta N - N_0}{N_0 \sigma \Im}\right)}, & t \ge \dfrac{\Delta N - N_0}{N_0 \sigma \Im} \end{cases}$$

Where N_0 is the methane coverage which could not be desorbed via photoexcitation.

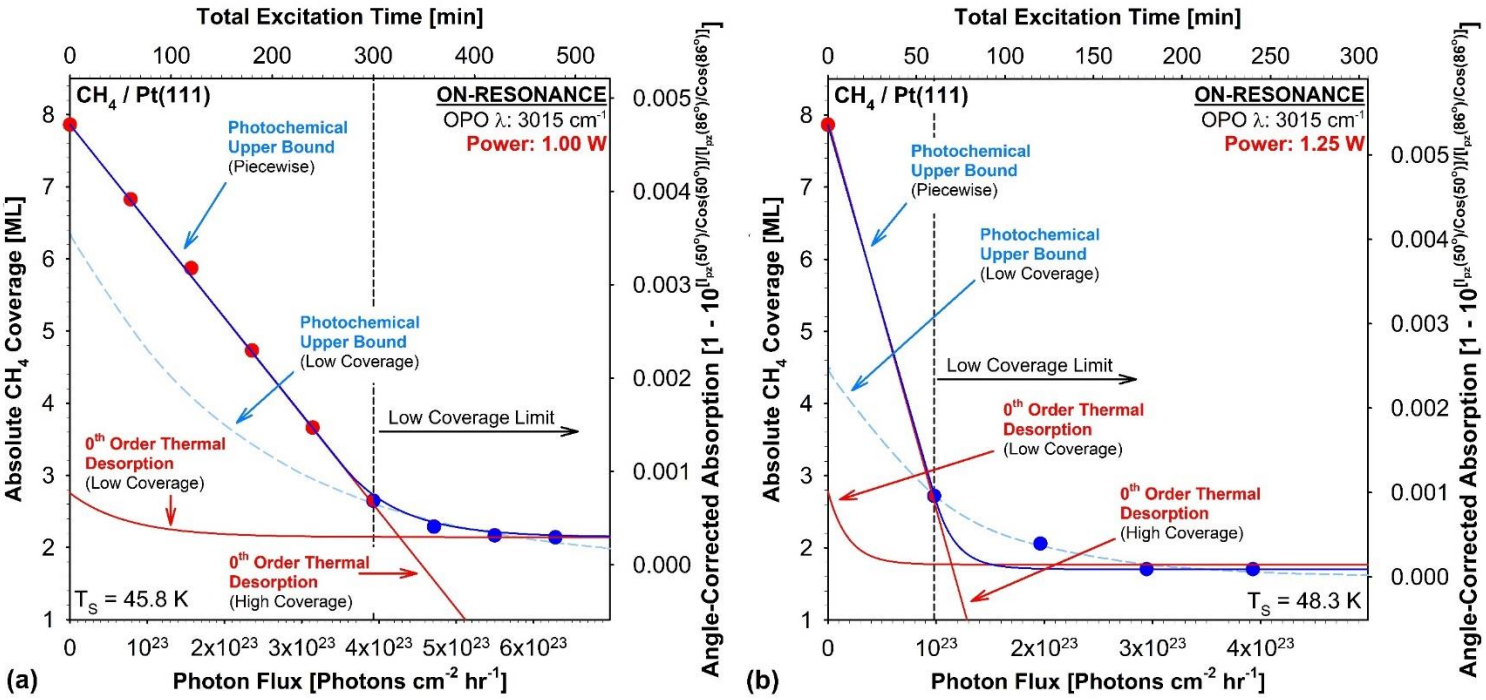

Figure 4.8. Loss of methane coverage as a function of vibrational excitation photon flux in reference to RAIRS spectra shown in **(a)** Figure 4.7 at 1.00 W excitation power and **(b)** Figure 4.7 at 1.25 W excitation power.

The high coverage region was found to fit most closely to 0th order linear decay and the low coverage region (fixed at 2 monolayers) treated as a 1st order exponential decay. By applying a non-linear least-squares fit to the piece-wise function the effective IR photodesorption cross-sections were determined as 1.34x10^{-23} cm^2 for the excitation power of 1.00 W and 6.23x10^{-23} cm^2 at 1.25 W.

IR Photon Flux (photons s^{-1} cm^{-2})	T_S^{Max} (K)	Effective Cross-Section (cm^2)
2.18x10^{19} (1.00 W)	45.8	≤ 1.34x10^{-23}
2.73x10^{19} (1.25 W)	48.3	≤ 5.22x10^{-23}

Table 4.2. Calculated upper-bound effective IR photodesorption cross-sections determined from desorption rates depicted in Figure 4.8.

4.4. Conclusions

Methane desorption efficiency from a Pt(111) single crystal was measured as a result of IR irradiation at frequencies both on and off resonance with methane vibrational stretching modes. When the photon flux was sufficiently high, desorption of methane was found to be more efficient when irradiated on resonance compared to off resonance. As a result of irradiation, particularly at higher photon fluxes, the crystal surface temperature would increase making the effect of photodesorption difficult to separate from thermal contribution. Therefore, from the rate of desorption and the associated photon flux an upper-bound effective IR photodesorption cross-section was able to be determined.

References

(1) Bernath, P. *Spectra of Atoms and Molecules*; Oxford University Press, 2016.

(2) Bordo, V. G.; Rubahn, H. G. *Optics and Spectroscopy at Surfaces and Interfaces*; Blackwell Science Publ, 2005. DOI: 10.1002/9783527618699.

(3) Clarkson, T. W.; Magos, L. The toxicology of mercury and its chemical compounds. *Crit. Rev. Toxicol.* **2006**, *36* (8), 609-662, Review. DOI: 10.1080/10408440600845619 From NLM Medline.

(4) Driscoll, C. T.; Mason, R. P.; Chan, H. M.; Jacob, D. J.; Pirrone, N. Mercury as a Global Pollutant: Sources, Pathways, and Effects. *Environmental Science & Technology* **2013**, *47* (10), 4967-4983, Review. DOI: 10.1021/es305071v From NLM Medline.

(5) Grandjean, P.; Satoh, H.; Murata, K.; Eto, K. Adverse Effects of Methyl-mercury: Environmental Health Research Implications. *Environ. Health Perspect.* **2010**, *118* (8), 1137-1145, Review. DOI: 10.1289/ehp.0901757 From NLM Medline.

(6) Gworek, B.; Dmuchowski, W.; Baczewska, A. H.; Bragoszewska, P.; Bemowska-Kalabun, O.; Wrzosek-Jakubowska, J. Air Contamination by Mercury, Emissions and Transformations-a Review. *Water Air and Soil Pollution* **2017**, *228* (4), 123. DOI: 10.1007/s11270-017-3311-y From NLM PubMed-not-MEDLINE.

(7) Higueras, P.; Oyarzun, R.; Kotnik, J.; Maria Esbri, J.; Martinez-Coronado, A.; Horvat, M.; Angel Lopez-Berdonces, M.; Llanos, W.; Vaselli, O.; Nisi, B.; et al. A compilation of field surveys on gaseous elemental mercury (GEM) from contrasting environmental settings in Europe, South America, South Africa and China: separating fads from facts. *Environmental Geochemistry and Health* **2014**, *36* (4), 713-734. DOI: 10.1007/s10653-013-9591-2 From NLM Medline.

(8) Srivastava, A.; Hodges, J. T. Development of a High-Resolution Laser Absorption Spectroscopy Method with Application to the Determination of Absolute Concentration of Gaseous Elemental Mercury in Air. *Analytical Chemistry* **2018**, *90* (11), 6781-6788, Article. DOI: 10.1021/acs.analchem.8b00757 From NLM Medline.

(9) Slemr, F.; Schuster, G.; Seiler, W. Distribution, Speciation, and Budget of Atmospheric Mercury. *Journal of Atmospheric Chemistry* **1985**, *3* (4), 407-434. DOI: 10.1007/bf00053870.

(10) Method 30A-Determination of Total Vapor Phase Mercury Emissions From Stationary Sources. EPA, Ed.; 2017.

(11) Granite, E. J.; Pennline, H. W. Photochemical removal of mercury from flue gas. *Industrial & Engineering Chemistry Research* **2002**, *41* (22), 5470-5476, Article. DOI: 10.1021/ie020251b.

(12) Pierce, A.; Obrist, D.; Moosmueller, H.; Fain, X.; Moore, C. Cavity ring-down spectroscopy sensor development for high-time-resolution measurements of gaseous elemental mercury in

ambient air. *Atmospheric Measurement Techniques* **2013**, *6* (6), 1477-1489. DOI: 10.5194/amt-6-1477-2013.

(13) Jongma, R. T.; Boogaarts, M. G. H.; Holleman, I.; Meijer, G. Trace Gas-Detection With Cavity Ring Down Spectroscopy. *Review Of Scientific Instruments* **1995**, *66* (4), 2821-2828.

(14) Fain, X.; Moosmueller, H.; Obrist, D. Toward real-time measurement of atmospheric mercury concentrations using cavity ring-down spectroscopy. *Atmos. Chem. Phys.* **2010**, *10* (6), 2879-2892. DOI: 10.5194/acp-10-2879-2010.

(15) Callear, A. B.; Patrick, C. R.; Robb, J. C. The Rection of Excited mercury (Hg63P1) with Oxygen. *Transactions of the Faraday Society* **1959**, *55* (2), 280-287, Article. DOI: 10.1039/tf9595500280.

(16) Marsh, K. M. *Recommended Reference Materials for the Realization of Physicochemico Properties*; Blackwell Scientific Publications, 1987.

(17) Callear, A. B.; Williams, G. J. Cross-sections for deactivation of Hg (63P0). *Transactions of the Faraday Society* **1964**, *60* (0), 2158-2167, 10.1039/TF9646002158. DOI: 10.1039/TF9646002158.

(18) Scheer, M. D.; Fine, J. DEACTIVATION OF HG (63P1) BY CO AND N2. *Journal of Chemical Physics* **1962**, *36* (5), 1264-&, Article. DOI: 10.1063/1.1732725.

(19) Benck, E. C.; Lawler, J. E.; Dakin, J. T. LIFETIMES, BRANCHING RATIOS, AND ABSOLUTE TRANSITION-PROBABILITIES IN HG-I. *Journal of the Optical Society of America B-Optical Physics* **1989**, *6* (1), 11-22, Article. DOI: 10.1364/josab.6.000011.

(20) Pitre, J.; Hammond, K.; Krause, L. 6P-31-6P-30 Excitation Transfer in Mercury, Induced in Collisions with N2 Molecules. *Physical Review A* **1972**, *6* (6), 2101-&, Article. DOI: 10.1103/PhysRevA.6.2101.

(21) *CRC Handbook of Chemistry and Physics*; CRC Press, 2018.

(22) Amadei, A.; Roccatano, D.; Apol, M. E. F.; Berendsen, H. J. C.; Di Nola, A. Prediction of the liquid–vapor equilibrium pressure using the quasi-Gaussian entropy theory. *The Journal of Chemical Physics* **1996**, *105* (16), 7022-7025. DOI: 10.1063/1.472503.

(23) *lmfit/lmfit-py*; Zenodo: 2023. https://doi.org/10.5281/zenodo.8145703 (accessed.

(24) Ben-Lakhdar-Akrout, Z.; Butaux, J.; Lennuier, R. Experimental study of the mercury 4 047 Å line (6 3P 0-7 3S1) absorption profile in the presence of foreign gases. *Journal de Physique* **1975**, *36* (7-8), 625-629. DOI: 10.1051/jphys:01975003607-8062500 Ajp.

(25) Rein, B.; Walther, T. Frequency stabilized diode laser with variable linewidth at a wavelength of 404.7 nm. *Optics Letters* **2017**, *42* (8), 1508-1511. DOI: 10.1364/ol.42.001508 From NLM PubMed-not-MEDLINE.

(26) Barger, R. L.; Hall, J. L. Pressure Shift and Broadening of Methane Line at 3.39 $\ensuremath{\mu}$ Studied by Laser-Saturated Molecular Absorption. *Physical Review Letters* **1969**, *22* (1), 4-8. DOI: 10.1103/PhysRevLett.22.4.

(27) Gordon, I. E.; Rothman, L. S.; Hargreaves, R. J.; Hashemi, R.; Karlovets, E. V.; Skinner, F. M.; Conway, E. K.; Hill, C.; Kochanov, R. V.; Tan, Y.; et al. The HITRAN2020 molecular spectroscopic database. *Journal of Quantitative Spectroscopy and Radiative Transfer* **2022**, *277*, 107949. DOI: https://doi.org/10.1016/j.jqsrt.2021.107949.

(28) Lehmann, K. K. Theoretical detection limit of saturated absorption cavity ring-down spectroscopy (SCAR) and two-photon absorption cavity ring-down spectroscopy. *Appl. Phys. B-Lasers Opt.* **2014**, *116* (1), 147-155. DOI: 10.1007/s00340-013-5663-3.

(29) Lehmann, K. K. Resonance enhanced two-photon cavity ring-down spectroscopy of vibrational overtone bands: A proposal. *J Chem Phys* **2019**, *151* (14), 144201. DOI: 10.1063/1.5122988 From NLM PubMed-not-MEDLINE.

(30) Lehmann, K. K. Optical cavity with intracavity two-photon absorption. *Journal of the Optical Society of America B* **2020**, *37* (10), 3055-3062. DOI: 10.1364/JOSAB.392539.

(31) Demtroder, W. *Laser Spectroscopy: Basic Concepts and Instrumentation*; 2002.

(32) Biraben, F. The first decades of Doppler-free two-photon spectroscopy. *Comptes Rendus Physique* **2019**, *20* (7-8), 671-681. DOI: 10.1016/j.crhy.2019.04.003.

(33) Linstrom, P. *NIST Chemistry WebBook - SRD 69* National Institute of Standards and Technology, 2017. DOI: https://doi.org/10.18434/T4D303.

(34) Zhao, G.; Bailey, D. M.; Fleisher, A. J.; Hodges, J. T.; Lehmann, K. K. Doppler-free two-photon cavity ring-down spectroscopy of a nitrous oxide (N2O) vibrational overtone transition. *Physical Review A* **2020**, *101* (6), 062509. DOI: 10.1103/PhysRevA.101.062509 From NLM PubMed-not-MEDLINE.

(35) Yariv, A. *Quantum Electronics*; 1975.

(36) Aikawa, Y.; Wakelam, V.; Hersant, F.; Garrod, R. T.; Herbst, E. From Prestellar to Protostellar Cores. II. Time Dependence and Deuterium Fractionation. *The Astrophysical Journal* **2012**, *760* (1). DOI: 10.1088/0004-637x/760/1/40.

(37) Garrod, R. T.; Weaver, S. L. W.; Herbst, E. COMPLEX CHEMISTRY IN STAR-FORMING REGIONS: AN EXPANDED GAS-GRAIN WARM-UP CHEMICAL MODEL. *The Astrophysical Journal* **2008**, *682*, 283–302.

(38) Geppert, W. D.; Hamberg, M.; Thomas, R. D.; Osterdahl, F.; Hellberg, F.; Zhaunerchyk, V.; Ehlerding, A.; Millar, T. J.; Roberts, H.; Semaniak, J.; et al. Dissociative recombination of protonated methanol. *Faraday Discuss* **2006**, *133*, 177-190; discussion 191-230, 449-152. DOI: 10.1039/b516010c.

(39) Horn, A.; H., M.; Sekiguchi, O.; Uggerud, E.; Roberts, H.; Herbst, E.; Viggiano, A. A.; Fridgen, T. D. THE GAS-PHASE FORMATION OF METHYL FORMATE IN HOT MOLECULAR CORES. *The Astrophysical Journal* **2004**, *611*, 605–614.

(40) Boogert, A. C. A.; Helmich, F. P.; van Dishoeck, E. F.; Schutte, W. A.; Tielens, A. G. G. M.; Whittet, D. C. B. The gas/solid methane abundance ratio toward deeply embedded protostars. *Astron Astrophys* **1998**, *336*, 352–358.

(41) Vastel, C.; Ceccarelli, C.; Lefloch, B.; Bachiller, R. The Origin of Complex Organic Molecules in Prestellar Cores. *The Astrophysical Journal* **2014**, *795* (1). DOI: 10.1088/2041-8205/795/1/l2.

(42) Wakelam, V.; Smith, I. W. M.; Herbst, E.; Troe, J.; Geppert, W.; Linnartz, H.; Öberg, K.; Roueff, E.; Agúndez, M.; Pernot, P.; et al. Reaction Networks for Interstellar Chemical Modelling: Improvements and Challenges. *Space Science Reviews* **2010**, *156* (1-4), 13-72. DOI: 10.1007/s11214-010-9712-5.

(43) Wright, E. L. The Physics of Interstellar Dust The Physics of Interstellar Dust ,

Endrik Krügel IOP, Philadelphia, 2003. $135.00 (559 pp.). ISBN 0-7503-0861-3. *Physics Today* **2004**, *57* (1), 53-54. DOI: 10.1063/1.1650072.

(44) Ribeiro, F. d. A.; Almeida, G. C.; Wolff, W.; Boechat-Roberty, H. M.; Rocco, M. L. M.; da Silveira, E. F. Low-temperature chemistry induced by cosmic rays: positive and negative ion desorption from nitrile-bearing astrophysical ice analogues. *Monthly Notices of the Royal Astronomical Society* **2020**, *492* (2), 2140-2150. DOI: 10.1093/mnras/stz3562.

(45) Bertin, M.; Fayolle, E. C.; Romanzin, C.; Poderoso, H. A. M.; Michaut, X.; Philippe, L.; Jeseck, P.; Öberg, K. I.; Linnartz, H.; Fillion, J. H. Indirect Ultraviolet Photodesorption from Co:N2binary Ices — an Efficient Grain-Gas Process. *The Astrophysical Journal* **2013**, *779* (2). DOI: 10.1088/0004-637x/779/2/120.

(46) GIBB, E. L.; WHITTET, D. C. B.; SCHUTTE, W. A.; BOOGERT, A. C. A.; CHIAR, J. E.; EHRENFREUND, P.; GERAKINES, P. A.; KEANE, J. V.; TIELENS, A. G. G. M.; VAN DISHOECK, E. F.; et al. AN INVENTORY OF INTERSTELLAR ICES TOWARD THE EMBEDDED PROTOSTAR W33A. *The Astrophysical Journal* **2000**, *536*, 347È356.

(47) Chen, Y. J.; Dartois, E.; Muñoz Caro, G. M.; Cruz-Díaz, G. A.; Carrascosa, H. Photon-induced desorption of larger species in UV-irradiated methane ice. *Monthly Notices of the Royal Astronomical Society* **2020**, *493* (1), 821-829. DOI: 10.1093/mnras/staa334.

(48) Chuang, T. J.; Hussla, I. Time-Resolved Mass-Spectrometric Study on Infrared Laser Photodesorption of Ammonia from Cu(100). *Physical Review Letters* **1984**, *52* (23), 2045-2048. DOI: 10.1103/PhysRevLett.52.2045.

(49) Hassel, M.; Svensson, K.; Persson, M.; Anderson, S. Direct Infrared Photodesorption of Physisorbed H2. *Physical Review Letters* **1998**, *80*.

(50) Heidberg, J.; Stein, H.; Riehl, E. Resonance, Rate, and Quantum Yield of Infrared-Laser-Induced Desorption by Multiquantum Vibrational Excitation of the Adsorbate CH3F on NaCl. *Physical Review Letters* **1982**, *49* (9), 666-669. DOI: 10.1103/PhysRevLett.49.666.

(51) Hussla, I.; Chuang, T. J. Infrared-Laser Spectroscopy of Ammonia-Copper Adsorbates by Infrared-Laser-Induced Photodesorption under Ultrahigh Vacuum. *J. Opt. Soc. Am. B* **1984**, *1*.

(52) Anderson, A.; Savoie, R. Raman Spectra of Crystalline CH4 and CD4. *Journal of Chemical Physics* **1965**, *43*, 3468–3473 DOI: 10.1063/1.1696502.

(53) Emtiaz, S. M.; Toriello, F.; He, J.; Vidali, G. Infrared Spectroscopic Study of Methane Ice, Pure and in Mixtures with Polar (H2O) and Nonpolar (N2) Molecules. *J Phys Chem A* **2022**, *126* (12), 1973-1979. DOI: 10.1021/acs.jpca.2c00287.

(54) Herzberg, G. *MOLECULAR SPECTRA and MOLECULAR STRUCTURE II. INFRARED AND RAMAN SPECTRA OF POLYATOMIC MOLECULES*; D. Van Nostrand Company, Inc., 1945.

(55) Yoshinobu, J.; Ogasawara, H.; Kawai, M. Symmetry Controlled Surface Photochemistry of Methane on Pt(111). *Physical Review Letters* **1995**, *75*.

(56) Chuang, T. J. LASER-INDUCED GAS-SURFACE INTERACTIONS. *Surface Science Reports* **1983**, *3*.

(57) Gortel, Z. W.; Kreuzer, H. J.; Piercy, P.; Teshima, R. Theory of photodesorption of molecules by resonant laser-molecular vibrational coupling. *Physical Review B* **1983**, *27* (8), 5066-5083. DOI: 10.1103/PhysRevB.27.5066.

(58) Gortel, Z. W.; Kreuzer, H. J.; Piercy, P.; Teshima, R. Resonant heating in photodesorption via laser-adsorbate coupling. *Physical Review B* **1983**, *28* (4), 2119-2124. DOI: 10.1103/PhysRevB.28.2119.

(59) Chuang, T. J.; Seki, H.; Hussla, I. INFRARED PHOTODESORPTION: VIBRATIONAL EXCITATION AND ENERGY TRANSFER PROCESSES ON SURFACES. *Surface Science* **1985**, *158*.

(60) Zhdanov, V. P.; Zamaraev, K. I. Vibrational Relaxation of Adsorbed Molecules. Mechansims and Manifestations in Chemical Reactions on Solid Surfaces. *Catal. Rev.-Sci. Eng.* **1982**, *24*.